ISSN: 2156-8359 Volume 17, Number 1, January 2026

Scientific Research Publishing

International Journal of Geosciences

ISSN: 2156-8359
9 772156 835003 01

https://www.scirp.org/journal/ijg

Journal Editorial Board

ISSN: 2156-8359 (Print) ISSN: 2156-8367 (Online)

https://www.scirp.org/journal/ijg

Scientific Research Publishing

International Journal of Geosciences, 2026, 17(1), 1-87
https://www.scirp.org/journal/ijg
ISSN Online: 2156-8367
ISSN Print: 2156-8359

Table of Contents

Volume 17 Number 1 January 2026

International Journal of Geosciences (IJG)
Journal Information

SUBSCRIPTIONS

The *International Journal of Geosciences* (Online at Scientific Research Publishing, https://www.scirp.org/) is published monthly by Scientific Research Publishing, Inc., USA.

Subscription rates:
Print: $79 per copy.
To subscribe, please contact Journals Subscriptions Department, E-mail: sub@scirp.org

SERVICES

Advertisements
Advertisement Sales Department, E-mail: service@scirp.org

Reprints (minimum quantity 100 copies)
Reprints Co-ordinator, Scientific Research Publishing, Inc., USA.
E-mail: sub@scirp.org

COPYRIGHT

PRODUCTION INFORMATION

For manuscripts that have been accepted for publication, please contact:
E-mail: ijg@scirp.org

International Journal of Geosciences, 2026, 17(1), 1-13
https://www.scirp.org/journal/ijg
ISSN Online: 2156-8367
ISSN Print: 2156-8359

Subsidence and Thermal History Effect on Source Rock Maturity of Semliki Basin, Albertine Graben, Uganda

Vivianne Maria Naiga[1], Ehinola Olugbenga[2], Simon Echegu[3,4]

[1]Department of Geology, Pan African University Life and Earth Science Institute (Including Health and Agriculture), University of Ibadan, Ibadan City, Oyo State, Nigeria
[2]Department of Geology, University of Ibadan, Ibadan City, Oyo State, Nigeria
[3]Department of Geology and Petroleum Studies, Makerere University, Kampala, Uganda
[4]Department of Energy, Minerals & Petroleum Studies, Mbarara University of Science and Technology, Mbarara, Uganda
Email: ngviviennemarie@gmail.com, ehinola01@yahoo.com, sechegu@must.ac.ug

How to cite this paper: Naiga, V.M., Olugbenga, E. and Echegu, S. (2026) Subsidence and Thermal History Effect on Source Rock Maturity of Semliki Basin, Albertine Graben, Uganda. *International Journal of Geosciences*, **17**, 1-13.
https://doi.org/10.4236/ijg.2026.171001

Received: July 1, 2024
Accepted: January 11, 2026
Published: January 14, 2026

Abstract

The research study focused on the analysis of subsidence and thermal history effects on source rock maturity in the Semliki Basin. The study utilised the back stripping approach and was accomplished using PetroMod Software. The research utilized previous data sets obtained from geochemical reports and final well data reports to generate a basin model of eight (08) Sedimentary Formations ranging in age from Lower Miocene to Pleistocene sediments *i.e.*, Surface, Nyabusozi-Nyakabingo, Nyaburogo, Oluka, Kakara, Kasande, Kisegi and Basement formations. The general trend of subsidence observed is a rapid deepening (13.0 to 11.5 Ma and 3.5 to 2.0 Ma) during the main and later rift phases respectively, followed by an exponential decline in the rate of tectonic subsidence. The maximum heat flow (77.59 mWm^{-2}) at 3.5 Ma corresponds to the Late Pliocene to Pleistocene thus deep burial conditions and represents maximum paleo-temperatures. The medium/dark shales of the Kasande-Kakara formations (2070 - 2100 m and 2480 - 2488 m) are the most prospective source rocks and comprise organic matter (TOC c.2.0%) and an oil-prone Type I/II source rock quality. The source rock maturity plots indicate that the source rock entered the early oil zone at 2.0 Ma whereby the top of the oil generation window is observed with Ro 0.5%, corresponding to the Kasande-Kakara formations at a depth of 2400 - 2500 m. This corresponds to the second subsidence event; however, there was no commencement of oil generation. Though limited by the scope of the data set, this study allowed for a quantification of tectonic subsidence and thermal maturity effects on the identified source rock horizons of the Semliki Basin sediments.

Keywords

Heat Flow, Backstripping, Subsidence, Basin Model, Vitrinite Reflectance, Source Rock Maturity, Albertine Graben

1. Introduction

Subsidence in sedimentary basins results from various processes, such as stretching and extension of the continental crust, loading from accumulated sediments and volcanic deposits, thickening of the mantle lithosphere during cooling, tectonic loading, metamorphism, or phase changes that increase crustal density, etc., that allow accommodation-infilling sediments to be spatially distributed. It is possible to reconstruct different subsidence curves from different positions in the same sedimentary basin because geodynamic evolution can differ from place to place and the existence of syn-depositional faults [1].

Dispersed organic matter in sedimentary basins undergoes significant and irreversible reactions as temperatures increase [2] [3]. Consequently, it is suitable for petrological and geochemical investigations to examine characteristics indicative of the maximum temperatures attained during burial.

The analysis of thermal maturity involves an evaluation of parameters, including the reflectance of dispersed organic matter, such as vitrinite reflectance or solid bitumen particles [4].

Therefore, using subsidence observations as a basis for interpretation, an examination of the thermal maturity of identified source rock horizons can be made.

2. Geological Setting and Stratigraphy

The research study area, Semliki Basin, is located between Lake Albert and the northern tip of the Rwenzori Mountains. It is made up of the Semliki Flats and the Toro Plain, which are located southwest of Lake Albert and is situated within the Western Branch of the East African Rift System, specifically in the Albertine Graben, which stretches along the border between Uganda and the Democratic Republic of Congo.

The rift basins that make up the Western Rift of the East African Rift System (EARS) are characterized by an asymmetrical and half-graben geometry and are bounded by major normal faults and faulted flexure on either side [5]. During the Late Miocene to Pliocene, intense rifting resulted in significant vertical movements and the Semliki Basin developed as an asymmetric half-graben. Specifically, the Rwenzori uplift, accompanied by faulting along the basin margins, created accommodation space for sediment to accumulate.

Thick lacustrine, fluvial and alluvial sediments filled in the asymmetric basins along the strike of the rift system of more than 5 km [6]. Source rocks developed mainly during the synrift in deeper portions while reservoirs developed mainly in shallow lacustrine and flexural areas.

The Semliki Basin (**Figure 1**), is particularly important as a study area to provide insights into the dynamics of subsidence, thermal history, and sedimentation in a rift basin setting. The subsidence and thermal history of a basin are crucial for understanding the basin's evolution, sedimentation patterns and potential for hydrocarbon generation. Understanding subsidence history can improve comprehension of the tectonic forces shaping the basin, the rate of sediment deposition and the burial history of organic matter, whereas thermal history enables assessment of the maturation of source rocks and understanding hydrocarbon generation and migration processes. In the case of the Semliki Basin, these two factors are especially significant given the basin's tectonic setting and potential for hydrocarbon accumulations.

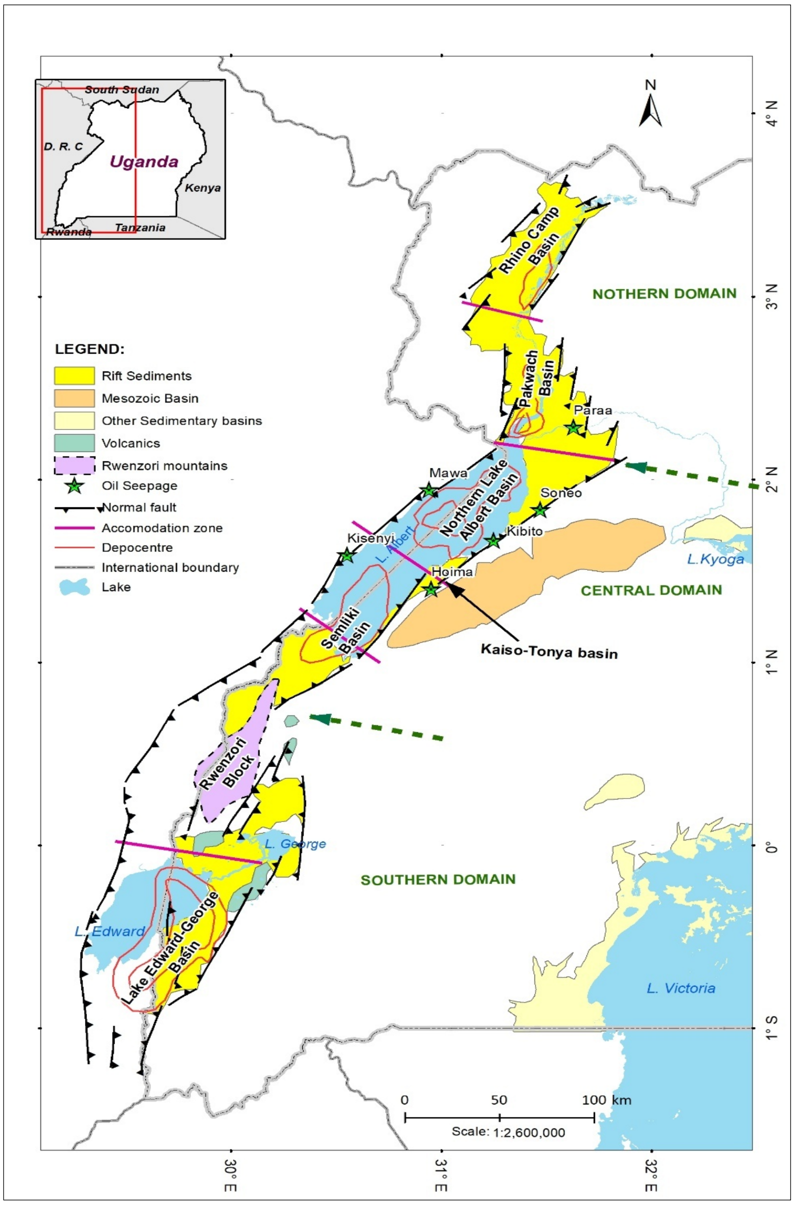

Figure 1. Sedimentary basins and structural setup of the of the Albertine Graben [9].

Previous studies have shown that the Kasande Formation, which is located within the Semliki Basin, has source rock characteristics that indicate potential for significant hydrocarbon generation [7]. The deposition of the Kasande Formation was suggested to be either early to mid-Miocene or early Pliocene whereas the Kakara Formation was of early to mid-Miocene and late Pliocene as determined from palynomorph assemblages in the Turaco wells [8].

By applying backstripping techniques, this research aimed to determine the potential for hydrocarbon generation of the Semliki Basin by considering the historical changes in basin depth, sedimentation rates and temperature evolution.

The first deep wells (Turaco 1, 2, and 3) drilled by Heritage in the Semliki Basin from 2002 to 2004 (in Western Uganda) provided favourable results about the discovery of hydrocarbons. However, this positive development yielded mixed outcomes since the natural gas tested in the Turaco-3 Well was heavily contaminated with Carbon dioxide (CO_2).

From the well sections, the Kasande Formation is characterized by grey, brown-grey, dark grey to reddish brown claystones and mudstones whereas the Kakara Formation overlies the Kasande Formation with a coarsening and shallowing upwards sequence of a sandy base, lacustrine shales and then topped by interbedded sands and shales. In the Turaco-3 well, the Kasande and Kakara Formations were also found to have 115 m and 542 m average thicknesses respectively (Turaco 1, 2 and 3 Final well reports).

3. Methods

3.1. Data Collection and Input Preparation

During the first stage of modelling, at the input stage, the main data sets used comprise geological, geochemical and geophysical information about the formation layers in the Semliki basin.

The stratigraphic well tops were defined based on the recorded depths at which they were encountered in the Turaco wells during drilling and then used as input for the simulation. The model includes 08 layers ranging in age from Lower Miocene to Pleistocene sediments *i.e.*, Basement, Kisegi, Kasande, Kakara, Oluka, Nyaburogo, Nyabusozi-Nyakabingo and Surface. Thicknesses were modified after [10] and [11].

Different lithologies were assigned to the layers based on the work of [8]. The Kisegi Formation was considered as sandstone, the Kasande Formation as a clay rich siliclastic mudstone and then the Kakara, Oluka and Nyaburogo Formations were considered as majorly sandstones interbedded with claystones. The absolute ages and the PSE assignment for the different well tops are from [12] and [8] respectively. The average TOC content for the shales within the Kasande and Nyaburogo formations was assigned based on the source rock geochemistry by [13].

3.2. Decompaction and Porosity Modelling

The backstripping technique involves three main stages, including decompacting sediments, removing sediment loads (isostatic adjustment), and calculating tectonic subsidence.

Using Athy's Law [14], the porosity (ϕ) reduction with depth due to compaction was modelled as shown in equation 3.1:

$$\phi(z) = \phi_{\circ} e^{(-cz)} \tag{3.1}$$

where, ϕ is the porosity of the rock at depth z (in Km), $\phi_{\circ}$ is the surface porosity (shale: ~ 0.5, sandstone: ~0.4) and c is the rock specific compaction coefficient (shale: ~0.5 km^{-1}, sandstone: ~0.3 km^{-1}).

Decompaction was then performed for each layer to restore its original thickness and correct for sediment loading.

3.3. Tectonic Subsidence Calculation

The tectonic subsidence (S_t) was calculated by removing sediment and water loads and correcting for compaction and eustasy using the equation 3.2, derived from [15]:

$$S_t = T_s .(1 - (\rho_s - \rho\omega)/(\rho_m - \rho\omega)) \tag{3.2}$$

where, ρ_m is the mantle density (~3.3 g/cm^3), ρ_s is the sediment density (~2.2-2.5 g/cm^3) and $\rho\omega$ is the water density (~1.0 g/cm^3) and T_s is the sediment thickness corrected for compaction.

3.4. Thermal History and Maturity Modelling

Thermal evolution was modelled by solving the heat conduction equation over geologic time, expressed as equation 3.3:

$$\delta T/\delta t = \kappa \delta^2 T/\delta z^2 \tag{3.3}$$

where, T is temperature, t is time, z is depth and κ is the thermal diffusivity ($\kappa = k/(\rho c_p)$), as derived from [16].

Boundary conditions were defined by surface temperature and basal heat flow and assigned per lithology. In the Semliki Basin, paleo water depth reconstructions are closely tied to the basin's depositional history, which was influenced by alternating fluvial, deltaic, and lacustrine environments. Active tectonics in the Semliki area could steepen gradients and deepen lakes rapidly, therefore, based on the methodology outlined by [17] and facies analysis, the lacustrine deposition setting characterized by laminated clays, massive silts and diatomaceous muds was assigned depths of eighty to one hundred fifty meters, ten to fifty meters for the deltaic and zero to five meters for the fluvial environments. According to [18], these estimates align with other analogous modern and ancient rift lake (e.g., Lake Tanganyika, Lake Malawi). For the basin model, the syn-rift phase (Miocene) was assigned paleo-heat flow values of above 70 mW/m^2, consistent with active rifting [19], followed by a decaying trend in the later-rift phase, transitioning through 70 - 80 mW/m^2 in the early later-rift (Pliocene) to 54 - 66 mW/m^2 at present, accounting for local variations due to faulting.

Maturity of the source rocks is a key factor in determining the source rock potential for hydrocarbon generation. Organic matter maturation was then modelled using the Easy% Ro kinetic model expressed as equation 3.4, derived from [20]:

$$\%\mathrm{Ro} = f\left(\int e^{((-E)/(RT(t))\,dt)}\right) \quad (3.4)$$

where E is the activation energy, R is the universal gas constant, and T(t) is the burial temperature over time.

Using [21] approach, the SWIT through time was calculated to obtain a relationship between geologic age and mean surface paleo-temperature based on plate tectonic reconstructions to present-day latitudes. Using Petro Mod software, the tool extracted the standard temperatures based on the present-day geographic location (Northern Hemisphere, North Africa) and latitude (1˚) of the Semliki basin as shown in **Figure 2**.

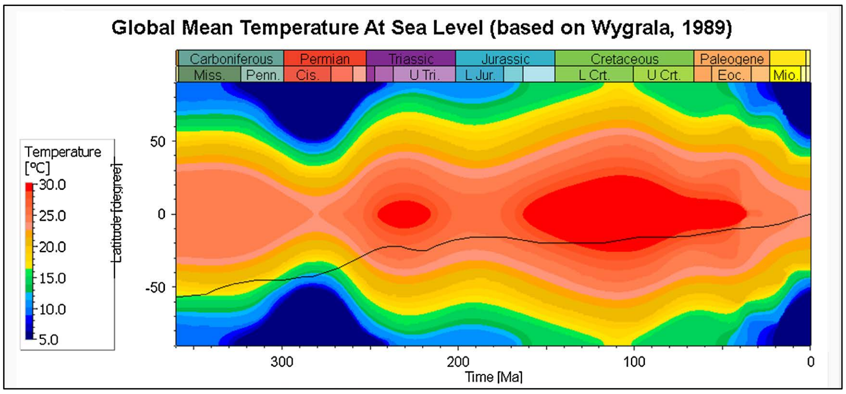

Figure 2. Variation in sediment-water interface temperature (SWIT) in the Semliki basin over time, illustrating the relationship between geologic age and mean surface paleo-temperature.

3.5. Calibration and Sensitivity Analysis

The model outputs were then calibrated using measured Vitrinite Reflectance (%Ro) and Bottom Hole Temperature (BHT).

The outputs from the simulation include temperature vs. depth curves and maturity vs. depth curves. These results were then used to assess source rock potential for hydrocarbon generation. Sensitivity tests involved varying key parameters such as heat flow to evaluate the model's consistency.

Therefore, using the subsidence observations as a basis for interpretation, an examination of the thermal maturity of identified source rock horizons was made.

4. Results and Discussion

4.1. Subsidence Analysis

During the main-rift phase of basin development (17 - 2.7 Ma), the general trend in subsidence is a moderate increase. As shown in **Figure 3**, two significant subsidence events are observed during the Miocene (13.0 - 11.5 Ma) and at the end of Pliocene and the onset of Pleistocene (3.5 - 2.0 Ma). The later-rift phase, at 2.7

Ma, marks the onset of thermal relaxation of the lithosphere basin development.

The main rifting phase characterised by rapid subsidence rates helped create deep, anoxic lacustrine conditions which are ideal for formation of organic rich source rocks. The later-rift thermal subsidence phase is characterized by slower subsidence rates that helped maintain the earlier anoxic conditions and prevented organic matter degradation. Elevated geothermal gradients during rifting also contributed to accelerate organic matter maturation.

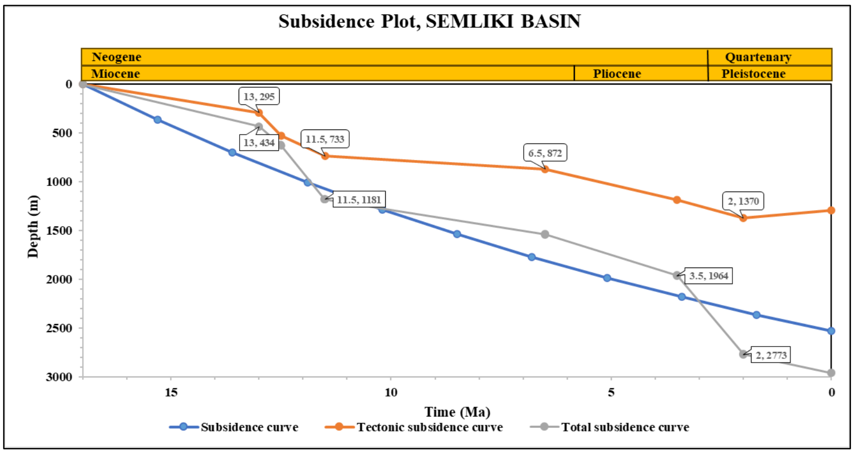

Figure 3. Tectonic and Total Subsidence plot for Semliki Basin. The subsidence histories indicate two rapid deepening events that occurred during the Miocene and End of Pliocene.

4.2. Paleo Water Depth, SWIT and Basal Heat Flow Interpretation

During deposition, the Sediment Water Interface Temperature (SWIT) was influenced by the palaeolatitude and water depth. Increased water depth with lower temperatures indicated sedimentation of the Kasande formations. Simulations with the heat flow curve illustrated the thermal history of the sediments as an overlay.

The heat flow curve (**Figure 4**) shows heat flow variations in the Semliki Basin with time. The heat flow gradually increased over time and reaching a maximum heat flow (77.59 mWm^{-2}) at 3.5 Ma (Pliocene). The heat flow trend during earlier periods was low but steadily increased, reaching a maximum peak before slowly decreasing. This, in turn, significantly affected source rock maturation within the basin, *i.e.* effects arising from the occurrence of sustained later-rift thermal influence from residual heat, hydrothermal fluids, deep-seated faults, etc.

According to [22], typically, the oil window falls within the vitrinite reflectance (VR) range of 0.6% - 1.4%, with the former as the top of the oil window and the latter as the bottom of the oil window (deadline). At 2400 - 2550 m, the top of the oil generation window is observed with Ro 0.6%, corresponding to the Kasande-Kakara formations (**Figure 5**). The maturity gradients closer to surface, for example, at 700 m with values of less than Ro 0.4%, show that the well section has not undergone net uplift and erosion, and is presently at maximum burial and maturity.

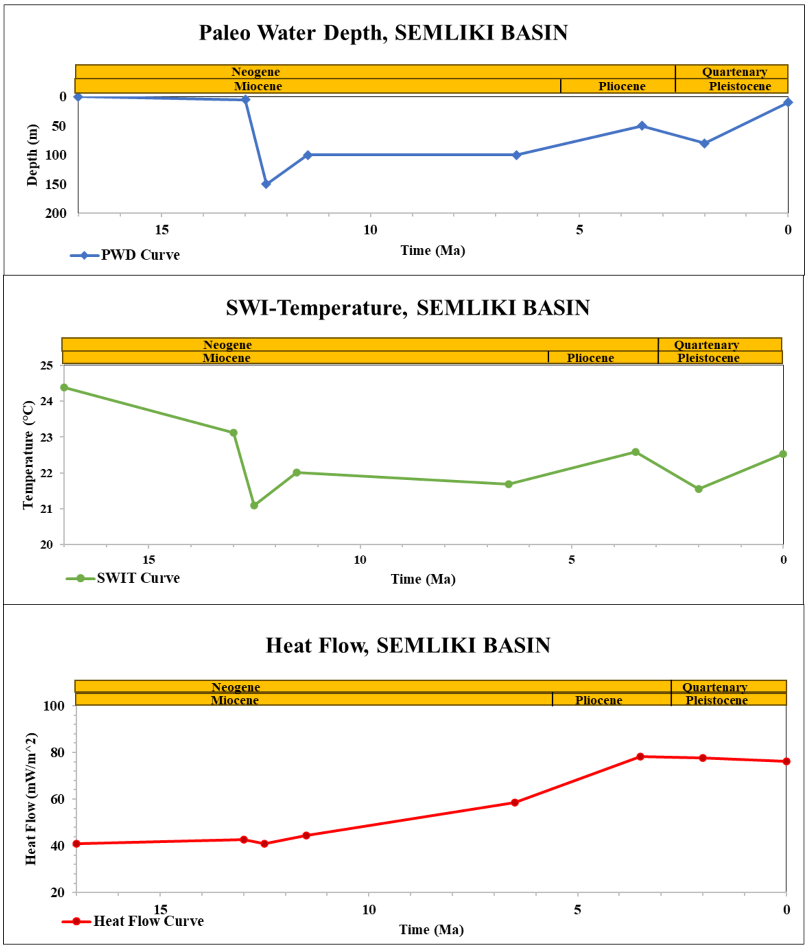

Figure 4. Plot showing curves generated for Paleo Water Depth (PWD), Sediment Water Interface Temperature (SWIT) and Heat Flow (HF) over time.

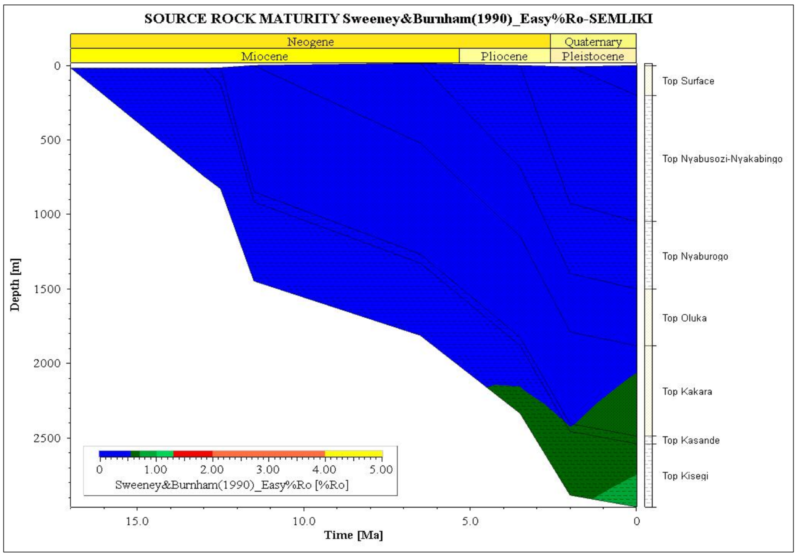

Figure 5. Source rock maturity curves through Turaco-1 Well in Semliki Basin. Plot indicates that the Kasande Formation, the presumed source rock is currently at the early oil window at ~2 Ma and at depth of 2400 m.

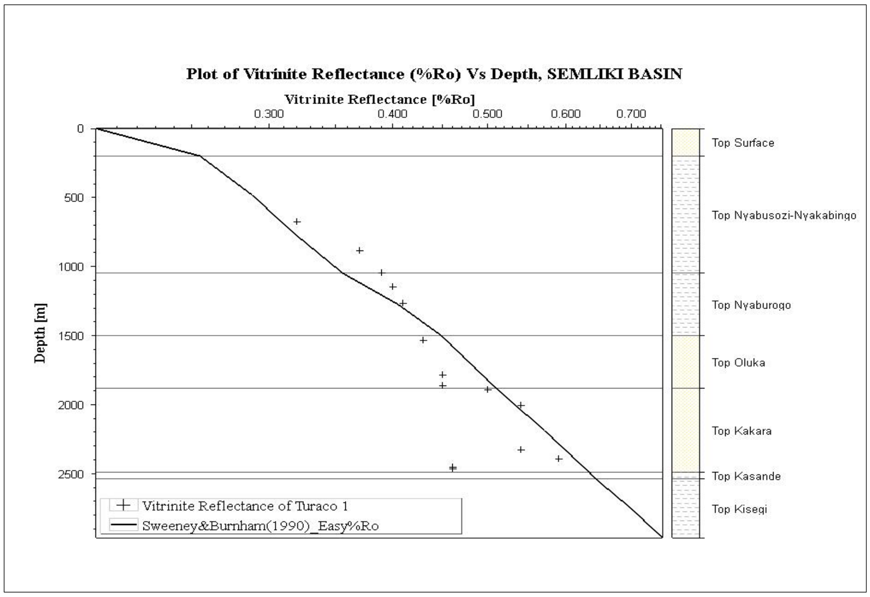

Figure 6. Calibrated Vitrinite Reflectance (%Ro) for Turaco-1 Well; fit of measured VR values (black crosses) with the calculated VR values (solid black line).

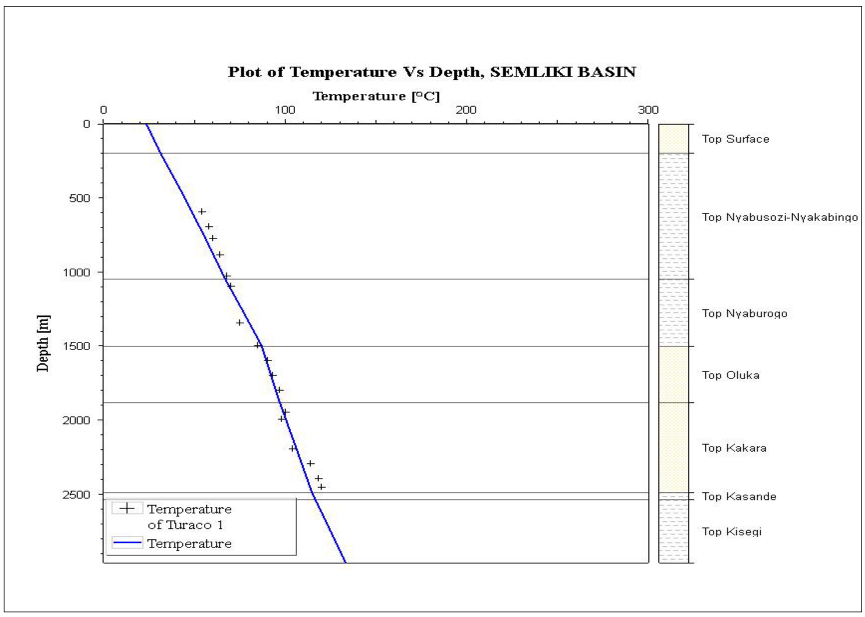

Figure 7. Calibrated Temperature (°C) for Turaco-1 Well; fit of measured temperature values (black crosses) with the calculated temperature values (blue line).

A vitrinite reflectance (VR) profile provides an indication of the level of thermal maturity of the source rocks. The majority of the source rock data from the Turaco-1 Well section was found to be thermally immature with respect to petroleum generation. VR and temperature data were plotted with depth, as shown in **Figure 6** and **Figure 7**. The two plots illustrate the effect of the heat flow which responsible for the thermal maturity of the source rock, *i.e.*, the increase in % Ro with depth suggests that the deeper formations, such as the Kisegi Formation underwent sufficient high temperature conditions which are favourable for generation of hydrocarbons. Unfortunately, however, the Kisegi Formation is not a source rock but a known reservoir rock in the Semliki basin.

4.3. Transformation Ratio (TR)

The transformation ratio is a critical parameter that quantifies the fraction of kerogen in a source rock that has been converted to hydrocarbons. However, as observed from the TR plot (**Figure 8**), no oil has been generated in the basin, despite having source rocks with good oil generation potential. This is consistent with the temperature curve model (**Figure 9**) that shows Kasande Formation, a presumed source rock in the Semliki basin having just reached temperatures around 100 - 120.

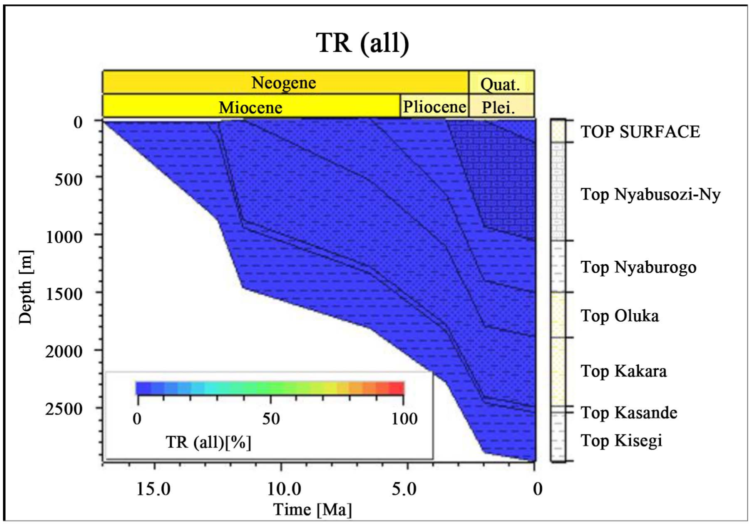

Figure 8. Transformation ratio, TR plots through Turaco-1 Well in the Semliki Basin. The plot illustrates no organic matter transformation, suggesting immaturity with respect to petroleum generation.

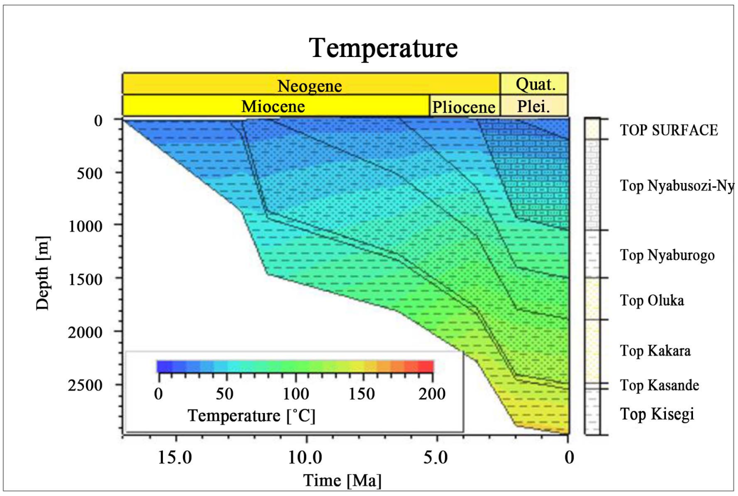

Figure 9. Thermal history model curves of Semliki Basin, Turaco-1 Well. Kasande, the presumed source rock is currently at temperatures between 100˚C to 120˚C.

5. Summary, Conclusion, and Recommendations

5.1. Summary

The general trend of subsidence observed is a rapid deepening during the rift stage, followed by an exponential decline in the rate of tectonic subsidence. In addition to the elevated geothermal gradients characteristic of extensional tectonic settings, the source rock maturity was influenced by progressive subsidence during the rift stage, which enabled the accumulation of thick organic-rich sedimentary sequences and allowed for prolonged deep burial conditions. Following the main rifting phase, thermal subsidence continued to contribute to burial as additional sediments were deposited. The maximum heat flow (77.59 mWm^{-2}) obtained at 3.50 Ma corresponds to the Late Pliocene to Pleistocene and represents times of deepest burial and maximum temperatures.

From the 1-D basin modelling results, the Kasande-Kakara Formations indicate good source rock potential, *i.e.*, they are thermally mature but are still in the early development stages and have not spent the necessary duration in the oil window required to favour oil generation. The source rock maturity plots indicate that the Kasande Formation at depths of 2400 - 2550 m reached the early oil window around 2 Ma, which corresponds to the second subsidence event.

5.2. Conclusions

The findings from the thermal modelling through the Turaco-1 Well suggest that while the Semliki Basin possesses good potential source rocks, the source rocks are immature or only marginally mature at the vicinity of the Turaco-1 Well. Therefore, any hydrocarbons must have been generated in the deeper basin, west of the Turaco-1 Well where increased burial depth may have led to earlier or more sustained maturation. Structural highs and fault closures in these deeper areas may serve as potential traps.

From a regional perspective, the Semliki Basin's geological characteristics and structural setting show strong analogies with other productive basins of the East African Rift System in Uganda where the current Kingfisher and Tilenga oilfields are located. Its continued burial, lack of significant uplift, and relatively recent tectonic inactivity imply that the petroleum system may still be evolving.

5.3. Recommendations

Turaco-1 and Turaco-2 wells were drilled in the same location; therefore, this limited the lateral range of the data. More data sets, especially well data, and geochemical analyses, are required to obtain a comprehensive analysis of the source rock geochemistry of the Semliki Basin.

Further geophysical surveys, including deep seismic imaging, would be essential to map these depocenters accurately. Additionally, forward modelling of burial history, incorporating sedimentation rates, paleo geothermal gradients, and erosion estimates, could refine predictions of maturity levels across the basin. This would help de-risk plays and guide future exploratory drilling.

The impact of internal heat generation in sedimentary rocks should be considered for upcoming models. This is because the Vitrinite Reflectance Vs. Depth Trend is moved to lower VR values when the internal heat production is disregarded [23].

Conflicts of Interest

The authors declare no conflicts of interest regarding the publication of this paper.

References

[1] Ingersoll, C. and Azor, A. (2011) Tectonics of Sedimentary Basins. Blackwell Publishing Ltd., 3-43.

[2] Bostick, N.H. and Foster, J.N. (1975) Comparison of Vitrinite Reflectance in Coal Seams and in Kerogen of Sandstones, Shales, and Limestones in the Same Part of a Sedimentary Section. Centre National de la Recharche Scientifique, 13-25.

[3] Scheidt, G. and Littke, R. (1989) Comparative Organic Petrology of Interlayered Sandstones, Siltstones, Mudstones and Coals in the Upper Carboniferous Ruhr Basin, Northwest Germany, and Their Thermal History and Methane Generation. *Geologische Rundschau*, **78**, 375-390. https://doi.org/10.1007/bf01988371

[4] Littke, R., Urai, J.L., Uffmann, A.K. and Risvanis, F. (2012) Reflectance of Dispersed Vitrinite in Palaeozoic Rocks with and without Cleavage: Implications for Burial and Thermal History Modeling in the Devonian of Rursee Area, Northern Rhenish Massif, Germany. *International Journal of Coal Geology*, **89**, 41-50. https://doi.org/10.1016/j.coal.2011.07.006

[5] Daly, M.C., Chorowicz, J. and Fairhead, J.D. (1989) Rift Basin Evolution in Africa: The Influence of Reactivated Steep Basement Shear Zones. *Geological Society, London, Special Publications*, **44**, 309-334. https://doi.org/10.1144/gsl.sp.1989.044.01.17

[6] Abeinomugisha, D. and Kasande, R. (2013) Tectonic Control on Hydrocarbon Accumulation in the Intracontinental Albertine Graben of the East African Rift System. In: Gao, D.L., Ed., *Tectonics and Sedimentation*, American Association of Petroleum Geologists, 209-228. https://doi.org/10.1306/13351554m1003539

[7] Mutebi, S., Sen, S., Sserubiri, T., Rudra, A., Ganguli, S.S. and Radwan, A.E. (2021) Geological Characterization of the Miocene-Pliocene Succession in the Semliki Basin, Uganda: Implications for Hydrocarbon Exploration and Drilling in the East African Rift System. *Natural Resources Research*, **30**, 4329-4354. https://doi.org/10.1007/s11053-021-09951-0

[8] Lukaye, J., Worsley, D., Kiconco, L., Nabbanja, P., Abeinomugisha, D., Amusugut, C., *et al.* (2016) Developing a Coherent Stratigraphic Scheme of the Albertine Graben-East, Africa. *Journal of Earth Science and Engineering*, **6**, 264-294. https://doi.org/10.17265/2159-581x/2016.05.004

[9] Lukaye, J. and Okello, M. (2015) Geochemical Characterization and Correlation of Crude Oils and Potential Source Rocks from the Semliki, Southern Lake Albert and Kaisotonya Basins in the Albertine Graben, Uganda. *International Conference and Exhibition*, Melbourne, 13-16 September 2015, 557. https://doi.org/10.1190/ice2015-2210807

[10] H. O. a. G. Limited (2003) Turaco-1 Final Well Report (Geological Section). Report of Heritage Oil & Gas Limited (HOGL).

[11] H. O. a. G. Limited (2004) Turaco-2 Final Well Report (Geological Section). Report

of Heritage Oil & Gas Limited (HOGL).

[12] Lukaye, J.M. (2009) Biostratigraphy and Palynofacies of Four Exploration Wells from the Albertine Graben, Uganda. AAPG, Article No. 50169.

[13] Kaye, M.N. (2004) Source Rock Geochemistry Report Turaco-1 Well, Uganda. Aberdeen. Ocean Grove Geoscience Limited.

[14] Athy, L.F. (1930) Density, Porosity, and Compaction of Sedimentary Rocks. *AAPG Bulletin*, **14**, 1-24. https://doi.org/10.1306/3d93289e-16b1-11d7-8645000102c1865d

[15] Steckler, M.S. and Watts, A.B. (1978) Subsidence of the Atlantic-Type Continental Margin off New York. *Earth and Planetary Science Letters*, **41**, 1-13. https://doi.org/10.1016/0012-821x(78)90036-5

[16] Fowler, C.M.R. (2004) The Solid Earth: An Introduction to Global Geophysics. 2nd Edition, Cambridge University Press. https://doi.org/10.1017/cbo9780511819643

[17] Immenhauser, A. (2009) Estimating Palaeo-Water Depth from the Physical Rock Record. *Earth-Science Reviews*, **96**, 107-139. https://doi.org/10.1016/j.earscirev.2009.06.003

[18] Scholz, C.A. (1995) Deltas of the Lake Malawi Rift, East Africa: Seismic Expression and Exploration Implications. *AAPG Bulletin*, **79**, 1679-1697. https://doi.org/10.1306/7834de54-1721-11d7-8645000102c1865d

[19] Allen, P.A. and Allen, J.R. (2005) Basin Analysis, Principles and Applications. Blackwell Publishing.

[20] Sweeney, J.J. and Burnham, A.K. (1990) Evaluation of a Simple Model of Vitrinite Reflectance Based on Chemical Kinetics (1). *AAPG Bulletin*, **74**, 1559-1570. https://doi.org/10.1306/0c9b251f-1710-11d7-8645000102c1865d

[21] Wygrala, B.P. (1989) Integrated Study of an Oil Field in the Southern Po Basin, Northern Italy. Dissertation Thesis, Berichte Kernforschungsanlage Jülich, University of Köln, 217.

[22] Peters, K.E. (1986) Guidelines for Evaluating Petroleum Source Rock Using Programmed Pyrolysis. *AAPG Bulletin*, **70**, 318-329. https://doi.org/10.1306/94885688-1704-11d7-8645000102c1865d

[23] Tscherny, R.G. (2006) Numerical Simulation of the Thermal Evolution and Basin Development of the Permo-Mesozoic Sudalpins (Dolomites) along the Trans Alp Traverse. Dissertation RWTH Aachen University.

International Journal of Geosciences, 2026, 17(1), 14-37
https://www.scirp.org/journal/ijg
ISSN Online: 2156-8367
ISSN Print: 2156-8359

Petrology and Geochemistry Study of the Basaltic Rocks of Tchaga South East of Fitri Lake-Chad: Metallogenic Implication

Tekoum Leontine[1,2*], Mady Esaie[1,2], Klamadji Moussa Ngarena[3], Jean Claude Doumnang Mbaigane[1,2], Rochette Pierre[4]

[1]Laboratory of Geology, Geomorphology, and Remote Sensing, Faculty of Exact and Applied Sciences, University of N'Djamena, N'Djamena, Chad
[2]Laboratory of Hydro-Geoscience and Reservoir, Department of Geology, Faculty of Exact and Applied Sciences, University of N'Djamena, N'Djamena, Chad
[3]Department of Mining and Geology Engineering, Faculty of Earth and Life Sciences, University of Pala, Pala, Chad
[4]National Centre for Scientific Research, Research Institute for Development, National Research Institute for Agriculture, Food and the Environment, Aix-Marseille University, Aix-en-Provence, France
Email: *leontinetekoum@yahoo.fr, madyesaie@gmail.com, doumnag@gmail.com

How to cite this paper: Leontine, T., Esaie, M., Ngarena, K.M., Mbaigane, J.C.D. and Pierre, R. (2026) Petrology and Geochemistry Study of the Basaltic Rocks of Tchaga South East of Fitri Lake-Chad: Metallogenic Implication. *International Journal of Geosciences*, **17**, 14-37.
https://doi.org/10.4236/ijg.2026.171002

Received: December 25, 2024
Accepted: January 11, 2026
Published: January 14, 2026

Abstract

In this paper, we present the new data from the study area. Located in the Southeast of Fitri Lake, at the center of the Republic of Chad in the Batha region, our study sector is an excellent metallogenic province, characterized by the presence of meta-volcano-sedimentary rocks. Based on petrography and geochemistry findings, these meta-volcano-sedimentary rocks are: the metavolcanites (metabasaltes, metadacites) and the metasediments (metaconglomerates, and marbles), covered by quaternary sedimentary formations (clay and sandstone). These *rocks* are crosscut by quartz-veins and a vein network hosting pyrite, chalcopyrite and gold mineralization. In the TAS classification we identify two lithological rocks of basaltic and dacitic composition. In the AFM ternary diagram, some rocks plot into the tholeitic field and others in the calco-alkaline domain, but have higher tholeitic tendency suggesting that the rocks have been crystallized from a similar parent magma. The high loss on ignition (LOI) values from 2.26 to 11.65 wt. % suggesting probably the contribution of secondary hydrated and carbonate phases. The variable contents of MgO, Mg# (36.09 - 67) and transition elements (Sc, Cr, Co, Ni) of the meta-volcanic rocks studied suggest that a certain degree of fractional crystallization occurred during the emplacement of meta-volcanic rocks. The Haker diagram shows a trend of negative evolution with the exception of the Al_2O_3vs SiO_2 diagram which shows a positive trend. The high enrichment of Th, Rb, Cs, K and Y, Zr, Hf, Sr shows a negative anomaly and subduction tectonic setting. Based on Chondrite and primitive mantle spider diagrams, LREE have been enriched to HREE in this area. The Th/Yb VS Nb/Yb diagram shows that, these rocks are original MORB of the oceanic arcs which have been enriched to the Metadacites of the continental arcs.

Keywords

Meta-Volcano-Sedimentary Rocks, Meta-Andesite, Metallogeny, Tchaga, Fitri Lake, Chad

1. Introduction

The Batha region is one of the largest regions in Chad, accounting for more than 22% of the country's total land area. In this region, previous studies are much more oriented towards the search for water for which several exploratory boreholes have been drilled. [1] [2] studied tertiary and quaternary formations for the preparation of a soil map for the recognition of Bokoro. [3] published a synthesis on the geophysical work carried out by the Office of Scientific and Technical Research of Overseas (ORSTOM), this work revealed a very important positive anomaly.

It extends in a general direction SW-NE from the east of Massenya to Ounianga Kébir in the north and even beyond to the Erdis Basin passing through the whole eastern half of the Chad Basin; [4] carried out the work of geochemical prospecting as part of the activities of the project to strengthen the Direction of Geological and Minières (DRGM), for the purpose of verifying the gold indices of the Precambrian metamorphic base and in the intrusive granites was reported.

In and around Chaga, the work of [5] as part of the project strengthening the DRGM showed some formations such as quartzites, granites, granodiorites, laterites and Metaconglomerates. These formations are similar to those of Mayo kebbi where many economic deposits are found along the southern margin: gold, uranium, copper, chromium, and nickel. The exposed part of this terrane is made up of metavolcanics and metasedimentary intruded by late-to post-tectonic granites and diorites most of which have different radiometric ages [6]-[8]. The Batha igneous formation is poorly surveyed, particularly with regard to petrographic, geochemical and geochronological studies.

Despite this work carried out in the area, as far as geology is concerned, the Batha region remains little known today, it is nowadays the covetousness of mining companies since the last gold rush of 2016 without any real knowledge of the geology, these formations mentioned above would show an economic interest and that could be explored and of course exploited to boost the economy of the region in particular and of Chad in general. In the present study, the field observations, petrography, geochemical and metallogeny data of the igneous rocks in the Batha region are presented. The approach of this study is therefore entirely suitable for providing new data on the of metavolcanics rocks and to discuss the geodynamic context in the Pan-African orogens.

Location of the Study Area, Hydrology and Geological Setting

The Batha Region, located in the center of the Republic of Chad between 12˚12′50″ North and 18˚20′10″ East, named after the Batha River, is one of the largest regions of Chad with a population of 527,031 inhabitants in 2009 with a density of 5.9 hab/km [9]. The Region includes six administrative departments including the department of Fitri where our study area is located, in the permits of the GMIA Minerals group near the village of Tchaga, 75 km northwest of the large city of Bokoro, connected to the capital Ndjamena by an asphalt road located approximately 300 Km. There is an airstrip at Ati 80 km to the North-East, the nearest port is 1470 km away in Douala in Cameroon as shown in **Figure 1**.

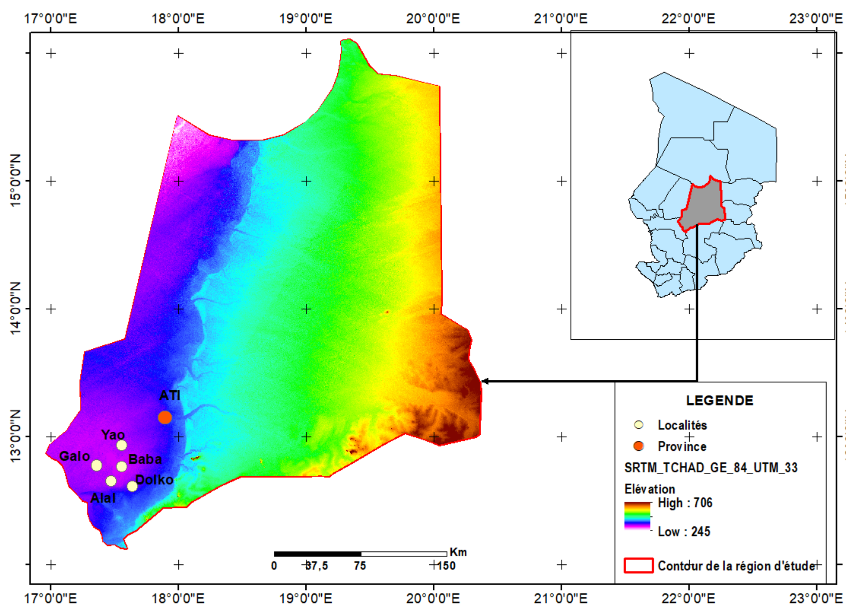

Figure 1. Map of the study area.

Hydrographic Network Made up of a set of intermittent oadis, the most important of which are the ridjil Djaya which takes its source about twenty kilometers north of Bitkine, Barh Zerzer to the north Gueria and Barh Zila to the South East of Ati Ardebé and the big watercourse, the Batha which runs along the town of Ati has its source in Sudan [5]. All these watercourses are temporary and all flow into Lake Fitri constituting a perennial waterbank as shown in **Figure 2**.

Chad is located in the middle of a vast domain called the "Pan-African Mobile Zone" between the West African Craton in the South-West and the Nilotic Craton in the North-East [10]. The African Orogenic Belt that recorded both Paleoproterozoic and Neoproterozoic juvenile accretion to the west. From recent investigations, it has been argued that the Mayo Kebbi massif was formed during the Neoproterozoic in response to the closure of an ocean involving juvenile accretion related to an active margin tectonic setting [7] [11].

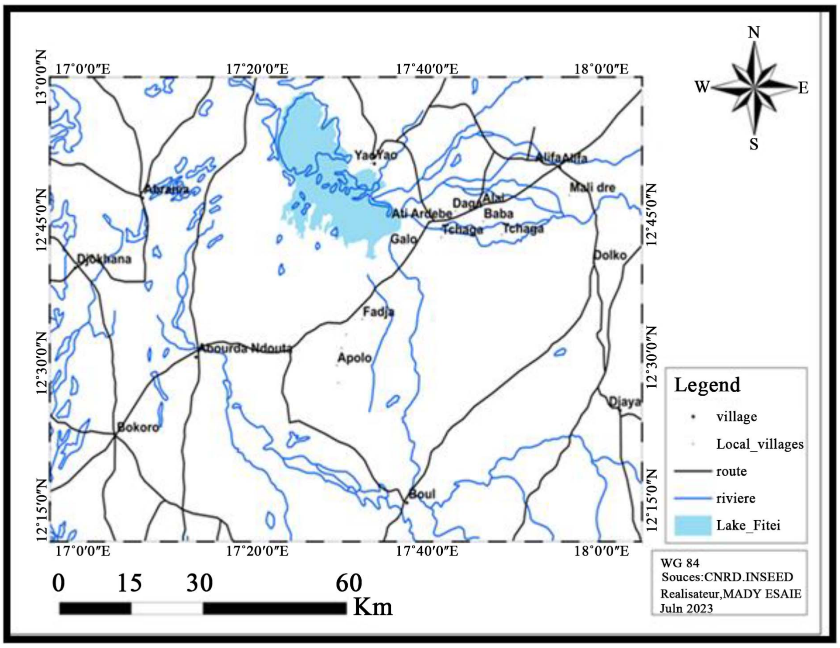

Figure 2. Hydrographic map of the study area.

The pan-African tectono-thermal event represents the last active orogeny on Chadian territory and the rocks formed or influenced by this event constitute the bulk of the crystalline massifs (Tibesti Ouaddaï, massif central, Mayo kebbi and Yadé). Now Chad is part of a stable block. Its geological history since the beginning of the Paleozoic is marked by the deposition of sedimentary platform formations over most of the territory. Paleozoic sediments accumulate in the north and east of the country following the latest pan-African tectonic shift. The posterior tectonics and the surrection of Tibesti and Ouaddaï limit sedimentation in the Erdis and Djado basin, which occupy northern Chad and adjacent regions [12]-[15]. The crystallophyllian rocks and Precambrian granitoids of Tibesti in the north, Ouaddai in the east, Guera in the center, Mayo-Kebbi in the southwest, and Mbaibokoum in the south correspond to the basement [16].

According to the regional geology in Batha, there are three stratigraphic units, namely, the gneiss-migmatite complex, the shale belt, and the pan-African granitoids as shown in **Figure 3**.

The migmatite gneiss complex reflects the ages between the Archean and early Proterozoic isotopic ages [17].

The rocks have undergone metamorphism under amphibolite facial conditions [18]. Complex structural units are evident in this stratigraphic unit and have in turn been invaded by the granitoid plutons of Pan-African magmatism [17]. Shale belts are of late Proterozoic Age and were deposited and metamorphosed with the base migmatite gneiss complex during pan-African orogenesis.

Shale belts are associated with a complex geological structure and tend to be N-S and NNE-SSO and contain assemblages of igneous rocks, politic sediment, and ribbed iron formations. They were further deformed and underwent a shale-green metamorphism.

Granitoids are tectonic late pan-African intrusions of granites, granodiorites, and diorites with gabbros and syenites. They occur mainly under the small subcircular [19]. The regional geological structure is either of a very tense area, or the mother rocks are highly deformed, laminated and affected by ductile and brittle shear zones [17]. According to local geology, specifically the Tchaga area, from field observations we identified meta-volcanic rocks covered by quaternary sediments with an average thickness of 1m, with poorly sorted and polymeric well-rounded sediments, and angular quartz fragments derived from quartz veins. This formation is in turn covered with dark gray clay soil ranging from 0 to 100cm, and recent gravel sometimes covers the clay soil as shown in **Figure 3**. Metavolcanic rocks are exposed in some places and are traversed by many quartz veins, as well as a conglomerate strip, which is traversed by quartz veins. The conglomerates have a dip varying between 15˚ and 20˚ and an azimuth of 120˚. They are composed of well-packed, polymeric and poorly sorted clasts ranging from stones to rocks; the matrix is basaltic of greenish gray color. They are sporadically flush according to an orientation as a function of the nesting. This is attributed to a 500 m fault in the geological structure or a 50m fault to the East that re-exposes the sediments [20]. The flush quartz veins have a thickness ranging from 15 cm to 2 m with an azimuth of about 205˚ on average and a dip of 45˚ subvertically. These quartz veins are post-volcanic and their Age remains to be determined [20].

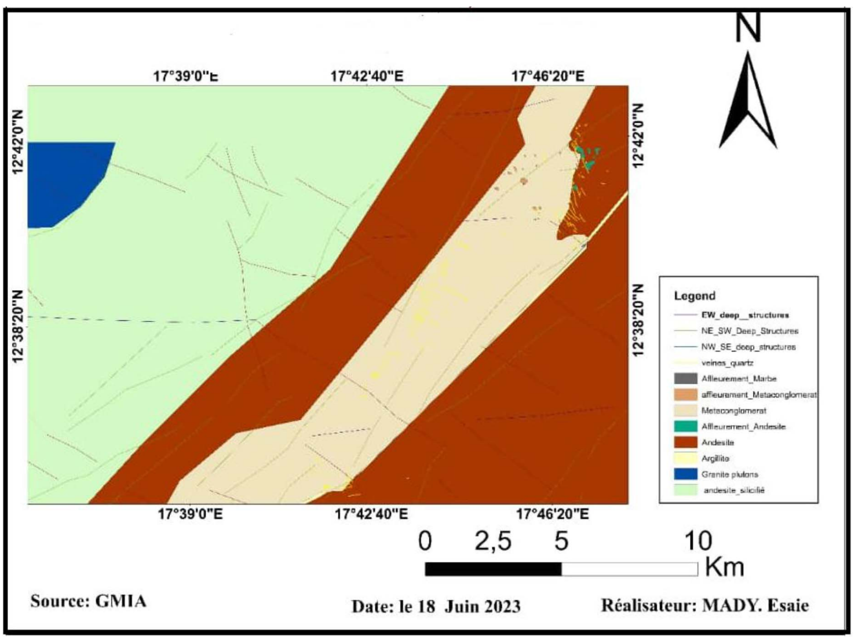

Figure 3. Geological map of the study area.

2. Material and Methods

2.1. Material

A total of thirty-four (34) fresh and representative metavolcanic samples were selected based on their health and degree of alteration for petrographic and geochemical studies. The sample was carefully cleaned and then sawn into two rock sugar cubes. Ten (10) rock cubes were ground (pretreatment) at the laboratory of GMIA MINERALS group while ensuring that there is no contamination by applying the QAQC Chad and then sent to the ALS laboratory (South Africa) for geochemical analyses. The other ten (10) were sent to the thin-section at the Geosciences and Environment Laboratory (LaGE) of the University of Joseph kizerbo (UJKZ) in Ouagadougou, Burkina Faso. Twenty-six (26) samples were analyzed at the SGS laboratory to specifically determine the gold content by FAE (fire assay analysis).

2.2. Methods

For geochemical analysis, the analytical uncertainties vary from 0.1% to 0.04% for major elements; from 0.1% to 0.5% for trace elements; and from 0.01 to 0.5 ppm for rare earths. The remaining trace elements were analyzed by ICP-MME.

Loss on ignition or LOI (Loss on ignition) for ICP-MS and ICP-AES (Inductively Coupled Plasma Atomic Emission Spectrometry) analyses is also known as calcination. Its determination is done by heating the powders to the point that they release all their water bound to the particles. Once in solution, the samples were analyzed by Inductively Coupled Plasma-Atomic Emission Spectrometry (ICP-AES). The prepared samples were mixed with the $LiBO_2/Li_2B_4O_7$ flow. The samples were dissolved under a Teflon bomb pressure, using a 1:1 mixture of HF and $HClO_4$ at 180˚C, and then taken up in an HNO_3 solution with an international In-Re standard. After dissolution in HF-$HClO_4$, the samples were taken into a mixture of HNO_3, HCl and HF and diluted. These solutions were measured within 24 hours of dilution to prevent HFSE absorption. For major elements, a comprehensive major element analysis was performed by combining several methods in a single package. This package combines the entire whole-rock analysis package (ME-ICP06) in addition to carbon and sulfur, which are analyzed using a combustion furnace (ME-IR08). The elements SiO_2, Al_2O_3, Fe_2O_3, CaO, MgO, Na_2O, K_2O, Cr_2O_3, TiO_2, MnO, P_2O_5, SrO, and BaO were analyzed by ICP-AES. Twenty-six (26) samples were analyzed at the SGS laboratory to specifically determine the gold content by FAE (fire assay analysis) which consists of melting the sample at a temperature of more than 1000°C and separating the silicates from the metals by settling and then determining the percentage of gold.

3. Results

3.1. Petrography

A total of thirty-four (34) samples were taken according to their lithology at various sites, in Tchaga Base, Tchaga Est, Ndjarai and Iteim and around Tchaga village in the exploration licenses of the GMIA Mineral group where the exploration work has been carried out for more than four years for the search for gold and many other metals. The petrography of the Tchaga area shows a low diversity of rocks dominated by meta-volcanic and meta-sedimentary formations: specifically meta-basalts, meta-dacites, marbles and meta-conglomerates and a few vein rocks such as quartz veins.

3.1.1. Metavolcanic Rocks

The Meta Basalts

The Metabasalts are flush in the form of a pointing direction NW-SE (Figure 4).

Macroscopically, these rocks have a greenish to gray color, with a microlithic texture cut in some places by veinules made of white minerals or quartz veins. Minerals such as biotite, amphiboles and plagioclases are observed.

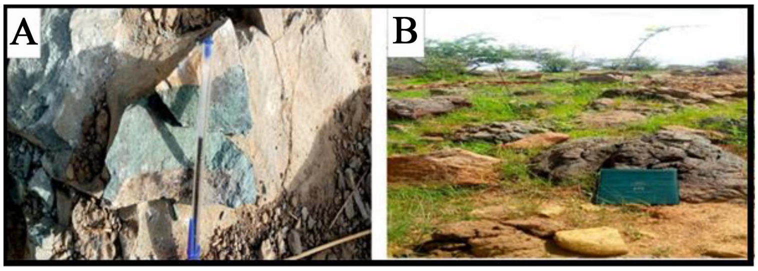

Figure 4. (A) and (B) showing the outcrop of the Meta basalts.

Microscopically, minerals such as olivine, amphibole-altered pyroxenes, and relics of phenocrystals of plagioclases, quartz, and micas are observed. Also chlorites, epidote and carbonates, quartz grains and oxides that would come from the alteration of ferromagnesian minerals (olivine, Amphiboles; Pyroxenes). The presence of opaque elements is also noted as shown in Figure 5, an alteration was noted which affected almost all rocks showing extensive destabilization of minerals on microscopy and fissures filled either with carbonates or hydrothermal fluids showing hydrothermal activity in the area.

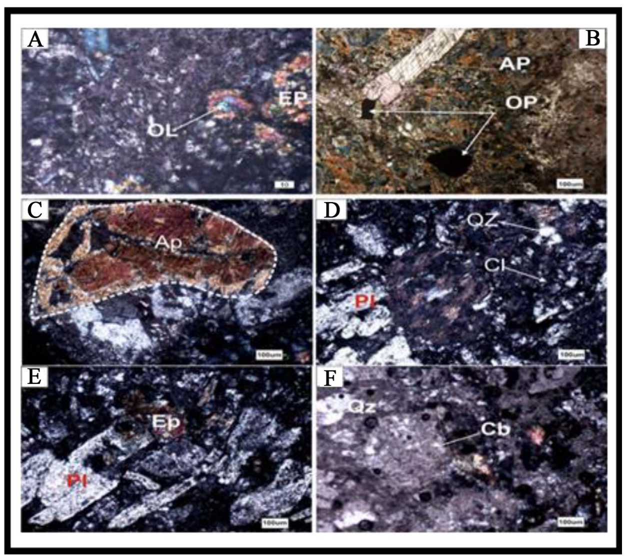

Figure 5. Microphotography of Metabasalts: Amp: amphibole; Pl: plagioclase; Qz: quartz; Ep: epidote; Cl: chlorite; Cb: carbonate; Op: opaque; Ol: olivine.

- Relics

Amphiboles (15%); they are large automorphs with cleavages forming angles of about 120˚. Olivines (5%); they are more or less altered and difficult to distinguish from the average size. Plagioclases (65%); they are large automorphs partially or completely destabilized with fine sometimes kinked twins showing small-scale deformities. Newly formed minerals include: epidote (5%): formed by altered plagioclases; quartz (4%): which are recrystallized quartz; carbonates (2%) also formed by alteration of plagioclases, opaque (1%) resulting from the alteration of olivines, chlorite (1%) derived from biotite. Quartz (2%): constituting the xenomorphic matrix of small size.

3.1.2. Metadacites

On macroscopy, the samples with cracks have a green color with a microlitic structure. Minerals are rarely visible as shown in **Figure 6**.

Figure 6. Metadacite Flush and hand specimen.

Microscopically, grains of quartz recrystallized in the subgrain, and plagioclases in mesostas are observed, followed by amphiboles, epidote, and a shearing quartz venule as shown in **Figure 7**. Relics are: amphiboles (15%), which have a mean cleaved size. Plagioclases (48%) were predominant in the medium sample size but a large proportion of the fine grains were in the matrix.

The newly formed minerals are: quartz (25%) forming the matrix with fine grains, carbonates (8%), which are the matrix of the rock and the opaque sulfides (4%), which are rarely automorphic.

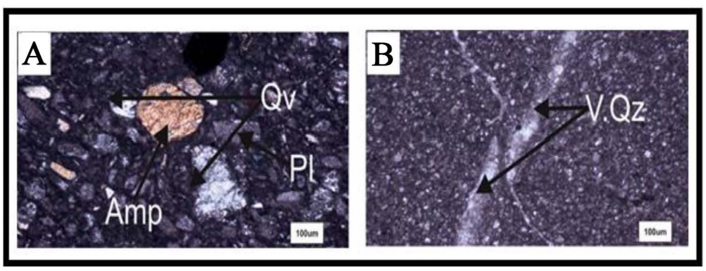

Figure 7. Microphotography of metadacites with a ruptured vein VQZ: quartz vein; Bt: biotite; Qz: quartz.

Metasedimentary Rocks

Metaconglomerates

For this purpose, two samples were taken to make the thin slides; one was cut, just from the matrix, and the other was all the rock that was cut. When observed macroscopically, these metaconglomerates are formed of polygenic medium-sized pebbles embedded in a green matrix as shown in **Figure 8**.

The Meta conglomerates are located in the eastern part of the Chaga village, more than 4 km wide and more than 30 km long. The conglomerates have dips varying between 15˚ and 20˚ and an azimuth of 120˚. These conglomerates are composed of clasts of granite, basalt, quartzite, flint and rarely quartz of millimeter to centimeter size. Our observations on the ground have allowed us to say that, given the size of the granite pebbles, which are generally smooth and rounded, testify to the power of the transport agent and the distance traveled which is important, and this makes us think of the mega lake whose bank is located not far from gueria and Zoubou at the origin of these important deposits.

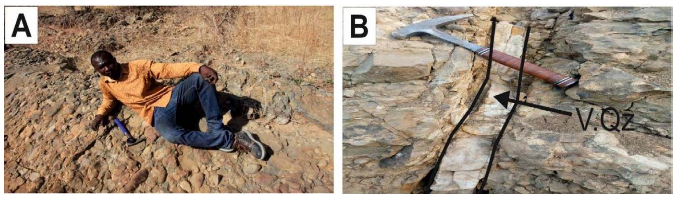

Figure 8. (A) Pebble in a conglomerate; (B) Conglomerate pass through a Quartz vein.

Microscopic observation of the matrix showed small quartz crystals, an abundance of carbonates and white micas that would likely have come from the alteration of plagioclases (**Figure 9(C)**), and some black minerals that could have been sulfides (**Figure 9**).

Under the microscope, the second sample, *i.e.* the entire rock, primary minerals, relics of plagioclases and white micas phenocrystals of small epidotes are observed, which are thought to have originated from the alteration of the plagioclases constituting the secondary minerals. The absence of ferro-magnesians would explain their fragility in the face of alteration.

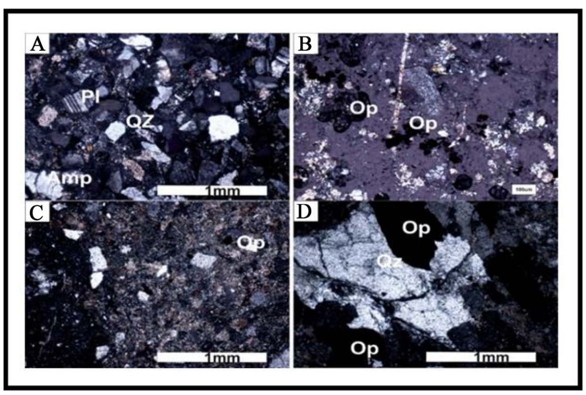

Figure 9. Conglomerate microphotography: Qz:quartz; Pl:plagioclase; Op:opaque.

Marbles

When observed macroscopically, the sample called marble, is yellowish gray in color with venules of impurities and some visible black crystals and quartz. Flush to the south in a ball with smooth faces and small holes that could be burrows, or are due to the dissolution of calcite in contact with acid from rainwater.

Structurally the geological formations are subjected to stresses that result in deformations that may not be visible. Field observations have enabled us to identify and measure various structures, including veins, diaclases and shears.

The veins observed in the study area are mainly quartz veins 15 cm to 3 m wide and generally over 50 m long, dipping from 45˚ to subvertical with a major N30˚E orientation observed in the meta-andesites and meta-conglomerates (Figure 10(B) **and** Figure 10(C)). Diaclases are observed in almost all the Tchaga formations, especially the Meta basalts, Meta conglomerates and Meta dacites. (Figure 10(A)). In the Meta basalts, two main directions are observed, one at N45˚E and the other at N60°E. In the Meta conglomerates, the directions are more or less uniform, mostly around N50E. Shears are observed specifically on quartz veins with horizontal movements whose striations are observed on the faces of quartz veins showing horizontal movement in the same direction as the quartz veins (Figure 10(D)). These movements are responsible for the brecciation of the quartz veins, which are carried away by erosion and deposited at the foot of the veins, forming gold-bearing sediments.

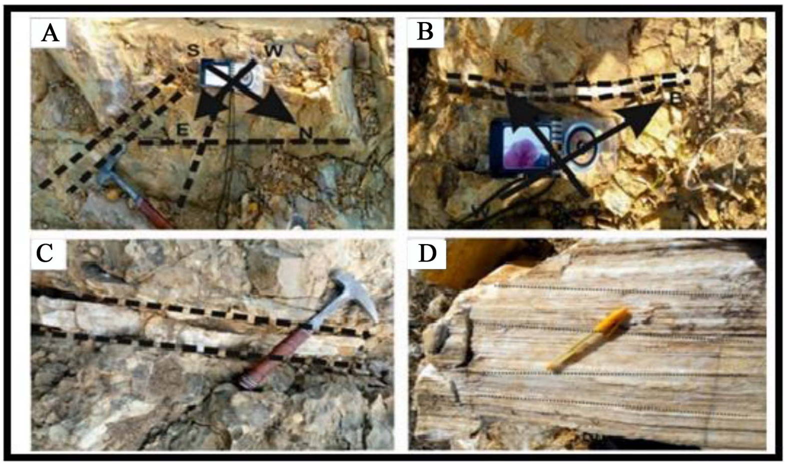

Figure 10. The outcrop showing the deformations that the rocks have undergone, (A) shearing on the Metabasalts, (B) and (C) quartz vein and (D) shearing.

3.2. Geochemical

Geochemical Characterization

Ten (10) samples were analyzed at the ALS Chimex South Africa (pty) Ltd. laboratory in Johannesburg, South Africa, for major, trace and rare earth elements.

The major elements summarized in Table 1 as a function of the different lithologies show high silica contents in the Meta-dacites which vary between 66.4% - 69.1%, in the Meta-basalts the silica values vary between 48% - 51.6%. The loss on ignition of the samples is very high, ranging between 2.73% - 11.65% We also note higher alkali values in the Meta-dacites compared to alkalis in the Meta-basalts. High iron values are observed in all lithologies varying between 5.1% and 14% while the MgO content is very low 1.6% - 9.47% apart from the elements SiO_2, Al_2O_3, Fe_2O_3, CaO, MgO, the elements CrO_3, TiO_2, MnO, P_2O_5, SrO, BaO have very low contents (**Table 1**).

In the SiO_2-K_2O diagram of [21], the metavolcanics rocks are transitional between the tholeiitic and subalkaline domains. Three (3) rocks (Metadacite) have a high potassium character, in medium they belong to the calco-alkaline domain (**Figure 11(A)**), other rocks (metabasalts) belong to the domain of the tholeitic series with low potassium contents. In the Na_2O + K_2O versus SiO_2 diagram [22] all samples are subalkaline (**Figure 11(B)**). On the ternary diagram of [23], used to discriminate the tholeiitic and calc-alkaline suites, some samples plot in tholeiitic domain (**Figure 11(C)**) suggesting that, the mafic rocks were crystallized from similar parent magma.

Analytical results plotted in the TAS classification diagram [24], have enabled us to identify two lithological units of basaltic and dacitic composition.

In addition, the lower Na_2O + K_2O ranging from 0.52 to 3.05% and the Na_2O content are higher than K_2O indicating that Na is also more enriched than K in the basalt. The low alkali contents are typical of the tholeiitic domain [25] [26].

The first geochemical studies carried out in this area demonstrated the oceanic provenance of the tchaga metabasites rock.

The major chemical analyses show a linear correlation between AL_2O_3, Na_2O and MgO, due to plagioclase fractionation. At the same time, the linear correlation between FeO, MnO and MgO suggests that both ortho-and clinopyroxene are the main ferro-magnesian phases that fractionated during the differentiation processes. The chemical pattern might be the result of a fractional crystallization process, which mainly involves pyroxene and plagioclase.

On the other hand, the variation in the refractory element (Ti, Cr, v) contents is consistent with the fractionation of ferro magnesian phase of orth- and clinopyroxene, hornblende and also with the accumulation of the pyroxene.

Moreover, Eu anomaly is negative in the accumulation phase and slightly positive in others facies. This shows the importance of plagioclase fractionation in the metabasic rocks.

The geochemical results show that the loss on ignition of the samples is very high, ranging between 2.73% - 11.65%, and is due to the effects of the metamorphic and hydrothermal phenomena affecting these formations. Altered rocks will contain variable proportions of Zr and Ti, caused by mass gains and losses, but the Zr/Ti ratio will remain constant as these elements are immobile in volcanic rocks [27] [28]. Potassium-poor rocks (K2O < 1% by weight) tend, before metamorphism, to incorporate this element into mafic phases such as biotite. Note in this regard that our petrographic study leads us to believe that some of the samples may contain accessory quantities of primary biotite [29].

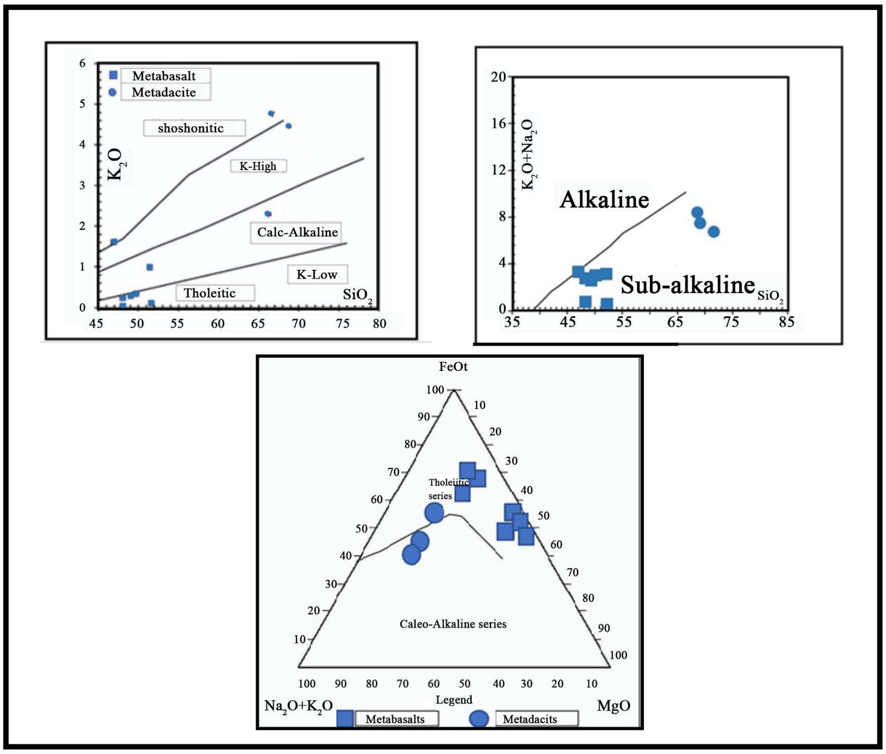

Figure. 11. (A) (Peccerillo and Taylor 1976); (B) SiO_2-(K_2O+Na_2O); Irvine and Baragar 1971 (C) Alk-FeO-MgO applied to Tchaga meta-volcanic formation.

Table 1. Modal mass results of major and trace elements of Metabasaltes, Metadacites.

Elements	23TCH 038	23TCH 01	23TCH 02A	23TCH 02B	23TCH 05A	23TCH 08A	23TCH 021A	23TCH 010	23TCH 011	23TCH 037
SiO_2	48	46.9	48	51.6	49	51.4	49.7	66.4	69.1	66.9
Al_2O_3	13.75	16.9	13.15	15.9	12.95	15.75	9.04	15.65	12.65	13.9
Fe_2O_3	9.15	8.32	13.3	9.79	14	8.54	13.15	5.4	5.43	5.1
CaO	12.85	9.87	6.35	6.65	6.2	9.57	10.6	1.33	0.13	2.94
MgO	9.3	2.82	4.44	8.37	3.97	7.32	9.47	1.66	1.94	1.9
Na_2O	0.46	1.44	2.49	0.41	2.1	1.9	2.42	5.37	1.71	2.08
K_2O	0.23	1.61	0.03	0.11	0.28	0.99	0.34	2.29	4.44	4.75
Cr_2O_3	0.088	0.011	0.002	0.045	0.004	0.049	0.151	0.005	0.004	0.012
TiO_2	0.39	0.48	1.75	0.46	1.88	0.44	0.45	0.59	0.36	0.59
MnO	0.19	0.2	0.13	0.14	0.19	0.17	0.44	0.11	0.05	0.11
P_2O_5	0.14	0.2	0.19	0.15	0.19	0.21	0.15	0.15	0.02	0.15
SrO	0.02	0.05	0.01	0.05	0.01	0.07	0.02	0.02	<0.01	0.04
BaO	0.02	0.06	<0.01	0.01	0.01	0.04	0.07	0.06	0.09	0.09
LOI	4.63	11.65	10.3	7.67	9.94	4.4	3.09	2.26	5.08	2.73
Total	99.22	100.51	100.14	101.36	100.72	100.85	99.09	101.3	101	101.29
$Na_{20}+K_2O$	0.69	3.05	2.52	0.52	2.38	2.89	2.76	7.66	6.15	6.83
Ba	846	148.5	489	17.2	97.3	83.3	396	533	777	662
Ce	48.3	13.8	16	16.6	12.4	17.2	18.6	28.5	264	9.3
Cr	90	666	78	14	322	29	365	37	27	1170
Cs	5.4	0.08	0.89	0.06	0.16	0.29	0.3	0.39	0.97	0.02
Dy	4.64	1.98	2.36	5.16	1.98	5.79	2.45	4.2	25.1	2.16

Continued

Er	2.73	1.14	1.4	3.2	1.22	3.41	1.51	2.52	15.25	1.24
Eu	1.09	0.66	0.78	1.39	0.68	1.54	0.85	1.3	3.95	0.64
Ga	20.3	15.8	16.4	22.9	16.7	20.5	17.2	18.7	43.7	8.5
Gd	5.01	2.21	2.46	5.05	2.15	5.34	2.53	4.42	22.6	2.25
Hf	5.03	0.74	1.13	2.98	0.79	3.25	1.16	3.83	31.3	0.72
Ho	0.92	0.43	0.47	1.08	0.41	1.14	0.5	0.88	5.33	0.44
La	23.2	7	8.1	6.6	6.5	6.6	9.6	13	138.5	4.1
Lu	0.39	0.19	0.21	0.44	0.2	0.46	0.25	0.38	1.9	0.18
Nb	10.05	1.03	2.55	5.23	1.1	5.33	2.4	6.82	243	1
Nd	25.1	8.3	10	13.3	7.8	14	11.2	17.4	118.5	7.6
Pr	6.11	1.8	2.18	2.63	1.76	2.79	2.44	3.98	30.5	1.46
Rb	191.5	3.3	41.3	0.8	2.6	5	24.4	35.7	305	7.7
Sm	5.43	2.12	2.32	4.06	2.01	4.26	2.62	4.5	23.8	2.26
Sn	2.2	<0.5	<0.5	0.6	<0.5	0.7	<0.5	0.8	10	<0.5
Sr	334	156	411	68.9	411	110	551	170.5	26.6	132.5
Ta	0.9	1.9	0.1	0.3	0.1	0.3	0.1	0.5	14.6	<0.1
Tb	0.82	0.31	0.4	0.89	0.35	0.94	0.43	0.72	4.12	0.39
Th	9.25	1.21	1.22	0.48	1.06	0.48	1.42	2.63	26	0.54
Tm	0.39	0.18	0.22	0.44	0.19	0.45	0.21	0.36	2.05	0.18
U	3.04	0.37	0.44	0.42	0.32	0.27	0.48	0.71	5.84	0.05
V	95	255	223	373	256	387	220	86	8	199
W	9.3	<0.5	1.7	4.4	10.9	1.7	<0.5	10.5	15.2	10.4
Y	26.9	11.2	13.7	29.8	11.7	30.7	14.3	23.1	141	12.5
Yb	2.68	1.17	1.42	3.1	1.27	3.09	1.52	2.54	13.9	1.25
Zr	166	27	39	107	27	112	41	135	1240	26

The Hacker diagram of major elements as a function of SiO_2 shows two groups of rocks, the metabasalt and the metadacite. The whole diagram shows a negative trend except for the Al_2O_3 Vs SiO_2 diagram as shown in **Figure 12**. The decrease of these oxides in the magma is due mainly to the fractionation of plagioclases.

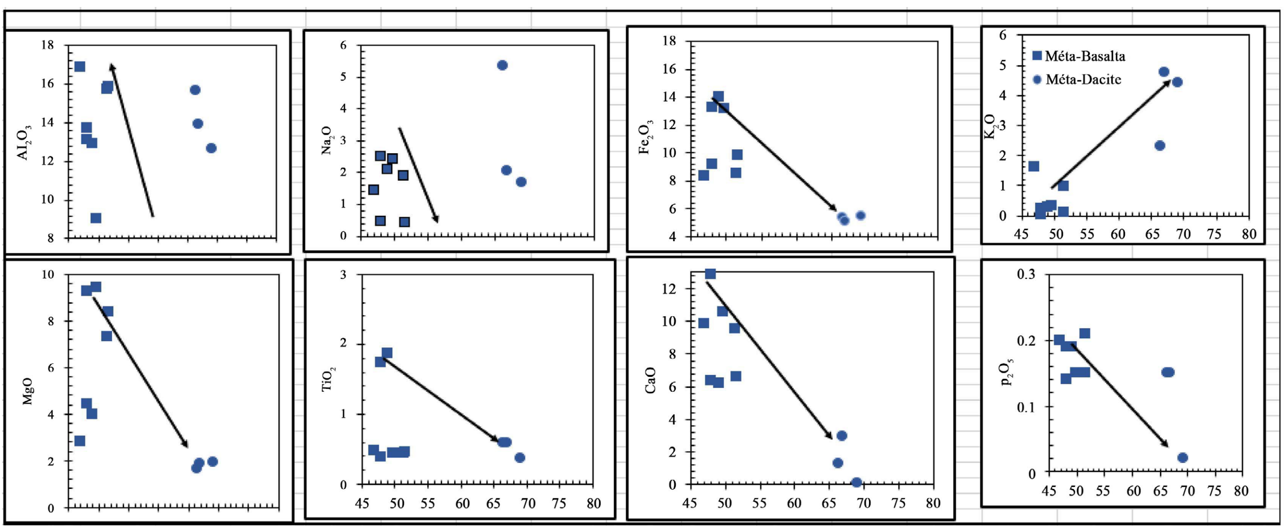

Figure 12. Hacker diagram showing the evolution of the major elements as a function of SiO_2 of the metabasalt, and metadacit of the study area.

Rare Earth Spectrum

In the Chondrite-normalised REE patterns for metavolcanics rocks from Study Area (Chondrite Normalized values are from Boynton 1984) we note the strong negative Nb, Ce, Eu, Sr and Zr anomaly in the metabasalt and metadacite, these samples have a rare earth spectrum marked by a slight negative anomaly in Eu with (δEu ranges from 0.85 to 1.39) and negative anomaly in Nd, having a more or less constant negative appearance at the level of the light rare earths (LREE) and a progressive depletion in heavy rare earth (HREE) as shown in **Figure 13(A)**. Metadacite has a very pronounced negative anomaly in Eu, with (δEu ranges from 0.6 to 3.95) due to the plagioclase fractionation and a very significant depletion of the heavy rare earths from Y to Lu (**Figure 13(B)**).

The high content of Cr and Ni indicated by the parental magma had been derived through partial melting of the peridotite mantle source, and suggested the presence of olivine and clinopyroxene fractions in the tchaga rocks [30] [31]. The concentration of Sr and Zr, in the tchaga rock sample study had relatively high contents. The Sr ranged between 26.6 to 551 ppm with an average of 289 ppm, Zr content between 26 to 1240 ppm with average of 635 ppm (**Table 1**). Vanadium concentration ranges between 8 and 387 with an average of 200 ppm. Vanadium and Titanium have a comparable behaviour in melting and crystallization processes; these elements provide a useful signal for the fractionation of Fe-Ti oxides (such as ilmenite) [32].

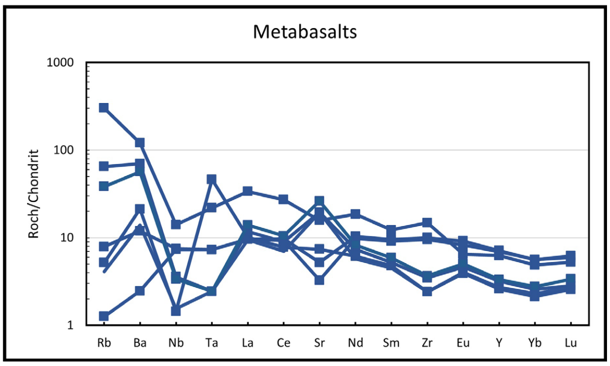

(A)

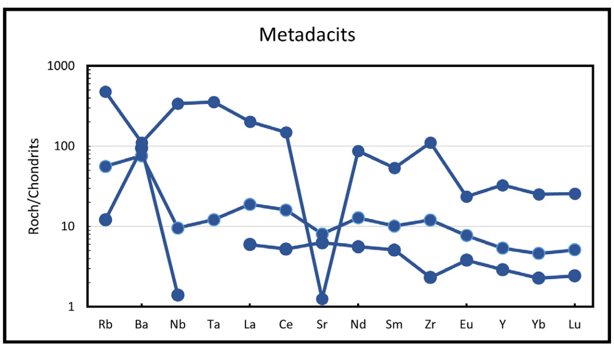

(B)

Figure 13. (A) and (B): Chondrite-normalised REE patterns for metavolcanics rocks from Study Area (Chondrite Normalized values are from Boynton 1984) Note the strong negative Nb, Eu, Sr and Zr anomaly in the metabasalt and metadacite.

In the Multielement variation patterns for the various rocks normalized to primitive mantle values of [33], we note the strong negative Nb, K_2O, Sr, Zr and Ti, P_2O_5, Y anomaly and positive en K_2O, Rb, Ta, anomaly in the metabasalt and metadacite as shown in **Figure 14**. Normalization of multielement to primitive mantle indicates losses of Ba, Ti and Cs which can be caused by the fractionation of plagioclase, apatite and ilmenite. The Ba anomaly is also controlled by the presence of K-feldspar and mica. The observed Ti anomalies are due to the fractionation of magnetite indicating a subduction environment (or remelting of a source from a subduction environment). Positive anomaly of Rb may have happened due to contamination of magma with crustal (due to the high concentration of these elements in the continental crust). In the primitive mantle normalized (**Figure 14**) enrichment from LREE and HREE was observed in all samples. Enrichment of LREE elements is higher than HREE and the negative gradient of the graph indicates the higher amount of LREE than HREE that conforms with the overall pattern of spider diagrams subduction zones.

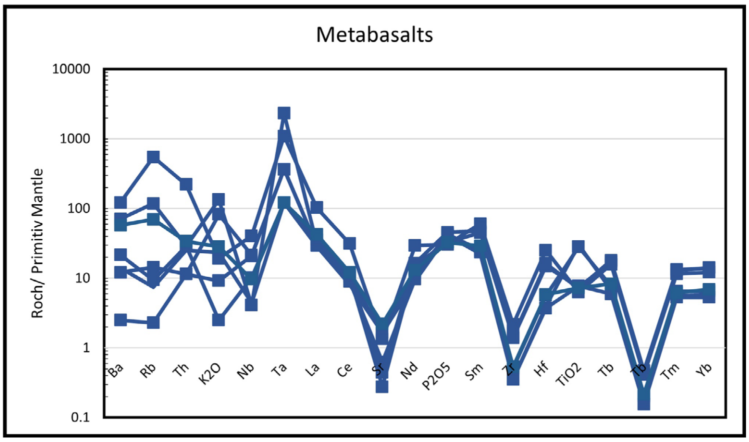

(A)

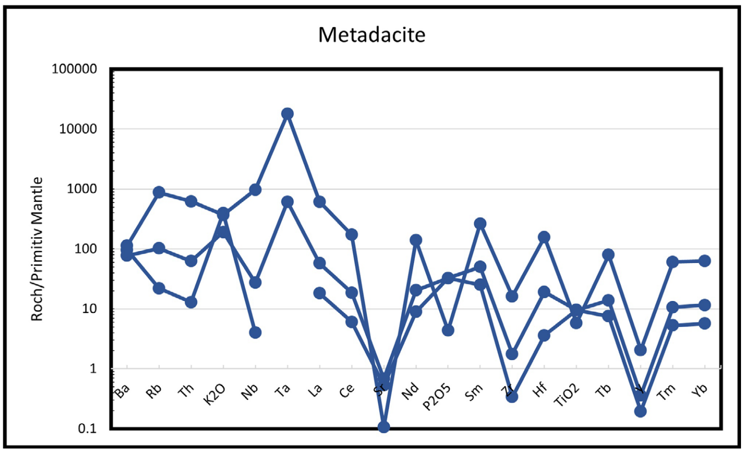

(B)

Figure 14. (A) (B) Multielement variation patterns for the various rocks normalized to primitive mantle values of [33], we note the strong negative Nb, K_2O, Sr, Zr and Ti, P_2O_5, Y anomaly and positive en K_2O, Rb, Ta, anomaly in the metabasalt and metadacite.

Geodynamic context

The geodynamic context of the tchaga region is debated, the geochemical analysis shows that, in the [19] diagram, all samples are subalkaline, in the ternary diagram, some samples plot in the tholeiitic domain, characteristic of oceanic dorsal or oceanic arc. The other samples plot in the calco alcaline field, the high loss on ignon of the sample suggests their origin on the oceanic arc. The Tchaga area from which the petrographic and geochemical studies are conducted has several deformation structures with quartz veins oriented mostly N30E whose geophysical studies have also revealed three main directions NW-SE, NE-SW and E-W.

The analysis of the field stratigraphic data showed that the volcanic Meta facies would have been first put in place after which the deposition of the conglomerates occurred, since these conglomerates consist mainly of basalt clasts, granite and quartz veins cross the basalts and the conglomerates, which would show that these veins are late in relation to the surrounding rocks.

On the Th/Yb versus Nb/Yb variation diagram of [34], used to distinguish the conservative and nonconservative behaviour of Ti, Th, the mafic lava invariably displays a higher Th/Yb ratio than MORB confirming the status of Th as a nonconservative element. We note that, the mafic lava has a spread of ratios comparable to that of MORB indicating that the mantle source of volcanic arc basalt may be enriched and depleted with respect to an average N-MORB source. The igneous rocks plot in the field of the oceanic arcs and continental arc show that these samples are MORBs of oceanic arc in origin that have enriched to the Meta Dacite of continental arcs as shown in **Figure 15**.

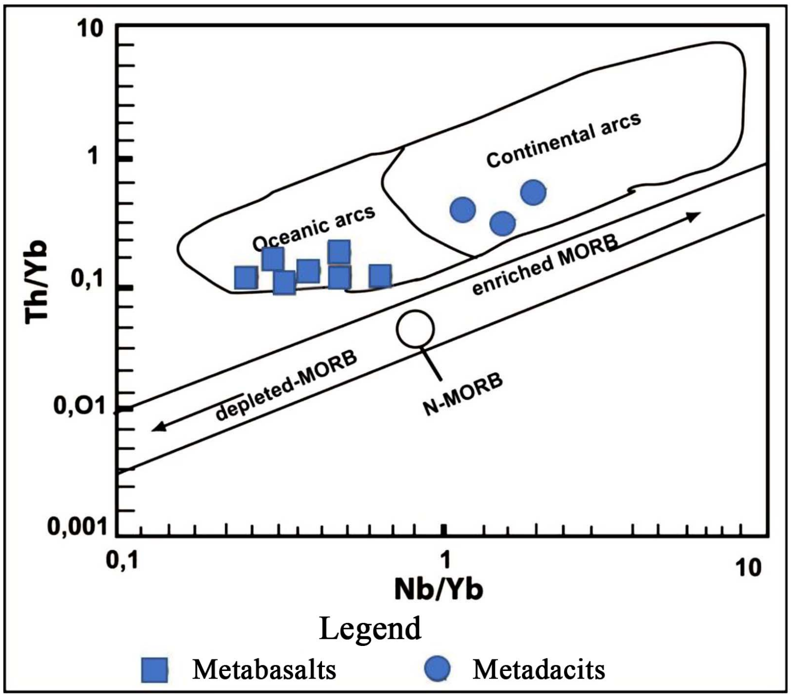

Figure 15. Pearce and Peate (1995); MORB: Medium oceanic wrinkle basalts; E-MORB: Medium oceanic wrinkle basalts enriched.

Metallogenic of gold forming mineralisation metallic deposit

Fieldwork, the geological environment of the study area and geochemical analyses of the samples revealed some evidence of mineralization. Gold is native in quartz veins as shown in Figure 16(A) and nuggets in eluvium deposited around vein fields as shown in Figure 16(B). Mineralization in this zone occurs as pyrites, chalcopyrite as shown in Figure 16(C) and Figure 16(D) and arsenopyrite, which are often combined with carbonates. A macroscopic observation of some nuggets found by artisanal gold miners in this area, given the angular and rough shapes, gives information on the origin and distance traveled. These nuggets would probably have originated from the quartz veins located nearby. As a result of the erosion phenomenon, gold is released and deposited just at the foot of the veins. Five (5) thin plates were metallized to allow observation and identification of metals as shown in Figure 17(A) and Figure 17(B).

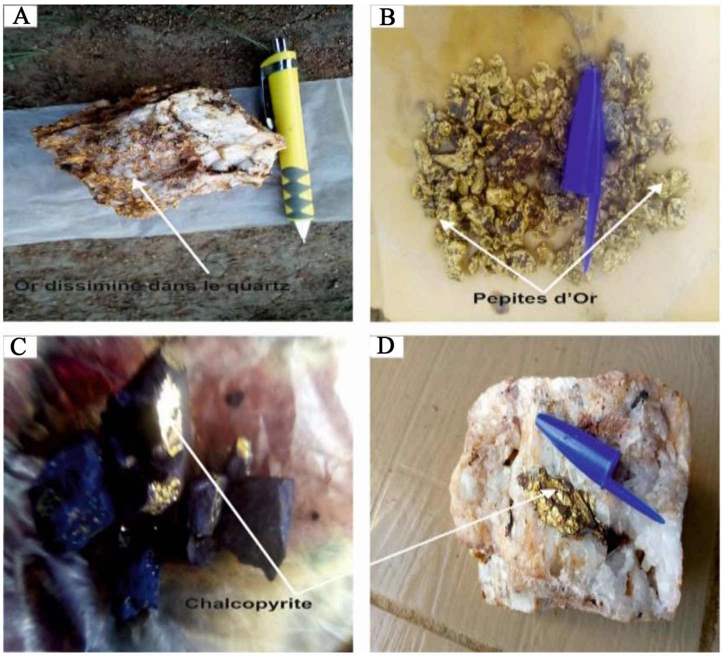

Figure 16. Photography of gold and pyrite in quartz and gold nuggets.

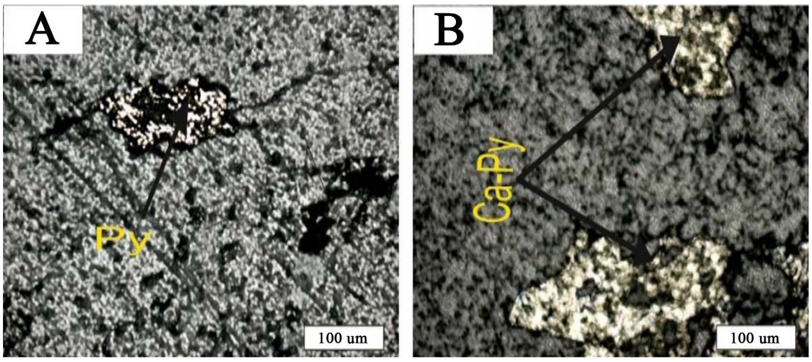

Figure 17. Microphotograph of a conglomerate in natural light. Py: Pyrite, Ca-Py: Chalcopyrite.

In metallogeny, a metal deposit is a geological formation in which the chemical element being exploited is at a much higher content than Clarke's of that element. The Clarke value is the average concentration of a chemical element in the earth's crust.

The studied elements compared with Clarke show higher levels than Clarke in some rock samples, for example uranium in Metadacite and Metasalts.

According to the analysis result our deposits belong to the deposit of ferrous and non-ferrous metals.

- Ferrous metals: The chromium in the basalt has a higher content than Clarke and the usable content is (0.02%) as shown in **Figure 18(A)**.

- Non-ferrous metals Copper has a content exceeding Clarke, and an exploitable value of 0.0045%. as shown in **Figure 18(B)**. Nikel has a value far greater than Clarke content; the exploitable content is 0.008 as shown in **Figure 18(C)**. The Cobalt content is higher than Clarke with a value of 0.0023% as shown in **Figure 18(D)**. Vanadium has a higher content than Clarke with a usable value of 0.011% as shown in **Figure 18(E)**. Zirconium has a very high value compared to Clarke with a value of 0,016% as shown in **Figure 18(F)**.

Twenty-six (26) samples were analyzed for gold content. 80% have a content varying between 1 and 9 ppb showing very low content and especially in rocks such as meta conglomerates and meta basalts, the remaining 20% have contents varying from 45 to 351 ppb, the highest content is that of quartz samples followed by conglomerate. The usable content of gold is 103. ppb. It is the artisanal mined metal in the Batha area today. Since the 2016 gold rush, the operation uses metal detectors to detect nuggets ranging from 0.5 g to 25 g in eluvium. Briefly, the few deposit indices represented by these metals described above in the rocks analyzed show positive anomalies; these metals are potentially exploitable subject to advanced studies for the evaluation of their tonnage to really prove the reserve.

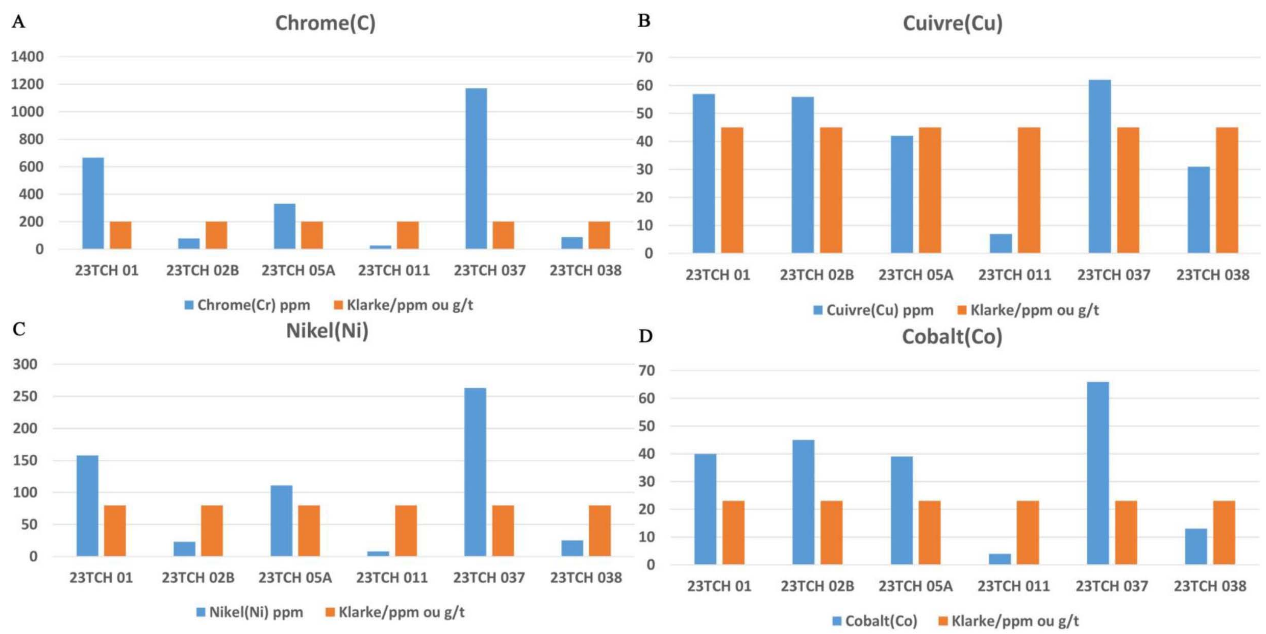

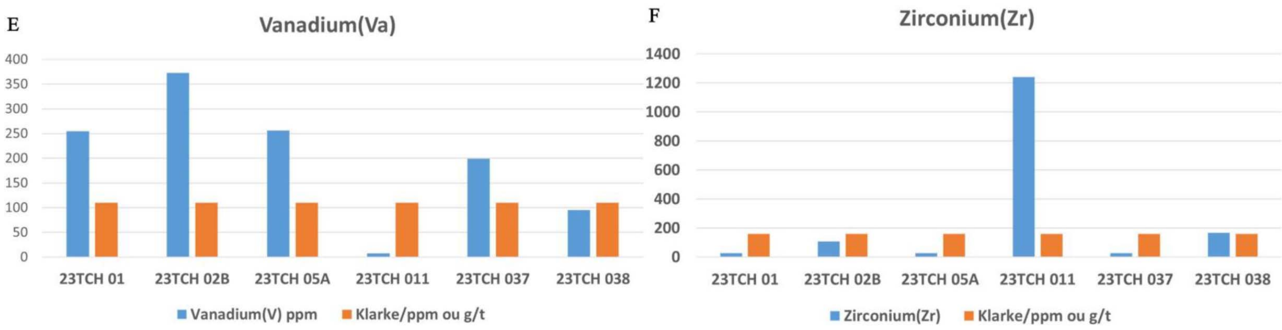

Figure 18. Histogram of sample analysis results showing chromium, nickel, vanadium, copper, cobalt and zirconium abnormalities compared to the Clarke value of each element.

4. Discussion

In this section we will try to discuss the different study results in order to characterize the geological formations of the northwest periphery of the central massif for the first time.

For a petrographical study we have identified meta-volcano-sedimentary rocks (Metabasalts, Metadacites, Metaconglomerates and marbles). The geological environment shows that the study area is located in the Paleo-basin of mega-Lake Chad, the accumulation of sediments of which would therefore be responsible for the formation of these sedimentary rocks, in this case the conglomerates and carbonates which have later undergone metamorphism.

The presence of newly formed minerals such as chlorites, calcite, and epidotes indicates alteration and metamorphism. These newly formed minerals are characteristic of low temperature, low pressure metamorphic conditions of green shale metamorphism.

The presence of feldspar in the rock samples is well matched with a positive Eu anomaly in the REE pattern [8]. These results are similar to the results of [5] [8] in the other region in Chad. Compared to the primitive magmas of the mantle, the very variable contents of MgO, Mg# (36.09 - 67) and transition elements (Sc, Cr, Co, Ni) of the metavolcanosedimentary rocks studied suggest that a certain degree of fractional crystallization occurred during the emplacement of mafic metavolcanic rocks [35]. The negative Nb anomaly, specific to subduction zone magmas, unrelated to that of Zr, suggests crustal contamination of a mantle basaltic magma in a context far from the influence of a subduction zone [36]. In the subduction area, fluid released from the upper part of the subducted lithosphere which is rich in LILE and poor in Nb is added to the mantle wedge [37]. Positive anomaly of Rb may have happened due to contamination of magma with crustal material (due to the high concentration of these elements in the continental crust). Meanwhile, negative anomalies of Ti element in lava can be formed on one hand to participate in the partial melting of lithospheric mantle linked to metasomatization and on the other hand crustal contamination resulting from digestion is attributed to zinocryst [38]. This Nb signature is due to an oceanic-oceanic subduction magmatic residue or a contamination from a MORB-like source.

The TAS [21], SiO_2 Vs K_2O [19] and Alk-FeO-MgO diagrams distinguished the calco-alkaline series rocks with high potassium characters on the one hand and the rocks belonging to the tholeitic series on the other. A dorsal cord is the site of frequent magmatism. Dorsal volcanism is generally basaltic, with tholeitic geochemistry. The fusion of the peridotitic material that takes place at the ridge is the origin of the material constituting the oceanic lithosphere [39].

Normalization of multielement to MORBs indicates losses of Ba, Ti and Cs which can be caused by the fractionation of plagioclase, apatite and ilmenite. The Ba anomaly is also controlled by the presence of K-feldspar and mica. The observed Ti anomalies are due to the fractionation of magnetite indicating a subduction environment (or remelting of a source from a subduction environment)

The characteristic of the calco-alkaline rocks described above corroborates the results of studies carried out in the Mayo-Kebbi zone showing a geodynamic environment of transition between subduction and collision [6] [11]. A tholeitic basalt has as its source the “oceanic” upper mantle, often depleted at the base, a larger partial fusion (10 to 25%) and little evolution after the formation of the magma. Calc-alkali basalt is also influenced by its source, close to a subduction zone, bringing alkalis and water which can promote the incorporation of CaO in the liquid. The rocks studied geochemically had intermediate to hypersilicic silica contents. Correlations observed between major elements with silica would show a fractionation of plagioclases during magmatic differentiation processes as shown in **Figure 15**.

The rare earth spectra of LREE enrichment relative to HREE are also similar to the work of [40] on volcanic rocks of El Aouana, NE Algerian. Negative correlations between major elements and silica in the Harker diagram show a significant fractionation of plagioclases. The diagram of [34] shows that the samples are MORBs of oceanic and continental arcs, which is consistent with the studies conducted by [8] in the Mayo-Kebbi region. These rocks have loss on ignition (LOI) values ranging from 2.26 to 11.65 wt%. % (**Table 1**), suggesting the contribution of secondary hydrated and carbonate phases. The few positive anomalies in Cr, Ni, Cu, Co, V; Zr reported are consistent with the results of geochemical studies conducted by [3] in the Batha area. From the metallogeny study, some samples have a higher chemical element content than Clarke’s value.

The Chaga geological formations in the Batha region which have been the subject of petrographic and geochemical studies, with obtained results and the work carried out by [6] [8] in the Mayo-Kebbi region show similarities in these facies which would probably be the extension to the South country.

5. Conclusions

The study of petrology, the geochemistry of geological formations southeast of Fitri Lake with metallogenic involvement, has allowed us to better understand the petrography of the Chaga area defined by volcano-meta-sedimentary formations specifically metabasalt, metadacite, marbles, meta conglomerates and quartz veins.

The geochemical analysis shows intermediate to hypersiliceous silica contents. Correlations observed between major elements with silica showed fractionation of plagioclases during magmatic differentiation processes. The Enrichment from LREE and HREE was observed in all samples. Enrichment of LREE elements is higher than HREE and the negative gradient of the graph indicates the higher amount of LREE than HREE which conforms with the overall pattern of spider diagrams in subduction zones.

These basaltic rocks are MORBs of oceanic arcs enriched to meta-dacite of continental arcs.

The deposit indices represented by some metals in the analyzed rocks show positive anomalies; these metals are potentially exploitable, subject to further studies to evaluate their tonnage to really prove the reserve.

Normalization of multielement to MORBs indicates losses of Ba, Ti and Cs which can be caused by the fractionation of plagioclase, apatite and ilmenite. The Ba anomaly is also controlled by the presence of K-feldspar and mica. The observed Ti anomalies are due to the fractionation of magnetite. Also, the presence of negative anomaly in P, Nb, Ta and Ti elements could indicate the formation of rocks in a subduction environment (or remelting of a source from a subduction environment)

Acknowledge

The authors are grateful to GMIA Minearls for supporting the field and laboratory financial and to the anonymous reviewers.

Conflicts of Interest

The authors declare no conflicts of interest regarding the publication of this paper.

References

[1] Schneider, J.L. (2001) Géologie, archéologie, hydrogéologie de la République du Tchad, tome 1 et 2, carte de valorisation des ressources en eau souterraines. UE-STABEX.

[2] Pias, J. (1970) La végétation du Tchad. Ses rapports avec les sols. Variations paléo-botaniques au Quaternaire. Travaux et Documents de l'ORSTOM N° 6, 49 p.

[3] Pierre, L. (1970) Contribution géophysique à la connaissance géologique du bassin du lac Tchad. ORSTOM, 312 p.

[4] Barbarin, B.D. (1996) Genesis of the Two Main Types of Peraluminous Granitoids. *Geology*, **24**, 295-298.

[5] Abba kaka, A. and Petit, Ch. (1993) Projet CHD/91/007 Renforcement de la DRGM. Géologie et géochimie du secteur de lélé-dolko.

[6] Doumnang, J.C. (2006) Géologie des formations Néoprotérozoïque du Mayo-Kebbi (Sud-ouest du Tchad): Apports de la pétrologie et de la géochimie, implications sur la Géodynamique au Panafricain. Master's Thesis, Université d'Orléans.

[7] Penaye, J., Kröner, A., Toteu, S.F., Van Schmus, W.R. and Doumnang, J. (2006) Evo-

lution of the Mayo Kebbi Region as Revealed by Zircon Dating: An Early (ca. 740ma) Pan-African Magmatic Arc in Southwestern Chad. *Journal of African Earth Sciences*, **44**, 530-542. https://doi.org/10.1016/j.jafrearsci.2005.11.018

[8] Tekoum, L., Doumnang Mbaigane, J.C., Kadjangaba, E., Qian, Y., Guang, D.W. and Sun, F.Y. (2023) Petrology, Geochemistry and Tectonic Environment of Igneous Complex in the Neoproterozoic Mayo Kebbi Basin, Chad. *International Journal of Current Research*, **15**, 23253-23260.

[9] INSEED (2009) Recensement général de la population et de l'habitation (RGPH). Institut National de la Statistique et de la Démographie, Bureau de la statistique et de la démographie, N'Djamena, TCHAD.

[10] Bessoles, B. and Trompette, R. (1980) Géologie de l'Afrique. La chaîne panafricaine "zone mobile d'Afrique centrale", (partie sud) et zone soudanaise. *Mémoire BRGM, Orléans*, **92**, 394.

[11] Pouclet, A., Vidal, M., Doumnang, J., Vicat, J. and Tchameni, R. (2006) Neoproterozoic Crustal Evolution in Southern Chad: Pan-African Ocean Basin Closing, Arc Accretion and Late- to Post-Orogenic Granitic Intrusion. *Journal of African Earth Sciences*, **44**, 543-560. https://doi.org/10.1016/j.jafrearsci.2005.11.019

[12] Pouclet, A. and Durand, A. (1983) Structures cassantes cénozoïques d'après les phénomènes volcaniques et néotectoniques au nord-ouest du lac Tchad (Niger oriental). *Annales de la Société Géologique du Nord*, No. 103-104, 143-153.

[13] Vincent, P.M. (1952) Rapport de Mission géologique Du Borkou Ennedi Tibesti. B.R.G.M.

[14] Vincent, P.M. (1963) Les volcans tertiaires et quaternaires du Tibesti occidental et central (Sahara du Tchad). Mémoire du BRGM 23, 307 p.

[15] Durand, A. (1993) Enregistrement sédimentaire de la dynamique climatique au Quaternaire supérieur dans le Sahel central (Niger et Tchad). Master's Thesis, Université de Bourgogne.

[16] Kusnir, I. and Moutaye, H.A. (1997) Ressources minérales du Tchad: Une revue. *Journal of African Earth Sciences*, **24**, 549-562. https://doi.org/10.1016/s0899-5362(97)00080-8

[17] Ramadan (2010) Géologie régionale du Batha (Rapport).

[18] Fitches, W.R., Ajibade, A.C., Egbuniwe, I.G., Holt, R.W. and Wright, J.B. (1985) Late Proterozoic Schist Belts and Plutonism in NW Nigeria. *Journal of the Geological Society*, **142**, 319-337. https://doi.org/10.1144/gsjgs.142.2.0319

[19] Wright, J.B., Hastings, D.A., Jones, W.B. and Williams, H.R. (1985) Geology and Mineral Resources of West Africa. Springer, 187 p.

[20] Aubrey and Mvokwe, N. (2008) Rapport annuel de la société GMIA Minerals.

[21] Peccerillo, A. and Taylor, S.R. (1976) Geochemistry of Eocene Calc-Alkaline Volcanic Rocks from the Kastamonu Area, Northern Turkey. *Contributions to Mineralogy and Petrology*, **58**, 63-81. https://doi.org/10.1007/bf00384745

[22] Le Maitre, R.W., Bateman, P., Dudek, A.G., *et al.* (1989) Download scientific diagram/Diagramme SiO_2 vs $Na_2O + K_2O$ appliqué aux roches magmatiques du Group de Ouarzazate (NP3sW).

[23] Irvine, T.N. and Baragar, W.R.A. (1971) A Guide to the Chemical Classification of the Common Volcanic Rocks. *Canadian Journal of Earth Sciences*, **8**, 523-548. https://doi.org/10.1139/e71-055

[24] Bas, M.J.L., Maitre, R.W.L., Streckeisen, A. and Zanettin, B. (1986) A Chemical Clas-

sification of Volcanic Rocks Based on the Total Alkali-Silica Diagram. *Journal of Petrology*, **27**, 745-750. https://doi.org/10.1093/petrology/27.3.745

[25] Schilling, J.G., Zajac, M., Evans, R., Johnston, T., White, W., Devine, J.D., *et al.* (1983) Petrologic and Geochemical Variations along the Mid-Atlantic Ridge from 29 Degrees N to 73 Degrees N. *American Journal of Science*, **283**, 510-586. https://doi.org/10.2475/ajs.283.6.510

[26] Sun, S. and McDonough, W.F. (1989) Chemical and Isotopic Systematics of Oceanic Basalts: Implications for Mantle Composition and Processes. *Geological Society, London, Special Publications*, **42**, 313-345. https://doi.org/10.1144/gsl.sp.1989.042.01.19

[27] MacLean, W.H. and Kranidiotis, P. (1987) Immobile Elements as Monitors of Mass Transfer in Hydrothermal Alteration; Phelps Dodge Massive Sulfide Deposit, Matagami, Quebec. *Economic Geology*, **82**, 951-962. https://doi.org/10.2113/gsecongeo.82.4.951

[28] Barrett, T.J., Cattalani, S. and MacLean, W.H. (1993) Volcanic Lithogeochemistry and Alteration at the Delbridge Massive Sulfide Deposit, Noranda, Quebec. *Journal of Geochemical Exploration*, **48**, 135-173. https://doi.org/10.1016/0375-6742(93)90003-5

[29] Rudnick, R.L., McLennan, S.M. and Taylor, S.R. (1985) Large Ion Lithophile Elements in Rocks from High-Pressure Granulite Facies Terrains. *Geochimica et Cosmochimica Acta*, **49**, 1645-1655. https://doi.org/10.1016/0016-7037(85)90268-6

[30] Winter, J.D. (2014) Principles of Igneous and Metamorphic Petrology: Pearson New International Edition (2e). Pearson Education, 738 p.

[31] Al-Fugha, H. and Bany Yaseen, I.A.A. (2019) Petrography, Geochemistry and Petrogensis of Pleistocene Basaltic Flow from Northwest Atarous Area, Central Jordan. *International Journal of Geosciences*, **10**, 613-631. https://doi.org/10.4236/ijg.2019.106035

[32] Brian, M. and Carleton, B.M. (1982) Principles of Geochemistry. 4th Edition, John Wiley & Sons, 350 p.

[33] Thompson, R.N. (1982) Magmatism of the British Tertiary Volcanic Province. *Scottish Journal of Geology*, **18**, 49-107. https://doi.org/10.1144/sjg18010049

[34] Pearce, J.A. and Peate, D.W. (1995) Tectonic Implications of the Composition of Volcanic ARC Magmas. *Annual Review of Earth and Planetary Sciences*, **23**, 251-285. https://doi.org/10.1146/annurev.ea.23.050195.001343

[35] Frey, F.A., Green, D.H. and Roy, S.D. (1978) Integrated Models of Basalt Petrogenesis: A Study of Quartz Tholeiites to Olivine Melilitites from South Eastern Australia Utilizing Geochemical and Experimental Petrological Data. *Journal of Petrology*, **19**, 463-513. https://doi.org/10.1093/petrology/19.3.463

[36] Nlomngan, J.P.S., Penaye, J., Tchameni, R., Owona, S., Ibohn, A.P.M., Nsifa, E.N., *et al.* (2019) Geochemical Characterization of Boula Ibi Granitoids and Implications in Geodynamic Evolution. *Journal of Geography and Geology*, **11**, 13-28. https://doi.org/10.5539/jgg.v11n4p13

[37] Borg, G. and Shackleton, R.M. (1997) The Tanzania and NE Zaire Cratons. In: de Wit, M.J. and Ashwal, L.D., Eds., *Greenstone Belts*, Clarendon Press, 608-619.

[38] McDonough, W.F. and Sun, S. (1995) The Composition of the Earth. *Chemical Geology*, **120**, 223-253. https://doi.org/10.1016/0009-2541(94)00140-4

[39] Sauter, D., Cannat, M., Rouméjon, S., Andreani, M., Birot, D., Bronner, A., *et al.* (2013) Continuous Exhumation of Mantle-Derived Rocks at the Southwest Indian Ridge for 11 Million Years. *Nature Geoscience*, **6**, 314-320.

https://doi.org/10.1038/ngeo1771

[40] Hamlaoui, H., Laouar, R., Bouhlel, S. and Boyce, A.J. (2020) Caractéristiques pétrologiques et géochimiques des roches magmatiques d'El Aouana, NE algérien. *Estudios Geológicos*, **76**, e124. https://doi.org/10.3989/egeol.43391.510

International Journal of Geosciences, 2026, 17(1), 38-48
https://www.scirp.org/journal/ijg
ISSN Online: 2156-8367
ISSN Print: 2156-8359

Performance of Boreholes Capturing the Aquifers Systems in the Crystalline Peneplain of Benin

Ringo Fernand Avahounlin[1*], Jean-Eudes Okoundé[2], Lucie Koudérin[2], Abdoukarim Alassane[2], Brunelle Icoutchika[2], Fabrice Lawson[2], Nelly Kélomé[2]

[1]National University of Science, Technology, Engineering and Mathematics, Abomey, Benin
[2]University of Abomey-Calavi, Calavi, Benin
Email: *d2ringofernand@gmail.com

How to cite this paper: Avahounlin Ringo, F., Okoundé, J.E., Koudérin, L., Alassane, A., Icoutchika, B., Lawson, F. and Kélomé, N. (2026) Performance of Boreholes Capturing the Aquifers Systems in the Crystalline Peneplain of Benin. *International Journal of Geosciences*, **17**, 38-48.
https://doi.org/10.4236/ijg.2026.171003

Received: October 16, 2023
Accepted: January 20, 2026
Published: January 23, 2026

Abstract

The water supply in the regions of the crystalline peneplain of Benin is ensured by the mobilization of groundwater. The objective of this study is to assess the productivity of fractured and/or fissured aquifers in the communes of Nikki, N'Dali and Pèrèrè located in northern Benin. The methodological approach is based on the comparative analysis of the physical and hydrodynamic parameters of the catchment structures associated with the interpretation of pumping tests of long and short durations combined. It appears from this study that the most productive depths are between 21.6 and 76 m. Some of the boreholes studied (32.37%) have a low flow rate. The transmissivity values vary from $3.06.10^{-5}$ to $6.95.10^{-4}$ m^2/s with an average of $2.38.10^{-4}$ m^2/s; the specific flow varies from 0.25 to 2.20 m^2/h with an average of 0.82 m^3/h. The classification of the distribution of flows and transmissivities established by the Lasm criterion (2000) showed that most of the boreholes have high transmissivities, which are witnesses of productive boreholes in the study area.

Keywords

Fractured and/or Fissured Aquifers, Productivity, Borehole Depth, Hydrodynamics, Transmissivity

1. Introduction

Water, also called "blue gold", is a vital resource for living beings in general and for man in particular. All the water on earth represents a volume of approximately 1.4 billion km^3, available in the form of liquid, solid, or gas [1]. However, most of the water (97%) is contained in the oceans, and is salty, which makes it unusable by humans. Fresh water represents only 3% of the water on earth, half of this water represents fresh water available for human use, *i.e.* only 0.3% of the volume of water in the planet, or 4 million km^3. This water is accessible in various natural resources such as rivers, shallow aquifers, or lakes [1]. Indeed, in Africa, the drinking water supply of the rural population comes from groundwater. The waters contained in the bedrock in particular are exploited by thousands of boreholes and wells. In reality, the territory of Benin is 80% made up of basement and there is a high rate of borehole failure in this area [2]. The communes of Nikki, Pèrèrè and N'Dali are no exception to this situation. Despite the goodwill of leaders to satisfy the demand for water, these numerous cases of failure slow down the achievement of their objectives and affect the economy. In order to increase the success rate of drilling in these environments, it is important to know the most productive zones of the aquifers exploited in the complex. Indeed, aquifers are generally characterized by their ability to store water and ensure its mobility. Hydrodynamic parameters are indices that define the ability of the aquifer to recover and deliver water. They are essential to know the aquifer and its volumes of water that can be exploited by a well or borehole [3]. In view of the resolution of this problem, the present work whose theme is: "the productivity and hydrodynamics of aquifer systems in the crystalline peneplain of Benin" aims to study the hydrodynamic parameters of these aquifers in relation to productivity.

2. Materials and Methods

2.1. Presentation of the Study Area

Covering an area of 9069 Km^2, the study area of our work is in the department of Borgou and is located east of the Kandi fault between latitudes 9˚25'N and 10˚15'N and longitudes 2˚00'E and 3˚35'E. The climate is of the Sudano-Guinean type characterized by a rainy season which extends from April to October and a dry season from November to March. However, despite the quantity of available water that flows and infiltrates, the supply of drinking water remains an important issue due to the geological nature of the subsoil.

Geologically, the study area is located on the crystalline peneplain. To the east, it has a dominant facies of migmatites and biotite granitoids. It brings together the Agramarou migmatite formations and the Pan-African intrusions. To the west, the geological domain is represented by migmatitic gneissic formations and also migmatites of the axial zone of Kandi. Faults are observed in places from North-East to West as well as formations of the Ouémé furrow and intrusive granite in the South-East.

2.2. Data

The data used in this study concerns technical drilling data (localities, geographical coordinates, end-of-drilling flow rate, total depth drilled), and pumping test results (long and short duration), made available to us by the ESSOR engineering office and the General Direction of Water. More than 207 technical drilling sheets, made in the crystalline peneplain of Benin, were used, including 15 pumping test sheets. The boreholes used during the study are presented on the map in "**Figure 1**". To produce the graphs and maps presented in the document, we used the hydrogeological map of Benin at the scale of 1/500000th and geological sheets Parakou-Djougou-Nikki, that of Dunkassa then that of Bembèrèkè on a scale of 1/200000th.

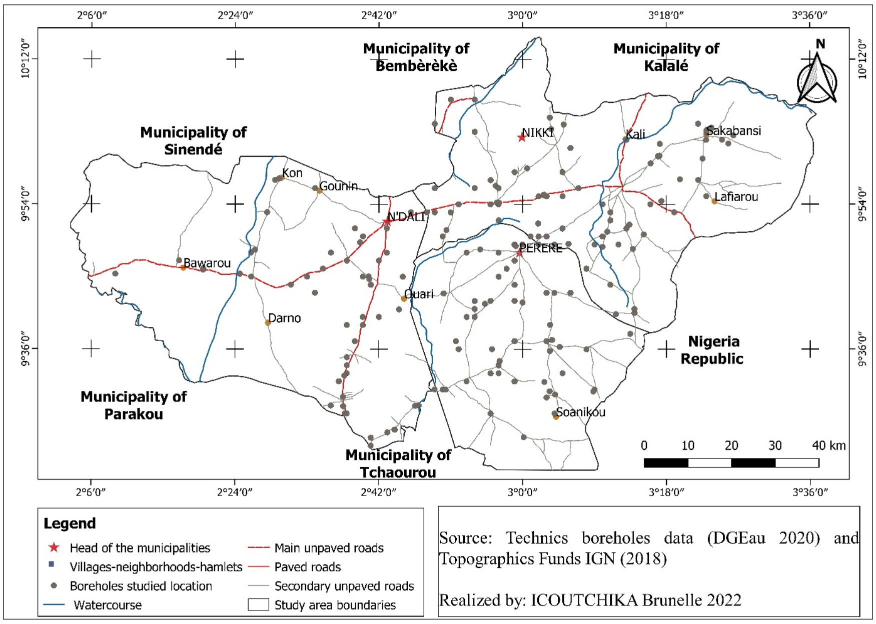

Figure 1. Projection map of the coordinates of the boreholes studied.

2.3. Methods

- Productivity evaluation

Productivity is the ability of an aquifer to provide a minimum usable flow through the channel of a catchment structure [4]. In order to evaluate the productivity of the basement aquifers in our study area, a comparative analysis was carried out between the flow rates of the boreholes and the hydrodynamic parameters (transmissivities and specific flow). The distribution of these flows and transmissivities has been established by various authors such as [5]-[7].

The classification is as follows (**Table 1**).

Table 1. Classification of flows and transmissivity [5].

Flow (m^3/h)		Transmissivity (m^2/s)	
Values	**Classification**	**Values**	**Classification**
0 - 1	Very low flow	$<10^{-5}$	Low class
1 - 2.5	Low flow	$10^{-5} < T < 10^{-4}$	Middle class
2.5 - 5	Average flow	$T > 10^{-4}$	High class
>5	High flow	-	-

- Hydrodynamic approach to aquifers

Determination of transmissivity T

This study was carried out using pumping test data obtained from the various drilling data sheets. These data were used to determine the hydrodynamic parameters, namely transmissivity (T) and specific flow (Qs). By the rise method, the transmissivity value is much more reliable because the pressure losses are much more negligible. Thus, based on long-term tests, to assess transmissivity, we therefore used the Theis rise method as recommended by (Lasm, 2000) [5] in [8] according to the formula:

$$\boldsymbol{T} = \frac{2.3 * \boldsymbol{Q}}{4\boldsymbol{\pi} * \Delta \boldsymbol{s}'} \tag{1}$$

With:

T: transmissivity in m^2/s; Q: the constant pumping rate in m^3/h and Δs′: the variation of the residual drawdown s' [9].

In fact, Theis' formula for transmissivity is based on the logarithmic relationship. This requires conversion between natural and decimal logarithmic units. This is why the factor 2.3 is used in the formula.

2.3: this factor converts the natural logarithm (e) into a decimal logarithm (10), as in this formula the logarithm is calculated in base 10. This factor is used to adjust the logarithmic scale and make the equation consistent. Consequently, the 2.3 * Q term in this formula is a factor that adjusts the flow rate to match the model's logarithmic scale.

The graph in "**Figure 2**" obtained from the long-term pumping test carried out on the Donkpraoui borehole in the municipality of Nikki highlights Δs′.

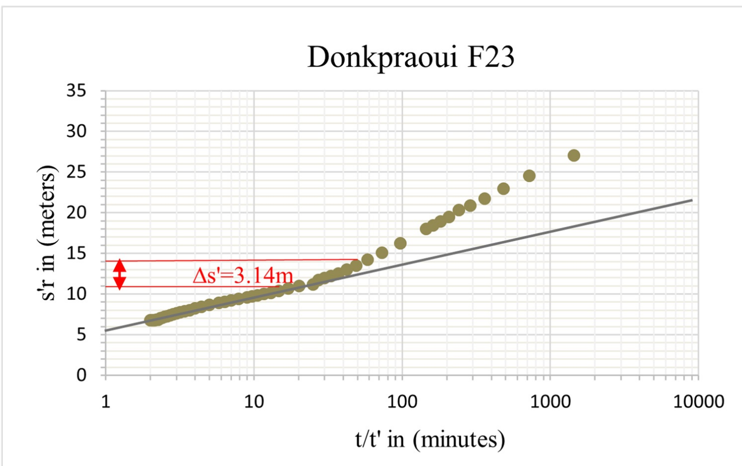

Figure 2. Determination of the slope of Jacob on the site of Donkpraoui F23.

➢**Determination of the specific flow Qs**

Data from pumping tests in stages at constant flow (short duration) allowed the calculation of the specific flow (Qs). It gives indications on the characteristics of the boreholes and on the connectivity between the fracture networks ([5] in [10]).

It was calculated at the end of the first level at all the boreholes using this formula:

$$Qs = \frac{Q}{s}$$

With: Qs: specific flow in (m2/h); Q: pumping rate in (m^3/h) and s: drawdown in (m).

3. Results and Discussions

3.1. Borehole Productivity Analysis

From the results obtained from the distribution histogram of the borehole flow classes in the study area; 25.12% of boreholes have very low flow rates, 32.37% with low flow rates, 18.35% with medium flow rates and 26.57% with high flow rates. Thus, in our study area productivity is low. However, 77.29% of boreholes have flow rates greater than or equal to 1 m^3/h. According to Soro (1987) quoted by [7] in [10] these flows are acceptable for Village Hydraulic projects for the Drinking Water Supply of populations in rural areas. The flow distribution histogram of the aquifer system in the crystalline peneplain of Benin is given in "**Figure 3**" below.

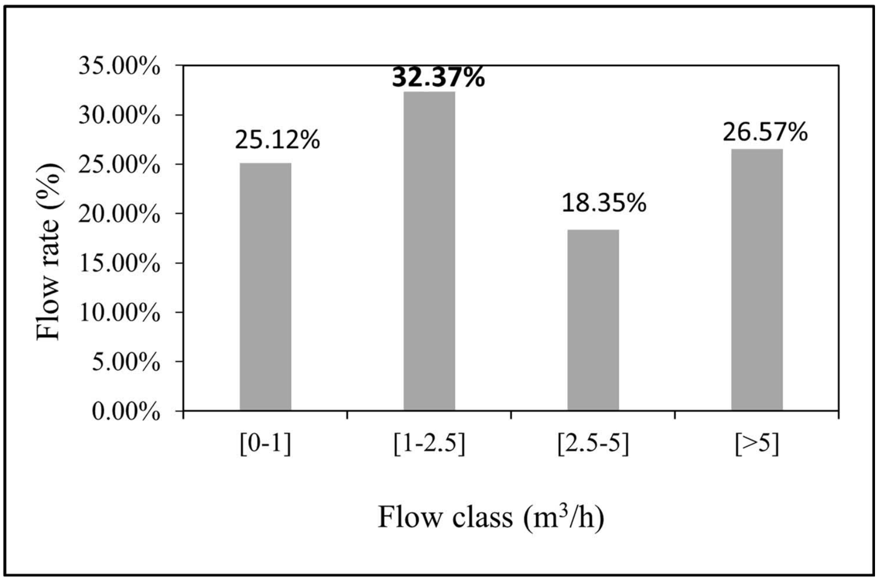

Figure 3. Histogram of flow classes.

- **Productivity and physical parameters of boreholes (total depth)**

The relationship between drilled depth and instantaneous flow is represented by the graph in "**Figure 4**". Analysis of the graph indicates that the majority of significant flows (> 5 m^3/h) are between 21.6 and 76m deep . Also the majority of flows are in the range of 21 to 80 m. However, flows greater than 15 m^3/h are between 36 and 75.5 m. So we can say that the productive slice is 21.6 to 76 m. In the same basement context, [10] suggest depths between 30 and 75 m as optimal depths. However, there are some flows greater than 5 m^3/h between 86 and 104 m.

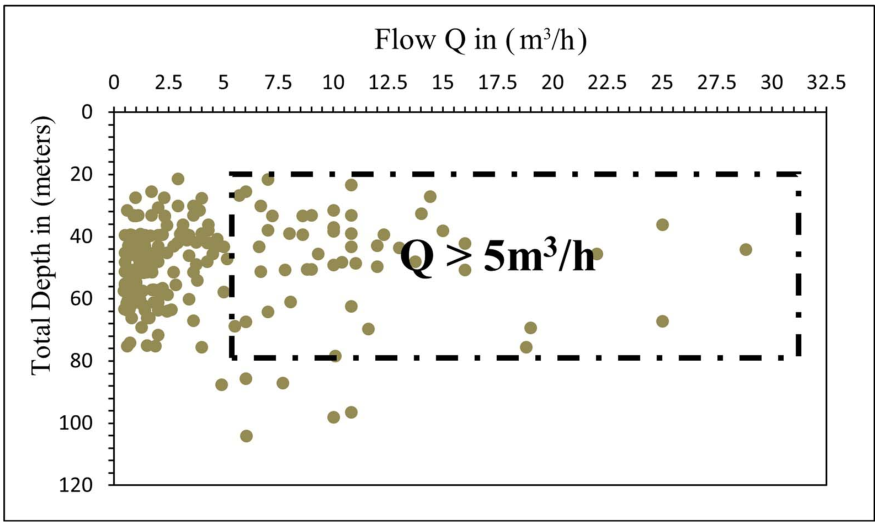

Figure 4. Relationship between discharges and total depth.

3.2. Determination of Hydrodynamic Parameters and Spatialization

The interpretation of long-duration pumping tests using the Theis rise method (1935) made it possible to determine the values of transmissivity T and of the specific flow rate Qs (**Table 2**).

Table 2. Calculated transmissivity values from long-term tests.

Town	Locality	Transmissivity (m^2/s)	Flow Q (m^3/h)	Δs' (m)
N'Dali	Boko	1.20×10^{-4}	20.03	2.16
N'Dali	Darnon	1.05×10^{-4}	20.03	4.37
N'Dali	Sonnoumon	2.47×10^{-4}	20.03	4.16
Nikki	Donkpraouin F'1	1.27×10^{-4}	20.03	4.75
Nikki	Donkpraouin F23	3.24×10^{-4}	20.03	3.14
Nikki	Sakabansi F'22	8.59×10^{-5}	20.03	3.11
Nikki	Sakabansi F'1	3.06×10^{-5}	20.03	8.62
Pèrèrè	Boro-Centre	6.95×10^{-4}	20.03	0.94
Pèrèrè	Gninsy-Centre	1.43×10^{-4}	20.03	1.85
Pèrèrè	Gninsy-Peulh	2.08×10^{-4}	20.03	1.22
Pèrèrè	Sontou	5.37×10^{-4}	20.03	0.65

The previous table relating to the calculated values of transmissivity of the various structures studied shows that the values of transmissivity are of the order of 10^{-4} m^2/s except for the boreholes of the localities of Sakabansi (F1 & F22) which are of the order of 10^{-5} with a general average of $2.38.10^{-4}$ for all the works. Thus, the structures within the scope of the study have transmissivities ranging from medium to high.

The values of the specific flow calculated for the crystalline peneplain aquifer system, obtained from the 1st stage of the short-term pumping test data, are presented as in the following "Table 3":

Table 3. Calculated specific flow values.

Town	Locality	Drawdown (m)	Flow Q (m^3/h)	**Specific flow Qs (m^2/h)**
NIKKI	Sakabansi F1	8.09	2	0.247218789
NIKKI	Domplawi F1	7.42	9.32	1.25606469
NIKKI	Sakabansi F22	4.69	1.6	0.341151386
NIKKI	Domplawi F23	3.92	5.39	1.375
PERERE	Boro-Centre (SE3-F2)	1.17	2.57	2.196581197
PERERE	Gninsy-Centre	7.92	2.53	0.319444444
PERERE	Guinangourou	7.23	2.5	0.345781466
PERERE	Boro (SE1-F1)	1.88	2	1.063829787
PERERE	Gninsy-Peulh	2.66	2.5	0.939849624
PERERE	Sontou (SE3)	1.76	1.47	0.835227273
PERERE	Souanworoussou	16.07	6.26	0.389545737
N'Dali	Boko	3.78	1.9	0.502645503
N'Dali	Darnon	11.88	5.15	0.433501684
N'Dali	Sonnoumon	3.31	5.4	1.63141994
N'Dali	Ouénou-Peulh	6.65	3.07	0.461654135

The values obtained vary from 0.25 m^2/h to 2.20 m^2/h with an average of 0.82 m^2/h. The maximum value is obtained in the locality of Boro-Centre with a drawdown of 1.17. The minimum value is found in the locality of Sakabansi with a drawdown of 8.09. Consequently, the specific flows in the study area are mostly very low (66.66%) with the exception of structures in the localities of Sonnoumon, Domplawi and Boro which are low (33.33%).

Spatialization of the distribution of hydrodynamic parameter values T and Qs

The spatial distribution of the values of transmissivities in m^2/s and specific flow rates in m^2/h shows that low transmissivities and specific flow rates are more concentrated in the South-West and North-East of the crystalline peneplain of Benin "Figure 5". At the level of the highest values, they are observed in the direction (South-East; North-West) of the study area.

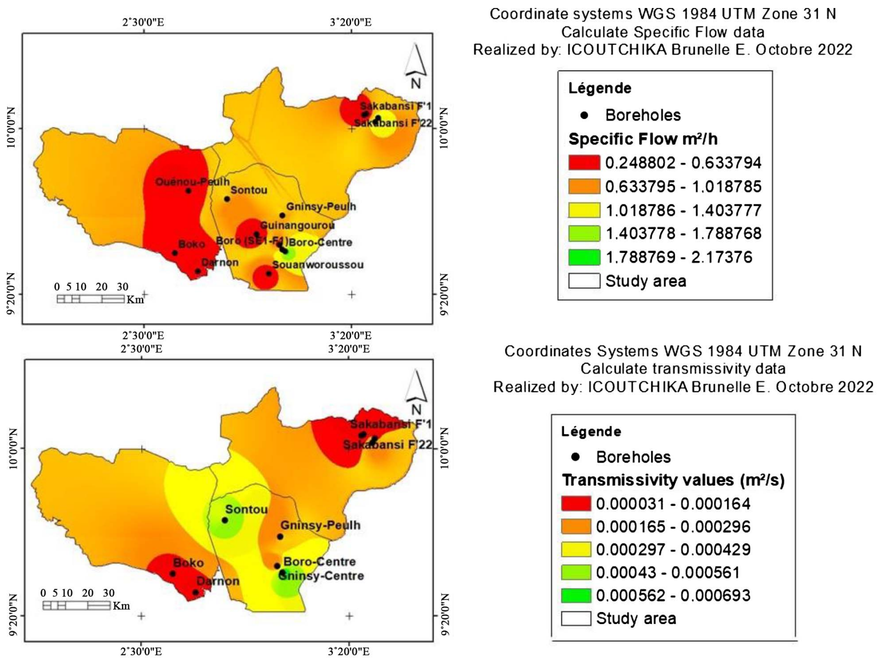

Figure 5. Spatial distribution map of transmissivity and flow values specific to the study area.

3.3. Productivity and Hydrodynamic Parameters

Statistical analysis of the hydrodynamic parameters of the various structures studied shows that the transmissivity values vary from $3.06.10^{-5}$ to $6.95.10^{-4}$ m²/s with a standard deviation of $2.06.10^{-4}$ m²/s, an average of $2.38.10^{-4}$ and a coefficient of variation of 0.87. The graph in Figure 6 illustrates the transmissivity class histogram. Of this graph, 18.18% are included in the class of medium transmissivities and 81.82% in the class of strong transmissivities. Thus we note that the structures studied have strong transmissivities. We can deduce that the basement aquifers captured in our study area have an average transmissive function.

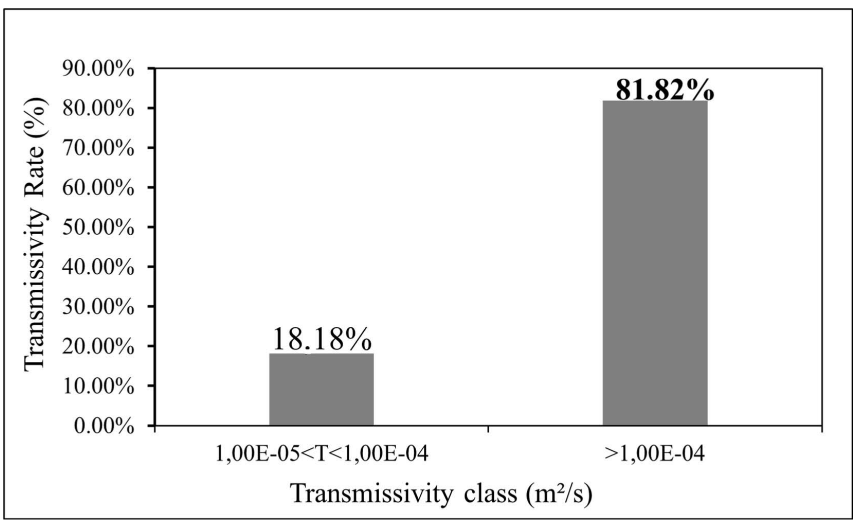

Figure 6. Histogram of the class of transmissivities. (Data used 2020)

Statistical analysis of the specific flow of the various structures studied shows that the values vary from 0.25 to 2.20 m^2/h with a standard deviation of 0.58 m^2/h, an average of 0.82 m^2/h and a coefficient of variation of 0.71. The distribution of the specific drilling flows according to the depth of the structures shows that the specific flows are found in the range of intervals from 50 to 90 m. However, most specific flow rates above 1 m^2/h are between 50 and 70 m. A drop in specific flows is observed after 70 m. This slice joins the one cleared at the level of the productive drilling depth (Figure 7).

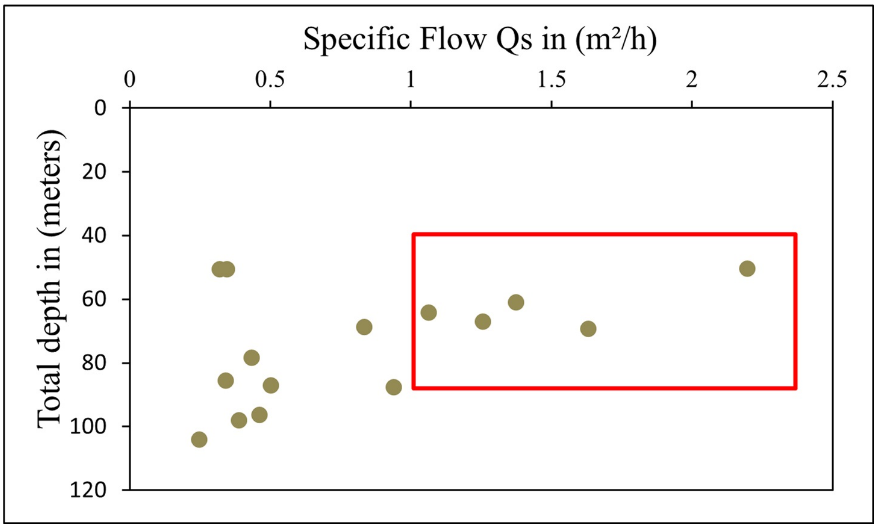

Figure 7. Relationship between specific flow rates and total borehole depth.

4. Discussion

In the Nikki-Pèrèrè-N'Dali complex, the total depth of the boreholes varies from 21.3 m to 104.01 m with an average of 49.47 m. The productive depth range is between 21.6 and 76 m. These values are close to those found by [10] in Côte d'Ivoire in the Katiola region where the values for the most productive depths are between 30 and 75 m. However, flow rates greater than 5 m^3/h are observed between 86 and 104 m; this could certainly mean that not having obtained the expected flow, the drilling was continued. The end-of-bore flow rate (instantaneous flow rate) of the boreholes varies from 0.45 m^3/h to 28.8 m^3/h with an average of 4.30 m^3/h. The histogram of the flow distribution of the boreholes of the Nikki-Pèrèrè-N'Dali complex indicates that it is the class of low flows that dominates in the study area, *i.e.*, 32.37%. We also note that 77.29% of these boreholes have flow rates greater than or equal to 1 m^3/h; acceptable flow rates for Village Water Supply projects to supply drinking water to rural populations (Soro 1987) in [10].

The transmissivity values obtained by the Theis rise method are between $3.06.10^{-5}$ and $6.95.10^{-4}$ m^2/s with an average of $2.38.10^{-4}$ m^2/s. According to the classification of flows and transmissivities according to [5] the values of transmissivities are divided into three classes. The class of low transmissivities ($T < 10^{-5}$ m^2/s); the medium transmissivity class ($10^{-5} < T < 10^{-4}$ m^2/s) and the high transmissivity class (T>10−4 m2/s) of the latter, 81.82% of the structures studied in the area of study have strong transmissivities, a little more than the percentage obtained by [11] in the commune of Savalou (76.47%). The specific flow values of the boreholes studied vary from 0.25 m2/h to 2.20 m2/h with an average of 0.82 m2/h. These values indicate that the specific flow rate of the area is mostly low; this confirms the dominant class of low-end-of-drilling flow rates within the study framework. This is certainly due to the fact that during Village Hydraulic campaigns, the search for very productive fractures is not a priority.

5. Conclusion

This study shows that the crystalline peneplain found in the communes of Nikki-Pèrèrè-N'Dali in Benin is a geologically difficult hydro zone for water supply. Despite the high transmissivity values obtained in the area, productivity in the communes of Nikki, Pèrèrè and N'Dali is generally low. This can be seen in the flow rate values, which range from 0.45 to 28.8 m^3/h, with an average of 4.30 m^3/h. Although we are aware that we have only just provided an answer to the many problems that arise in the basement within our study area, we suggest that, in order to bring greater precision to our knowledge of these aquifers, a fracturation map of the area should be produced in order to identify the fracture networks making up the aquifer system and their inter-connectivity. This will enable us to confirm the conductive or non-conductive function of the aquifer systems.

Conflicts of Interest

The authors declare no conflicts of interest regarding the publication of this paper.

References

[1] L'Observatoire Régional pour l'Environnement (2016) Répartition de l'eau sur terre.

[2] Alle, C. (2019) Évaluation de l'implantation géophysique des forages d'eau en zone de socle en milieu tropical (Bénin, Afrique de l'Ouest): Apport de la tomographie de résistivité électrique pour la caractérisation de la cible hydrogéologique. Ph.D. Thesis, Université d'Abomey-Calavi.

[3] (2003) Françoise Gourmelon. La contribution des SIG à la connaissance et à la gestion de l'environnement littoral. Sciences de l'Homme et Société. Université de Bretagne occidentale-Brest. https://theses.hal.science/tel-00321106v1

[4] Gombert, P. (1997) Variabilité spatiale de la productivité de l'aquifère du socle sahélien en hydraulique rurale. *Hard Rock Hydrosystems*, **241**, 113-122.

[5] Lasm, T. (2000) Hydrogéologie des réservoirs fracturés de socle: Analyses statistique et géostatistique de la fracturation et des propriétés hydrauliques. Application à la région des montagnes de Côte d'Ivoire (domaine archéen). Ph.D. Thesis, Université de Poitiers, 274 p.

[6] Dibi, B., Inza, D., Goula, A., Savane, I. and Biémi, J. (2004) Analyse statistique des paramètres influençant la productivité des forages d'eau en milieu cristallin et cristallophyllien dans la région d'Aboisso (Sud-Est de la Cote d'Ivoire). *Sud Sciences & Ttechnologies*, No. 13, 22-31.

[7] Kouassi, K. (2012) Evaluation quantitative et qualitative des ressources en eau de la

région centre: Cas du département de Didiévi en Côte d'Ivoire. Institut National Polytechnique Félix Houphouet-Boigny de Yamoussoukro (Côte d'Ivoire) Memoire Online 2000 2019 mémoireonline.com.

[8] Ahoussi, K.E., Koffi, Y.B., Kouassi, A.M., Soro, G., Soro, N. and Biémi, J. (2013) Fonctionnement hydrodynamique des aquifères discontinus de la région d'Abidjan-Agbovillle (Sud de la Côte d'Ivoire). *International Journal of Geography and Geology*, **2**, 52-69. https://doi.org/10.18488/journal.10/2013.2.5/10.5.52.69

[9] Kotchoni Valerie, O. (2012) Evaluation des performances des forages d'exploitation du champ de captage de Ouèdo et des paramètres hydrodynamiques de l'aquifère capté: Intèrêt pour une mise en valeur durable des ressources en eau souterraines locales. Mémoire de Master, Université d'Abomey-Calavi, Faculté des Sciences et Techniques (FAST), 28-32.

[10] Gnamba, M.F., Solange, O.Y.M., Théophile, G., *et al.* (2014) Analyse de la productivité des aquifères de fissures du socle paléoprotérozoïque de la région de katiola. *European Scientific Journal*, **10**, 79-98.

[11] Sodjahin, A. (2019) Etude de la productivité des aquifères de socle dans la commune de Savalou. Mémoire de Licence, Université d'Abomey-Calavi, Institut National de l'Eau, Hydrologie et Gestion des Ressources en Eau, 40-45.

International Journal of Geosciences, 2026, 17(1), 49-65
https://www.scirp.org/journal/ijg
ISSN Online: 2156-8367
ISSN Print: 2156-8359

The Status of the Gravimetric Geoid across Nigeria

Kurotamuno Peace Jackson, Lawrence Hart

Department of Surveying and Geomatics, Rivers State University, Port Harcourt, Nigeria
Email: kurotamuno.jackson@ust.edu.ng

How to cite this paper: Jackson, K.P. and Hart, L. (2026) The Status of the Gravimetric Geoid across Nigeria. *International Journal of Geosciences*, **17**, 49-65.
https://doi.org/10.4236/ijg.2026.171004

Received: December 23, 2025
Accepted: January 26, 2026
Published: January 29, 2026

Abstract

Orthometric heights are obtained by Spirit leveling; however, this approach is not only slow but is also costly and time-consuming. Therefore, the uncertainties in the accuracy of geoid height models have hampered the use of GNSS heightening as an alternative method of determining Orthometric heights across Nigeria. This study was aimed at appraising the status of the geoid model in Nigeria based on gravity measurements, applying the remove-compute-restore (r-c-r) approach through the Fast Fourier Transform (FFT) tool. The GRAVSOFT tool was used in evaluating the residual height anomalies and terrain effects resulting from the residual terrain model (RTM). The residual height anomalies, (ζ_{res}) were computed by applying the modified Molodenskii Integral tampered 100% zero padding so as to overcome cyclic effects. The residual height anomalies were converted to geoid undulation by adding the ζ-to-N correction. The study revealed that, the difference between the height anomaly (ζ) and the geoid height (N) is about 24 cm and the geoid values across Nigeria range between 13.738 m and 26.052 m. There is a tilt of the geoid from the South-west to North-west part of the country. The gravimetric geoid is accurate to ±41 cm rmse when compared with the geometric geoid while the surface fitting revealed that the hybrid-geoid is accurate to ±3 cm rmse.

Keywords

Fast Fourier Transform, Gravimetric Geoid, Height Anomalies, Hybrid-Geoid, Residual Terrain Model

1. Introduction

The quest for an improved local geoid for Nigeria has been on for some time now. Geoid determination or modeling is one of the essential problems in geodesy. A key aim of physical geodesy is the determination of the geoid with accuracy at the centimeter (cm) level, matching the accuracy of Global Navigation Satellite System (GNSS) height determination. The combination of an accurate geoid model with GNSS coordinates plays a central part in achieving timely, high accuracy leveling results, mostly over long distances, unlike Spirit leveling, which is tedious, costly, and time-consuming. However, the up-to-date accuracy of global geoid modeling is a few decimeters to meters, which is not adequate for many scientific and engineering applications. Thus, there is a need to model the geoid locally.

The geoid heights, when compared to the ellipsoidal heights from GNSS, can result in orthometric heights accurate to those delivered by spiriting leveling. For practical purposes, most countries have established an officially fitted geoid model corresponding to the height system(s) in use. Such a national model can be used for height system unification, scientific purposes, and other regional tasks, but also as a national reference surface. One of the primary practical applications of geoid height (N) in surveying is to transform GNSS-derived ellipsoidal heights (h) to orthometric heights (H) as argued [1] using the simple algebraic relation as shown in Eq. 1:

$$H = h - N \tag{1}$$

However, there is no officially published geoid model in Nigeria for engineering and related applications. More so today, local modeling of the geoid, amongst other things, facilitates the connection between land datum and sea datum; this has been implemented in most developed countries with the terminologies such as Vdatum (Canada and US) and Vertical Offshore Reference Frame (VORF) in Great Britain, Ireland, and Northern Ireland [2]. It becomes very pertinent to emphasize the necessity for the determination of an acceptable geoid model for Nigeria, which will help and drive proper integration and effective use of the Global Navigation Satellite System (GNSS) over Nigeria for GNSS heightening. The geoid is evaluated using different methods such as geometric/leveling, astro-gravimetric, satellite, gravimetric, and a combination of any of the above methods. Each of these approaches has its peculiar strengths and weaknesses.

Thus, high-resolution regional/local models are still required for most practical purposes. There are many different methods proposed over the years for global, regional, and local geoid evaluation by gravimetric data, each with its own procedure, concepts, and philosophy. In addition, today all of these techniques integrate long-wavelength Global Geopotential Models (GGMs) with a combination of local terrestrial and airborne gravity data. However, they differ purely in the way they join these data sets.

There are different approaches to gravimetric geoid modeling such as Least Squares Collocation (LSC), Least Squares Modification of Stokes Integral with Additive Corrections, Remove-Compute-Restore (R-C-R) approach using Fast Fourier Transform (FFT) Technique, etc., each based on its philosophy, weaknesses, and strengths. In the gravimetric approach to geoid modeling, the geoid is modeled using the Stokes integral after gravity reduction as shown in Eq. 2 [3].

$$N = \frac{R}{4\pi\gamma_0}\iint_{\sigma} \Delta g S(\psi) \mathrm{d}\sigma \tag{2}$$

where: N: The Geoid height, γ_0: Normal gravity, Δg: Gravity anomaly, and $S(\psi)$: Stokes kernel. The Stokes integral has two conditions that must be satisfied for the results to be true. Firstly, as the solution to the geodetic boundary-value problem (BVP), the Stokes integral requires the gravity anomalies to represent the boundary values on the geoid. That is, it must be referred to the geoid.

Secondly, there must be no masses present outside the geoid, making sure that g on the geoid truly is the boundary surface, as the BVP's used in physical geodesy are the solution to Laplace's Equation, and $\Delta V \neq 0$ if masses exist above surface S as opined by [3]. The gravity on the geoid and the gravity on the reference ellipsoid must be well-defined, such that there are no masses present above the geoid, to satisfy the requirements of the boundary value problems. Since gravity cannot be measured on the geoid, gravity observed on or above the Earth's surface must be reduced to the geoid.

Even when gravity is measured at the geoid, all the mass on Earth above the geoid would have to be removed. This modifies the mass distribution of the Earth, making it difficult to define the actual geoid. The second condition of the Stokes integral; is overcome by applying the theory of Molodenskii. The terrain replaces the geoid as the boundary surface, and the result of the Stokes integral is the quasi-geoid instead of the geoid. While the quasi-geoid is approximately equivalent to the geoid in terms of shape, unlike the geoid, it has no physical meaning and is merely a mathematical surface of convenience [4]. In the remove-compute-restore (R-C-R) approach, as posited by [1], the long, medium, and short wavelength components are derived from global geopotential models, terrestrial gravity, and Digital Terrain Models (DTM). This approach adopts the procedure of computing the gravity anomalies and then the geoid model, taking into account the integration of the different wavelengths mentioned earlier.

The study is aimed at appraising the status of the geoid in Nigeria with the following objectives:

1) Compute the residual gravity anomaly (Δg_{RES}) from terrestrial gravity, including residual terrain models for the remove and restore effects,

2) Compute residual height anomalies from Molodenskii integral based on the FFT model and sum the resulting different effects to obtain height anomalies and also convert the height anomalies to classical geoid values so as to generate the regular geoid grid file based on FFT model,

3) Compare the gravimetric and geometric geoid and tailor the geoid file to the GNSS/leveling data using a seven-parameter model.

2. Data and Methods

2.1. Data Used for Research

The data used for this research are terrestrial gravity data, digital terrain model (DTM), and GNSS/leveling and were obtained from different sources. The terrestrial gravity dataset was obtained from Bureau Gravimetrique International [5] as shown in **Table 1**. These data were contributed by different organizations and individuals either for oil prospecting or for the development of a gravity geoid for the country, however, the data were domiciled at Bureau Gravimetrique International (BGI), and the fill-in gravity data were obtained from the International Centre for Global Earth Models [6]. The gravity field information received contains the absolute gravity value (g), free-air anomaly, bouguer anomaly and the height of the gravity stations. Statistically, more than ninety-five (95) percent of the gravity field information received contains this information.

Table 1. Statistics of gravity and anomalies data used for the research.

Types	Counts	Max. (mGal)	Min. (mGal)	Mean (mGal)	Std. Dev.	Remarks
Gravity	4,234	978203.44	977907.71	978057.46	36.16	BGI
Free-Air Anomaly	4,234	71.406	−70.960	−1.910	24.652	GRS80
Bouguer Anomaly	4,234	55.970	−85.260	−16.983	22.306	GRS80
Fill-in Dataset						
Gravity	8,167	978286.21	977692.60	978073.84	128.22	EGM08
Free-Air Anomaly	8,167	72.60	−70.96	3.59	21.11	GRS80
Bouguer Anomaly	8,167	19.80	−105.05	−44.00	22.00	GRS80

Therefore, it was easier to evaluate the inner consistency between the information in the data given such as the height, free-air anomaly and the Bouguer anomaly, and to identify which normal gravity formula has been used (*i.e.* GRS67 or GRS80). Absence of internal consistency between constituents of a data record is a clear indication of erroneous gravity data. As it is most often not clear which constituent of a data record is erroneous, the internally non-consistent records could not be repaired and were therefore simply eliminated from the dataset. Nearly, five percent of data points were removed from the dataset, and it was discovered that the GRS67 ellipsoid was used in the computation, which was subsequently converted to align with the global ellipsoid GRS80.

The digital terrain model (DTM) sourced from ALOS Global Digital Surface Model "ALOS World 3D-30 m (AW3D30)" as reported by [7]. The SELECT subroutine was used to re-sample the DTM by low-pass filtering employing a moving average to create the detailed, coarse and reference grids. The data sets used for this study are shown pictorially in **Figure 1**.

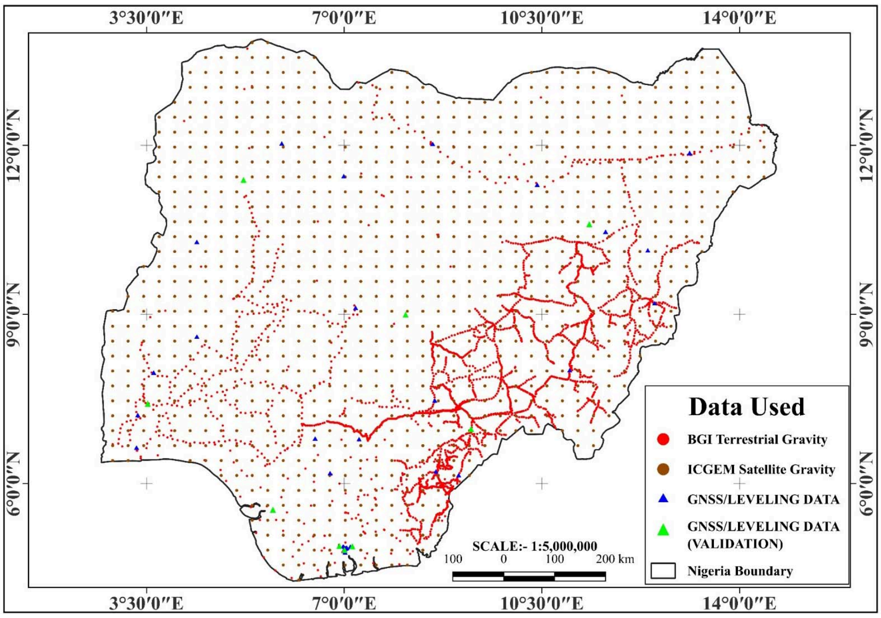

Figure 1. Datasets used for this study.

2.2. Methodology

The remove-compute-restore (R-C-R) method was used in this study. According to [1], this method takes into consideration the geoid's long, medium, and short wavelength components, which are obtained via Digital Terrain Models (DTM), terrestrial gravity, and global geopotential models. This method uses the previously described process of calculating the gravity anomalies and subsequently the geoid model, while accounting for the integration of the various wavelengths. Four main processes are involved in modeling the gravimetric geoid and fitting it to the geometric geoid model: *i.e.*, removal, prediction, restoration, and tailoring/fitting.

2.2.1. Gravity Anomalies from Gravity Data

There are different methods proposed over the years for gravimetric geoid modeling. These methods depend on the approach of gravity reduction such as simple or complete Bouguer anomalies, Faye anomalies and free-air anomalies etc. The methods of the treatment of the topographic masses are distinguished amongst the various techniques of gravity anomalies. In this study the basic free-air anomalies were first employed in the preliminary stage. Nevertheless, the Bouguer anomalies were employed in the conversion of the height anomalies (ζ) to the classical geoid (N). The estimates Bouguer, Δg_B, and simple Free air, Δg_{FA} anomalies are given in Eqs. (3) and (5).

$$\Delta g_{FA} = g + \delta y_A - \gamma_0 + 0.3086H \tag{3}$$

where: g: The observed terrestrial gravity., δy_A: The atmospheric correction after [8], γ_0: The normal gravity of a point on the ellipsoid (GRS80), $0.3086H$: The simple Free-air gradient multiplied by the height of the gravity station above the geoid.

And the normal gravity (γ_0) was evaluated numerically after Somigliana as:

$$\gamma_0 = \gamma_a \frac{1+k\sin^2\varphi}{\left(1-e^2\sin^2\varphi\right)^{1/2}} \quad \text{with } k = \frac{b\gamma_b}{a\gamma_a} - 1 \tag{4}$$

Where: γ_0: The normal gravity on the ellipsoid at a point φ, γ_a: The normal gravity at the pole, γ_b: The normal gravity at the equator, a,b: The semi-major and minor axes of the reference ellipsoid. The simple Bouguer anomalies were computed using Eq. (5):

$$\Delta g_B = g - A_B + F - \gamma_0 = g - 0.1119H + F - \gamma_0 \tag{5}$$

where: Δg_B: The simple Bouguer anomaly, g: Observed gravity, $0.1119H$: The Bouguer plate correction multiple by the height of the gravity station, F: Normal vertical gravity gradient = 0.3086H, γ_0: Normal gravity of a point on the ellipsoid (GRS80).

2.2.2. Evaluation of the Gravity Anomaly and Height Anomaly from Harmonic Coefficients

Global geopotential models (GGM) represent the solution of the boundary value problem for the global approach. In regional gravity field modelling, GGMs are used for computation of global, long-wavelength, contributions of different functionals such as the height anomaly ζ using [9]:

$$\zeta(\varphi,\lambda,r) = \frac{GM}{r\gamma} \sum_{n-2}^{n_{\max}} \sum_{m=0}^{n} \left(\bar{C}_{nm}\cos m\lambda + \bar{S}_{nm}\cos m\lambda\right)\bar{P}_{nm}(\sin\varphi) \tag{6}$$

where: $\bar{C}_{nm}$ and $\bar{S}_{nm}$ are the fully normalized geopotential coefficients of the anomalous potential, $\bar{P}_{nm}$ are the normalized Legendre functions, $n_{\max}$ is the maximum degree of expansion. $r = R + H$. R is the mean radius of the Earth and H the height of the evaluation point. Gravity anomalies are computed using the equation:

$$\Delta g_{GGM}(\varphi,\lambda,r) = \frac{GM}{r^2} \sum_{n-2}^{n_{\max}} (n-1) \sum_{m=0}^{n} \left(\bar{C}_{nm}\cos m\lambda + \bar{S}_{nm}\cos m\lambda\right)\bar{P}_{nm}(\sin\varphi) \tag{7}$$

The Geoid Undulation N is obtained by:

$$N_{GGM}(\varphi,\lambda) = \frac{T - 2\pi G\rho H^2}{\gamma} \tag{8}$$

In a similar manner the height anomaly is obtained as:

$$\zeta_{GGM} = \frac{T - \Delta g_{GGM} H}{\gamma} \tag{9}$$

Where: H is the height of the evaluation points. In this research EGM 2008 was used as reference to a maximum degree of 2190.

2.2.3. Evaluation of "Remove" Terrain Effects

The RTM approach was chosen for the computation of the terrain effects because it yields an optimal result and the residual gravity anomaly and indirect effect are smaller and smoother than with other methods, according to analysis done by various scholars in geoid modeling [10]. Additionally, it demonstrates that RTM reduction is one of the most accurate methods of gravity reduction in gravimetric geoid computation. In this study, the Residual Terrain Model (RTM) was used to compute the terrain effects by prism integration. One of the most used mass reduction techniques, mostly for quasi-geoid determination, is the RTM. This approach eliminates the topography's input and replaces it with an equivalent topography model.

As a result, masses fill up the gaps below the reference surface and the topographic masses above it are eliminated. The fine (detailed) resolution topography grid was averaged, and the average grid created by taking 9' × 9' moving averages over the coarse 3' × 3' mean height grid was then low pass filtered to create the reference surface. Geoid terrain impacts by prism integration were calculated using the FFT approach. In practice, the coarse topographic grid is utilized for the entire topography of the area being evaluated, while the detailed topographic grid is utilized up to a certain distance [11]. The resolution of the available detailed DTM determines the inner zone's radius. A grid with a lesser resolution can be utilized for points outside of this inner region.

This approach is fully implemented in the GRAVSOFT software, particularly inside the TCFOUR program [11] and [13], which is frequently used in applications of gravity field modeling. Considering the coarse/detailed grid system speeds up computation. Using this program, a bicubic spline interpolation approach is used to further densify the topographic data in a small inner zone surrounding the computation point. This allows for the integration of the inner zone's frequently significant effects [11]. The RTM terrain was directly evaluated by the *TCFOUR* program by Fourier (FFT) method.

Following [12] the topographic effect on gravity of the RTM reduction is computed using Eq. (10):

$$\Delta g_{\mathrm{RTM}} = G\rho \int_{-\infty}^{\infty}\int \int_{z=h_{ref}(x,y)}^{z=h(x,y)} \frac{z-h_p}{\left[\left(x_Q-x_P\right)^2+\left(y_Q-y_P\right)^2+\left(z_Q-h_P\right)^2\right]^{3/2}} \mathrm{d}x_Q\mathrm{d}y_Q\mathrm{d}z_Q \quad (10)$$

2.2.4. Evaluation of "Restore" Terrain Effects

The restore step follows after residual quasi-geoid $\zeta_{\Delta g}$ has been obtained in the compute step. The GGM and RTM contributions on the height anomalies ζ_{GGM} and ζ_{RTM} are computed using the same input parameters that were used in the remove step for computation of Δg_{GGM} and Δg_{RTM} contributions on gravity anomalies. The height anomaly, ζ_{GGM} from the GGM and height anomaly, ζ_{RTM} from the DTM are then added to the computed residual quasi-geoid ζ_{res}. The RTM terrain effects on the quasi-geoid is evaluated using Eq. (10) but evaluated in Eq. (11) by FFT, here reproduced in short form:

$$\zeta_{restore} = \zeta_{RTM} = \frac{G\rho}{\gamma} \int_{h_{ref}}^{h} \frac{1}{r} \mathrm{d}x\mathrm{d}y\mathrm{d}z \quad (11)$$

where $r = \left[\left(x_P - x\right)^2 + \left(y_P - y\right)^2 + \left(H_P - z\right)^2\right]^{1/2}$

2.2.5. Evaluation of Reference Fields from the Topography

The evaluation of the terrain effects, especially by the RTM approach, required coarse, detailed and a reference grid. The purpose of the reference grid is to provide optimal smoothing of the geoid effects. Thus, a reference grid height around 100km resolution was computed using the *TCGRID* subroutine. The *TCGRID* does two operations: it first makes an average grid and then filters the average grid with a moving average operator. The topography reference field was evaluated using TCGRID module in the GRAVSOFT program.

2.2.6. Evaluation of Reduced Gravity Values

The compute step, which determines the residual gravity field by subtracting the global and local gravity effects, comes after the remove step in the gravimetric geoid evaluation using the R-C-R approach. The computation stage uses residual gravity field data as input. The data are often gravity anomalies. Since there are multiple topographic reduction techniques available, there are various variations of the R-C-R methodology. Gridding can be done either before or after the removal step, and the input data can be either Faye or RTM anomalies.

The reduced gravity values were obtained using the following steps:

1) Start from the observations on the Earth's surface Δg_{FA}.
2) Compute long-wavelength contribution to the gravity Δg_{GGM}.
3) Compute RTM terrain effects on gravity $\Delta g_{terr.effects} = \Delta g_{RTM}$.
4) Obtain residual gravity anomalies $\Delta g_{RES} = \Delta g_{FA} - \Delta g_{GGM} - \Delta g_{RTM}$.
5) Interpolate (grid) residual gravity anomalies Δg_{RES}.

2.2.7. Evaluation of the Modified Stokes/Molodenskii Integral

In Stokes integration, each gravity anomaly Δg from the grid within the integration radius is multiplied with the Stokes function $S(\psi)$. Stoke's function can be computed spectrally using Legendre polynomial series or analytically by closed expressions. The spectral Stokes' function was employed in this research as shown as given in Eq. (12):

$$\text{Spectral}: S(\psi) = \sum_{n=2}^{\infty} \frac{2n+1}{n-1} P_n \cos(\psi) \tag{12}$$

However, the continuous integration of gravity anomalies across the entire sphere should be used to evaluate Stokes' integral; yet, these values are not available for integration over the entire sphere, particularly in regional gravity field modeling. Because of this, the integration can only be done inside the spherically defined area (σ_0) and not over the entire sphere (σ). Since local gravity data are known to contain errors in long wavelengths, information is thus lost in the remote zone where data are not integrated ($\sigma - \sigma_0$), resulting in long wavelength truncation errors. Long wavelength inaccuracies from gravity measurements therefore spread into the geoid under evaluation.

Molodenskii demonstrated that the modified Stokes' kernel function, which integrates the long wavelength contribution in the form of low-degree coefficients (up to degree L) from satellite-derived GGMs and terrestrial gravity data, may minimize the truncation error of the remote zone. The Stokes kernel function is altered in this study in accordance with [14]. The low degree Legendre polynomials are eliminated from the unaltered Stokes' function by the Wong and Gore modification. The height anomaly (ζ), is evaluated as given in Eq. (13):

$$\zeta_{res} = \frac{R}{4\pi\gamma}\iint_{\sigma}\left(\Delta g_{res} + G_1\right)S(\psi)\,\mathrm{d}\sigma \tag{13}$$

where: $G_1 = \frac{R^2}{2\pi}\iint\frac{\left(H - H_P\right)}{l_0^3}\Delta g\mathrm{d}\sigma$

The quasi-geoid is derived by summing the effects from the different gravity field as shown in Eq. 14:

$$\zeta = \zeta_{res} + \zeta_{RTM} + \zeta_{GGM} \tag{14}$$

The quasi-geoid is converted to the classical geoid using the relation in Eq. 15:

$$N = \zeta - \frac{\Delta g_B H}{\gamma} \tag{15}$$

where H_P: The evaluation point and H being the reference point.

3. Results and Discussion

The statistical results of the residual gravity anomaly, residual terrain effects are given on Table 2.

Table 2. Statistics of the RTM terrain effects (Remove effects).

Gravity Field/Unit: mGal	Max.	Min.	Mean	Std. Dev.	Remarks
Δg_{FA}	72.599	−70.960	3.592	21.111	1
Δg_{GGM}	58.292	−61.591	6.963	17.326	2
$\Delta g_{FA} - \Delta g_{GGM}$	71.245	−92.356	−2.190	14.719	3
Δg_{RTM}	140.445	−154.540	−0.079	9.971	4
$\Delta g_{FA} - \Delta g_{GGM} - \Delta g_{RTM}$	131.766	−92.318	−0.851	14.243	5
RTM ζ_{RTM}	1.999	−0.485	0.033	0.173	7
RTM Geoid Effects ζ_{RTM} (Niger Republic)	1.473	−0.306	−0.014	0.069	8

The RTM impacts should have a mean value and standard deviation that are nearly zero, according to the statistics in Table 2. The RTM effects on the geoid in this study are smooth because, as Table 2 illustrates, the mean value is close to zero. The acquired results are in line with the expected RTM anomalous property, which has a small indirect influence and the smallest power at short wavelengths. Furthermore, using the same methodology, [15] findings from the neighboring Niger Republic produced results that were similar to those shown in Table 2.

Additionally, it is preferable that the remaining gravity field quantity following the remove step be smooth and free of outliers or systematic biases in the data before gridding. The residual gravity anomalies are smooth, according to the data in Table 2, and they are consistent with readings from neighboring countries that used the same methodology.

The results of the residual gravity anomaly Δg_{RES} was gridded to a 3′ x 3′ grid using *GEOGRID* subroutine and this was input into the *SPFOUR* (GRAVSOFT) for the evaluation of the residual height anomaly ζ_{RES} after Molodenskii modified after Wong-Gore kernel modification. The statistic of the output is shown on Table 3.

Table 3. Procedure and statistics of the reduced height anomaly.

Gravity Field/Unit:(m)	Max.	Min.	Mean	Std. Dev.
FFT Contribution ζ_{res}	2.060	-2.195	-0.004	0.446

In this study, the geoid, as defined by Eqs. 14 and 15, was initially assessed as a quasi-geoid and then transformed into a geoid by applying the quasi-geoid to the geoid correction (ζ-to-N). Mountainous regions, including the Plateau and Taraba States in North Central and East of the research area, have the highest values of the (ζ-to-N) in absolute terms. These modifications have maximum range values greater than 24 cm. This modification is minor and occasionally disregarded in low-lying and coastal regions. Although it hasn't been accomplished yet, geodesists worldwide are working to create sub-centimeter geoid. The total accuracy of the geoid was evaluated for this study using GNSS/leveling, whose dependability is unknown. An estimate of the projected error budget of the geoid might have been obtained by performing an error propagation analysis to assess the undulations' error if the GNSS/leveling error had been known.

But given this clear fact, we assumed that the GNSS/leveling data to be errorless. As a result, Table 4 displays the comparison and overall level accuracy of the geoid for this study, which is 41 cm (decimeters level). The Nigerian Primary Geodetic Network's GNSS/leveling data, which mostly comes from the orthometric heights from the geodetic leveling network, is the main source of the significant disparity between the geometric and gravimetric geoids. Furthermore, unmodeled errors from the DEM utilized for this study, terrestrial gravity data, and the interpolation of the reduced gravity anomalies used in the Stokes or Molodenskii integral may potentially be responsible for the decimeter level precision attained.

Table 4. External assessment of gravimetric geoid with GNSS/levelling.

ID	S/N	Lat. dd	Long. dd	h (m)	H (m)	N^{GNSS} (m)	N^{GRAV} (m)	N^{GNSS}-N^{GRAV} (m)
A16	1.	10.1249	12.3759	786.6040	768.7680	17.8360	18.0830	0.2470
A39	2.	11.2889	10.4174	495.4990	474.7460	20.7530	21.3500	0.5970
C16	3.	6.1371	9.0267	628.4300	607.4730	20.9570	21.1740	0.2170
CFL56	4.	11.8532	13.1164	357.4050	340.6800	16.7250	17.1610	0.4360
CFH66	5.	6.1731	6.7501	57.3680	37.2140	20.1540	19.7030	−0.4510
CFA33A	6.	6.6269	3.3231	70.4120	47.0930	23.3190	23.7260	0.4070

Continued

H4	**7.**	**7.4627**	**8.6032**	**362.9030**	**341.7780**	**21.1250**	**20.5410**	**−0.5840**
L10	8.	7.2044	3.3449	197.8920	172.9870	24.9050	25.6210	0.7160
R43	9.	12.0212	5.8946	477.2400	456.4400	20.8000	20.9280	0.1280
U81	10.	6.7870	6.4857	215.8380	193.7200	22.1180	23.0190	0.9010
U78	11.	6.7764	7.2634	424.4120	402.0030	22.4090	23.2000	0.7910
ZVS3003	12.	4.8480	7.0478	35.3270	16.6140	18.7130	18.3650	−0.3480
L8	13.	7.9562	3.6267	464.8940	439.4110	25.4830	25.3410	−0.1420
L18	14.	8.5956	4.3915	458.4220	434.3450	24.0770	23.4510	−0.6260
D13	15.	10.2756	4.3907	290.6730	268.1180	22.5550	22.1010	−0.4540
K01	16.	12.0143	8.5664	504.2310	482.9880	21.2430	20.7170	−0.5260
C014	17.	6.2028	8.6243	148.3030	127.2320	21.0710	21.2820	0.2110
N123A	18.	11.4412	6.9920	769.7730	747.9120	21.8610	21.5390	−0.3220
N032	19.	9.1060	7.2016	708.8040	686.0680	22.7360	22.0860	−0.6500
A001	20.	9.1888	12.4961	217.9380	200.5570	17.3810	18.3160	0.9350
C036	21.	7.9988	10.9930	543.6250	524.4710	19.1540	19.3050	0.1510
A21	22.	10.4553	11.6280	758.9630	740.3310	18.6320	18.7310	0.0990
AP1	23.	4.8695	6.9779	33.7200	14.8081	18.9119	18.8199	−0.0920
HS8	24.	4.7651	7.0166	26.0280	6.9860	19.0420	19.0350	−0.0070
PT 4 Emma	25.	4.7984	7.0056	30.6930	11.6906	19.0024	18.9524	−0.0500
PT 8 Emma	26.	4.8338	7.0070	26.7890	7.8509	18.9381	18.8381	−0.1000
PT 5 Emma	27.	4.8069	7.0094	29.3740	10.3801	18.9939	18.9339	−0.0600
PT 9 Emma	28.	4.8366	7.0153	29.1410	10.1660	18.9750	18.8860	−0.0890
PT 2 Abdul	29.	4.8443	7.0395	32.6400	13.6539	18.5861	18.5161	−0.0700
PT 3 Abdul	30.	4.8408	7.0313	26.7500	7.7697	18.9803	18.9093	−0.0710
AP4	31.	4.8683	6.9899	35.8490	16.9261	18.9229	18.8349	−0.0880
PP5	32.	4.8703	7.1089	38.8020	19.7522	19.0498	19.0028	−0.0470
PT 4 Abdul	33.	4.8372	7.0229	32.8420	13.8392	19.0028	18.9558	−0.0470
PT 3 Emma	34.	4.7902	7.0023	25.1950	6.2283	18.9667	18.8907	−0.0760
PT 6 Emma	35.	4.8155	7.0098	34.5140	15.4366	19.0774	19.1044	0.0270
							RMS	**41 cm**

Additionally, the data showed that the quasi-geoid had a tilt and/or slope, supporting the conclusions of earlier research conducted in the region by [16] and [17]. As seen in **Figure 2(a)** and **Figure 2(b)**, this tilt and/or slope extends from the north central and southwestern regions to the research area's edges. The degree of proximity between the two surfaces was revealed by the fitness between the gravimetric and geometric geoid. The central and southwest regions of the research area had the highest values of the undulations, and the geoid values throughout Nigeria show that the geoid is above the ellipsoid.

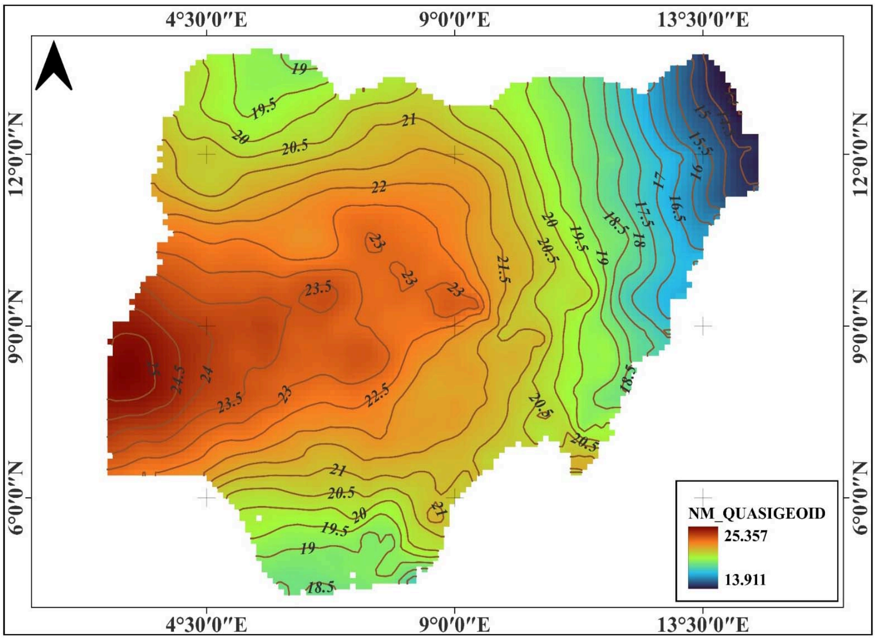

(a)

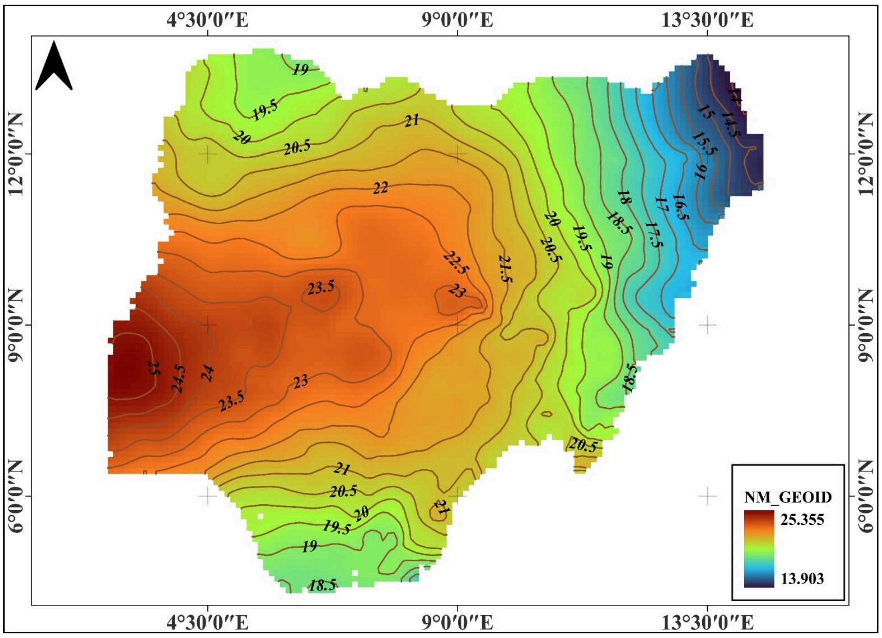

(b)

Figure 2. (a): Quasi-geoid over Nigeria; (b): Geoid over Nigeria.

The degree of agreement between the geometric and gravimetric geoids, that is, (N^{GNSS}-N^{GRAV}) is shown pictorially Figure 3. This clearly shows whether the geometric geoid is below and/or above the gravimetric geoid.

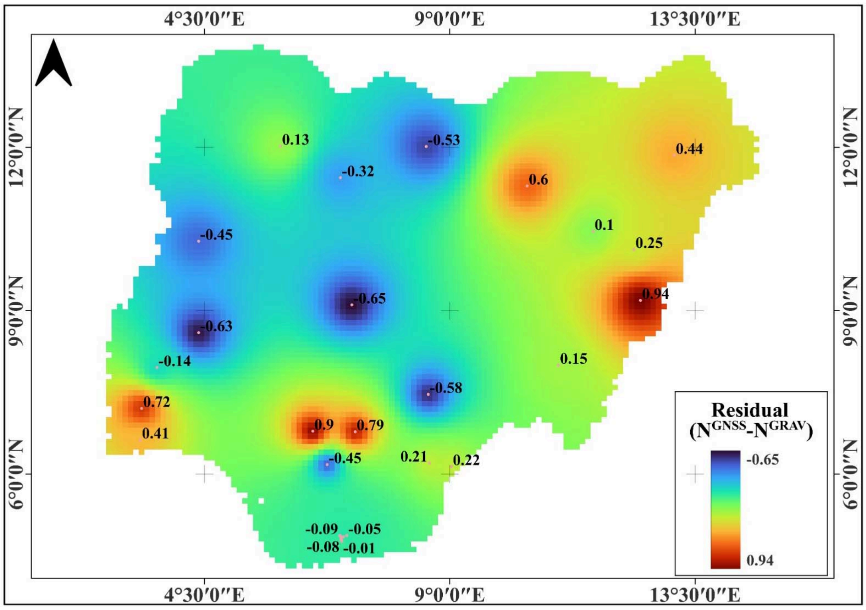

Figure 3. The residuals between the geometric and gravimetric geoid over Nigeria.

However, the recent GNSS/leveling dataset acquired from the office of the Surveyor's General Rivers State was used exclusively to evaluate the geoid file, revealing a centimeter level of accuracy as shown in **Table 5** to demonstrate that the modelled geoid in this study and the level of accuracy achieved for the gravimetric geoid across Nigeria is at centimeter level.

Table 5. External assessment of gravimetric geoid with GNSS/levelling (Rivers state).

ID	S/No	Lat. dd	Long. dd	h (m)	H (m)	N^{GNSS} (m)	N^{GRAV} (m)	N^{GNSS}-N^{GRAV} (m)
AP1	1.	4.8695	6.9779	33.7200	14.8081	18.9119	18.8199	−0.0920
HS8	2.	4.7651	7.0166	26.0280	6.9860	19.0420	19.0350	−0.0070
PT 4 Emma	3.	4.7984	7.0056	30.6930	11.6906	19.0024	18.9524	−0.0500
PT 8 Emma	4.	4.8338	7.0070	26.7890	7.8509	18.9381	18.8381	−0.1000
PT 5 Emma	5.	4.8069	7.0094	29.3740	10.3801	18.9939	18.9339	−0.0600
PT 9 Emma	6.	4.8366	7.0153	29.1410	10.1660	18.9750	18.8860	−0.0890
PT 2 Abdul	7.	4.8443	7.0395	32.6400	13.6539	18.5861	18.5161	−0.0700
PT 3 Abdul	8.	4.8408	7.0313	26.7500	7.7697	18.9803	18.9093	−0.0710
AP4	9.	4.8683	6.9899	35.8490	16.9261	18.9229	18.8349	−0.0880
PP5	10.	4.8703	7.1089	38.8020	19.7522	19.0498	19.0028	−0.0470
PT 4 Abdul	11.	4.8372	7.0229	32.8420	13.8392	19.0028	18.9558	−0.0470
PT 3 Emma	12.	4.7902	7.0023	25.1950	6.2283	18.9667	18.8907	−0.0760
PT 6 Emma	13.	4.8155	7.0098	34.5140	15.4366	19.0774	19.1044	0.0270
							RMS	**7 cm**

Results of the Cross Validation of the GNSS/Levelling Data

The disparity between the derived and observed orthometric heights nationwide was fitted or tailored using a seven-parameter empirical model as shown in Eqs. 16 to 18:

gravimetric geoid can be expressed as:

$$l_i = h_i - H_i - N_i = A_i x - v_i \quad (16)$$

$$Ax = \left(N_{GPS/leveling} - N_{grav}\right) + v \quad (17)$$

where A is the design matrix, x is the vector of unknown parameters and v is the vector of the unknown random errors coming from GPS and levelling observations and geoid itself. Even though the choice of the appropriate parametric model, AX depends on the distribution, density and the quality of the data used, in this thesis, we used a simplified 7-parameter version of the usual 7-parmeter similarity datum shift transform model to derive the corrector surface model after [3]. It has also been used in previous studies by [18]. The 7-parameter model can be expressed mathematically as:

$$A_i x = \cos\varphi_i \cos\lambda_i x_1 + \cos\varphi_i \sin\lambda_i x_2 + \sin\varphi_i x_3 + \frac{\cos\varphi_i \sin\varphi_i \cos\lambda_i}{W_i} x_4 + \frac{\cos\varphi_i \sin\varphi_i \sin\lambda_i}{W_i} x_5 + \frac{\sin^2\varphi_i}{W_i} x_6 + x_7 \quad (18)$$

where φ_i, λ_i, the geodetic coordinates of the GPS/leveling points, e is the eccentricity of the reference ellipsoid and $W_i = \sqrt{1 - e^2 \sin^2\varphi_1}$. The vector of the unknown parameters are $x_1, x_2, x_3, \cdots$ and x_7.

A cross-validation of the GNSS/leveling data subset was performed. This is to guarantee that, following the interpolation and transformation process, the customized or hybrid geoid may produce orthometric heights that are dependable to a specific degree of precision. In order to determine the associated orthometric heights, the corresponding geoid values were interpolated from the hybrid geoid file and then deducted from the ellipsoidal heights of these points. As indicated in Table 6, the hybrid geoid (post-fit) is accurate to 3 cm root mean square (r.m.s.) when the derived or transform orthometric height is compared with the observed orthometric height.

Table 6. Results of the cross-validation.

Station's Attribute	Lat. (dd)	Long (dd)	h(m) Observed	H (m) Observed	H* (m) Derived	(H-H*) (m)	Source
C21	6.9687	9.2468	344.6080	324.6000	324.5950	0.005	OSGOF
A24	10.6038	11.3397	624.6253	605.6290	605.6293	−0.003	OSGOF
D29	11.3880	5.2173	526.7924	505.5490	505.5474	0.002	OSGOF
N25	8.9988	8.0874	591.9590	570.1200	570.1160	0.004	OSGOF
CBL10	5.5393	5.7379	25.8125	4.7930	4.8005	−0.008	OSGOF
L03	7.4173	3.5209	290.3270	264.2840	264.2980	−0.014	OSGOF

Continued

PT 7 Emma	**4.8239**	**7.006**	**33.3790**	**14.3716**	**14.4470**	**−0.075**	**SG's Rivers**
Uniport	4.8937	6.9144	29.7120	10.8670	10.8654	0.002	SG's Rivers
PP9	4.8883	7.1445	33.5700	14.4602	14.5040	−0.044	SG's Rivers
						RMS	**3 cm**

4. Conclusions

Distortions or residuals are always present in any normal geoid derivation, fitting, and transformation process from 3D GNSS-derived ellipsoidal height to gravity-related 1D orthometric height. The transformation process through interpolation, systematic mistakes caused by the various contributors to the geoid, and inconsistent datums could all be to blame for this. For example, it was found that the gravity and gravity anomaly datasets acquired from BGI were calculated using the GRS67 reference ellipsoid, but the global ellipsoid, such as WGS84 or GRS80, is now used for gravimetric geoid computation. Long wavelength inaccuracy would have resulted from ignoring this. Over Nigeria, the effect is roughly 0.87 mGal. Thus, conversion was carried out from GRS67 to GRS80 prior to computation.

Additionally, it is anticipated that any gravity reduction procedure for gravimetric geoid modeling will result in residual gravity anomalies that are smooth, have negligible indirect effects, and have geophysical significance. It should be noted that the defects present in the Nigerian vertical network have not been eliminated by the fitting and transformation procedure outlined in this work (**Table 6**). However, it has only harmonized the corresponding points on the two surfaces (N^{GNSS} and N^{GRAV}), producing results that are compatible throughout the research region and repeatable and consistent. Using Spherical Harmonic Coefficients (EGM08) as a reference field, the standard remove-restore method was used to generate the geoid. Spherical Fast Fourier Transform (FFT) and Residual Terrain Modelling (RTM) by prism integration were applied. The FFT's use is based on the idea that it is quick and effective, especially when performing calculations across wide areas where the traditional integration of the Stokes/Molodenskii integral in the space domain takes a long time.

After a thorough evaluation as a quasi-geoid, the gravimetric geoid model over Nigeria was transformed into a classical geoid by applying the $N-\zeta$ adjustment. The gravimetric geoid's strength and details are reflected in the geoid model at short range, while the leveling networks' trends are reflected at long range. It is crucial to remember that the GNSS/leveling data throughout Nigeria, not the geoid model, is what makes it difficult to utilize GNSS to determine suitable gravity-related (Orthometric) height. It should be noted that systematic mistakes and land uplifts are likely to cause tilts in the final geoid model. Therefore, the geoid surface from fitting is a corrective surface rather than an equipotential surface. A graphic user interface (GUI) using the interpolation program Height Transformation Model, which enables height users to interpolate geoid values and then convert ellipsoidal heights to orthometric heights or vice versa, provides access to the geoid surface and the underlying gravimetric geoid file.

Acknowledgements

The authors wish to thank the Bureau Gravimetrique International (BGI) for the release of terrestrial gravity for this research and acknowledge the producers of the GRAVSOFT software that was used in the computation.

Conflicts of Interest

The authors declare no conflicts of interest regarding the publication of this paper.

References

[1] Sansò, F. and Sideris, M.G. (2013) Geoid Determination: Theory and Methods. Springer. https://doi.org/10.1007/978-3-540-74700-0

[2] Adams, R., IIiffe, J., Ziebart, M., Turner, J. and Oliveira, J.F. (2006) Joining up Land and Sea: UKHO/UCL Vertical Offshore Reference Frame. *Hydro International*, **10**, 7-9.

[3] Hofmann-Wellenhof, B. and Moritz, H. (2006) Physical Geodesy. Springer. https://doi.org/10.1007/978-3-211-33545-1

[4] Sjoberg, L.E. and Bagherbandi, M. (2017) Gravity Inversion and Integration: Theory and Applications in Geodesy and Geophysics. Springer. https://doi.org/10.1007/978-3-319-50298-4

[5] Bureau Gravimetrique International (2015) Land and Marine Gravity Data.

[6] Ince, E.S., Barthelmes, F., Reißland, S., Elger, K., Förste, C., Flechtner, F., *et al.* (2019) ICGEM—15 Years of Successful Collection and Distribution of Global Gravitational Models, Associated Services, and Future Plans. *Earth System Science Data*, **11**, 647-674. https://doi.org/10.5194/essd-11-647-2019

[7] Alaska Satellite Facility (2020) ALOS PALSAR—Digital Elevation Model (12.5 m Spatial Resolution. https://asf.alaska.edu/data-sets/derived-data-sets/alos-palsar-rtc/alos-palsar-radiometric-terrain-correction

[8] Wichiencharoen, C. (1982) The Indirect Effects on the Computation of Geoid Undulations. Report No. 336, Dept. of Geodetic Science and Surveying, The Ohio State University, Columbus.

[9] Barthmeles, F. (2013) Definition of Functionals of the Geopotential and Their Calculation from Spherical Harmonic Models: Theory and Formulas Used by the Calculation Service of the International Centre for Global Earth Models (ICGEM). Deutsches GeoForschungZentrum GFZ: Scientific Technical Report STR09/02. https://doi.org/10.2312/GFZ.b103-0902-26

[10] Stelios, P.M. (2010) Gravity, Geoid and Earth Observation. Springer.

[11] Forsberg, R. (2010) Terrain Effects in Geoid Computations. *Lectures Note*, *International School for the Determination and Use of the Geoid*, Saint Petersburg, 28 June-2 July 2010, 159-181.

[12] Tscherning, C.C. (2012) Geoid Determination by 3D Least-Squares Collocation. In: Sansò, F. and Sideris, M., Eds., *Geoid Determination*, Springer, 311-336. https://doi.org/10.1007/978-3-540-74700-0_7

[13] Forsberg, R. (1984) A Study of Terrain Reductions, Density Anomalies and Geo-

physical Inversion Methods in Gravity Field Modelling. Department of Geodetic Science and Surveying, The Ohio State University, No. 355.

[14] Wong, L. and Gore, R. (1969) Accuracy of Geoid Heights from Modified Stokes Kernels. *Geophysical Journal International*, **18**, 81-91. https://doi.org/10.1111/j.1365-246x.1969.tb00264.x

[15] Yahaya, S.I. and Azzab, D.E. (2018) High-Resolution Residual Terrain Model and Terrain Corrections for Gravity Field Modelling and Geoid Computation in Niger Republic. *Geodesy and cartography*, **44**, 89-99. https://doi.org/10.3846/gac.2018.3787

[16] Ezeigbo, C.U. (1991) Estimation Models of Geoid in Nigeria Using Doppler Satellite Observations. In: Rapp, R.H. and Sansò, F., Eds., *International Association of Geodesy Symposia*, Springer New York, 230-240. https://doi.org/10.1007/978-1-4612-3104-2_28

[17] Ezeanaka, E.E. (1987) A Study of the Local Geoid Using Integral Equivalents of Stokes and Vening Meinesz Equivalents. Master's Thesis, University of Nigeria.

[18] Fotopoulos, G. (2003) An Analysis on the Optimal Combination of Geoid, Orthometric and Ellipsoidal Height Data. PhD Thesis, University of Calgary.

International Journal of Geosciences, 2026, 17(1), 66-87
https://www.scirp.org/journal/ijg
ISSN Online: 2156-8367
ISSN Print: 2156-8359

Multi-Scale Analysis of Erosion and Sediment Transfer Processes on Grand-Lahou Beach

N'Doufou Gnosseith Huberson Claver[1], **Gbangbot Jean-Michel Kouadio**[2], **Saimon Aby Atsé Mathurin**[3]*

[1]Department of Geosciences, University Peleforo GON COULIBALY of Korhogo, Korhogo, Côte d'Ivoire
[2]Departement of Environment, Laboratory of Environmental Science and Technology, University Jean Lorougnon Guédé, Daloa, Côte d'Ivoire
[3]Department of Environment, Laboratory of Marine Physics and Geology, Oceanographic Research Center, Abidjan, Côte d'Ivoire
Email: gnosseith3@gmail.com, gbangbotjeanmichel@yahoo.fr, *saimonaby@yahoo.fr

How to cite this paper: Claver, N.G.H., Kouadio, G.J.-M. and Mathurin, S.A.A. (2026) Multi-Scale Analysis of Erosion and Sediment Transfer Processes on Grand-Lahou Beach. *International Journal of Geosciences*, **17**, 66-87.
https://doi.org/10.4236/ijg.2026.171005

Received: August 23, 2025
Accepted: January 26, 2026
Published: January 29, 2026

Abstract

This study was carried out to report on the hydro-sediment dynamics of Grand-Lahou beach at different time scales over the last twenty-five years. It is based on two complementary methods: the method of sediment reworking based on continuous altimetric monitoring of posts during a tidal cycle and in situ tracing using fluorescent-coloured sand, and the method of monitoring changes to the beach based on topographical profiles at different time intervals (seasonal, annual, multi-year, ten-year). The sediment balances were established by determining the areas eroded and/or greased using the trapezoidal or triangular surface calculation method to precisely quantify the sediment movements in the profile and the associated dynamics. The results obtained show that the dynamic swash zone varies according to the phases of the tide. On the ebb tide, this zone is reduced to the low foreshore and a few points on the mid-foreshore, depending on the tide-swell couple. When the tide is flowing, the zone widens, taking into account the high foreshore. The morphology of the submerged zone changes constantly as the tide passes over it. The low offshore shows a trend towards stability with weak erosion episodes. The mid-foreshore shows a predominance of fattening, with the highest movements of instantaneous reworking (RrI) on the foreshore. The maximum amplitude of sediment movement of 25.5 cm was obtained at mid foreshore. The morpho-sedimentary monitoring of the beach reveals that the most important retreats, estimated at 25 m.an-1 were observed during exceptional events including storms. Erosion in the area around the mouth of the Bandama River is the main threat to the people living along the river, given the damage that has been caused.

Keywords

Reworking, Amplitude, Sedimentary Balance, Erosion, Fattening

1. Introduction

The coastal area represents only 5% of the land area [1]. Yet more than 20% of the world's population lives less than 30 km from the coast [2]. It is impacted by various human activities but also by the effects of climate change such as sea level rise, changes in storm regimes and the risks of submersion and floods [3]. The evolution of sandy coastlines is generally dominated by a trend towards erosion. Studies conducted in recent years in different regions of the world show that the erosion of sandy coasts is a global phenomenon. According to Bird (1993) [4], More than 70% of the world's sandy beaches are thought to be eroding. It is, therefore, a fragile environment that must be protected. In Côte d'Ivoire, some coastal areas show worrying signs of destabilization. Such is the case of Grand-Lahou beach. Indeed, the erosion of the coast of Grand-Lahou is worrying. Initially located on the cordon near the mouth of the Bandama, the city was relocated to 18 km on the north shore of the lagoons due to erosion. Coconut plantations and historic buildings (gendarmerie, civil prison, sub-prefecture, hospital, maternity, school, lighthouse, etc.) have not escaped the destruction caused by erosion. The disappearance of the rocky banks under the mud at Grand-Lahou beach would leave this area without any natural defences and particularly vulnerable to erosion [5]. Erosion is exacerbated by a lateral (east-west) migration of the mouth of the Bandama River [5]-[7]. Since 1993, 765 m of coastline has been destroyed [7]. Between 1912 and 1955, the mouth of the Bandama would have moved about 2 km [8]. Despite the extent of the damage, the local population, due to its main activity which is fishing refuses to leave the cordon. It moves as the sea advances. The retreat of the shoreline inherent in the migration of the pass has the corollary of destroying habitats and reducing the space available for construction. A loss of 10.7 ha, including 4 ha of built area between 1993 and 2006 was estimated by Hauhouot (2008) [6]. The population is watching helplessly as the Lahou-Kpanda cemetery is destroyed. The Catholic mission that houses a primary school is threatened with destruction due to migration from the past. Shorelines and beaches are systems that evolve at different scales of time and space depending on forcing agents such as waves, tides and associated currents [9]. In order to better characterise the evolution of the beach and surface reworking processes, monitoring was carried out on several time scales. The study is based on a number of in situ measurement campaigns, which make it possible to monitor changes in the surface sediment cover, and to highlight erosion and deposition phases as a function of tide gauge conditions on the foreshore [10] [11]. For short-term sedimentary evolutions (tidal cycle), single-tidal sediment level variation measurement devices have been implemented in the swash zone [12] [13]. Specific hydrodynamic processes in the swash determine the direction of sediment movement, towards the coastline where deposition can occur, or towards the inner zone, with the sediment potentially being dispersed offshore [14]. Swash oscillations (shore jet, retreat sheet) play a significant role in beach morphology [15]. For the medium-term follow-up (annual scale), long-term (multi-annual scale) profiles were made in some stations (mouth, catholic mission...) along the radials. These measurements make it possible to monitor erosion-sedimentation rhythms and relate them to episodes of greater agitation [10] [16]. This additional study of the hydrosedimentary processes will enable us to highlight the evolutionary trends on different spatiotemporal scales that will be useful for managing the Grand-Lahou coastline.

2. Materials and Methods

2.1. Main Characteristics of the Study Area

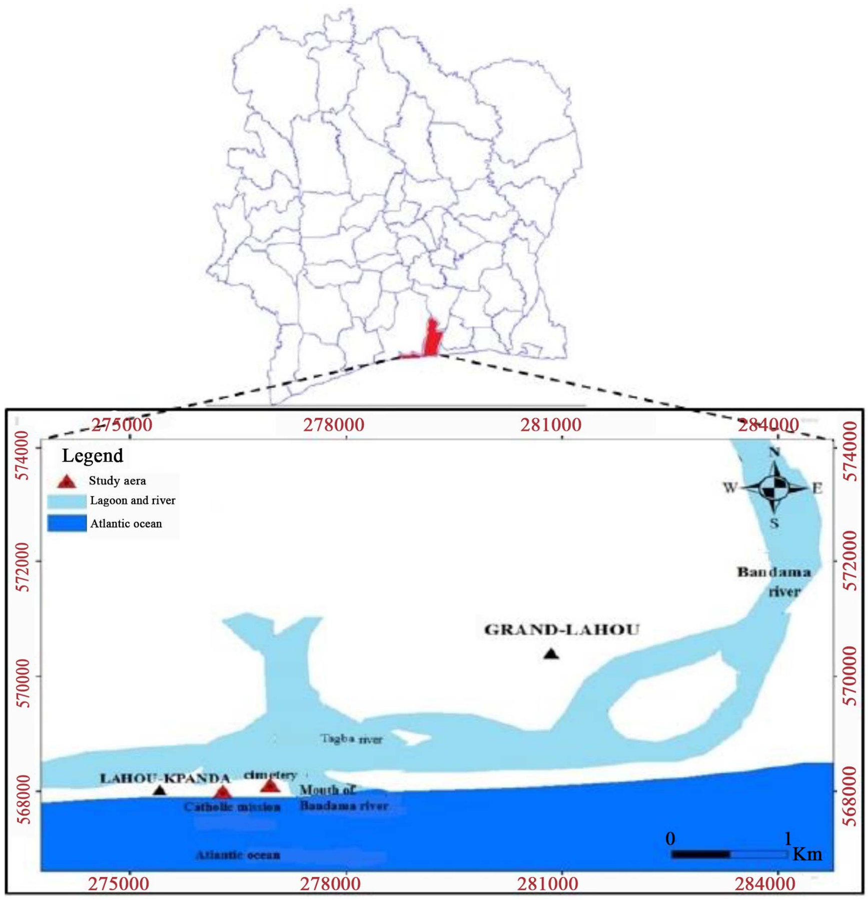

Figure 1. Grand-Lahou coastal zone.

The study area (Figure 1) is part of the Ivorian sedimentary basin, which covers 3/5 of the country's Atlantic coastline [17]. Located between latitudes 5˚9 North and 5˚12 North and longitudes 4˚56 West and 5˚20 West [18]. It is oriented in an average direction of 81˚, parallel to the Atlantic Ocean. This configuration is the very type of barrier cordon that isolates a body of water. The area to the west of the mouth of the Bandama river is the chosen study zone (Figure 1). In the region, the shoreline is frequently battered by swells with amplitudes of between 0.80 and 2.00 m and periods of 10 to 12 seconds. Exceptionally, larger swells with periods of up to 20 s break on the coast [19]. They are very destructive. The swells that usually break in the region, despite their average characteristics, have significant morphological effects on the coastline in the current dynamic context. They approach the shore from a preferential south-westerly to southerly direction. The swells approach Grand-Lahou-Abidjan stretch of coast at an angle of 60˚ [20], so that there is a strong littoral drift estimated at 800.000 m^3 of sand per year [21]. It is therefore a section of the coast dominated by sedimentary transport. In 1952, the Bandama river enters the Tagba lagoon and digs a passage through the cordons [19]. There are three channels in the estuary [18]. To the south, the river channel, whose depth varies between 7 and 8 m, runs alongside the Braffedon spit. It is crossed [22] by sometimes antagonistic currents (flow, downstream). To the north, the lagoon channel is 6 m deep. At the pass, the lagoon channel has a depth of 5 m. These channels are generally made up of medium to fine sands [23]. The grain size of beach sands varies between 409 µm and 719 µm [23].

2.2. Morphological Evolution of the Beach

The fieldwork carried out in 1998, 1999, 2006, 2007, 2008, 2017, 2018, 2022 and 2023 consisted of surveying the profiles perpendicular to the shoreline using a level (or theodolite), a mire and a tripod. The surveys were carried out so that they could be compared with previous data obtained from topographic profiles set against reference benchmarks. Profiles are set using topographic nails placed on stable areas [24]. The accuracy of the measurements is in the order of centimeters with a maximum vertical error of 2.2 cm [24]. The surveys were carried out at low tide to explore the maximum width of the beach. In this study, the beachbreak was taken as the reference line representative of the coastline. In the case of sandy coasts, the beach ado proves to be the most reliable [25]. It is marked by an easily identifiable break in the slope. The sedimentary balance sheets were carried out by comparing the first and the last profiles taken for the seasonal, annual and decennial scale. The aim is to quantify the sediment balance over the longest study period. Sediment balances were established from the determination of eroded and/or greased areas by the trapezoid method [26] to precisely quantify sedimentary movements in the profile and associated dynamics.

2.3. Sedimentary Reworking

The study focuses on determining the layer (thickness) of sediment equivalent to the total balance of hydro-sedimentary mobilisation and transport processes at the water-sediment interface. It is based on the sediment reworking method, using continuous altimetric monitoring of the stakes (every 5 minutes) during the tidal cycle of 22/12/2018. This cycle is 12 hours on the ivorian coasts. The tidal range deduced from the water levels described by the shom on behalf of the port of Abidjan is 0.746 m. The daily average significant wave height (Hs) obtained from the ERA programme is 1.083 m. These measurements enable us to study the response of the beach to wave loads by quantifying erosion depths and the thickness of the moving sediment layer [11].

2.4. Altimetric Monitoring of Beaches

The evolution of the beach during a tidal cycle has consisted of high-frequency topographic measurements made on stakes following a cross-shore profile [27] [28]. The main originality of this study consists in measuring the topographical changes of the Grand Lahou beach when it is subjected to the action of hydrodynamic forcing (tide, swell, etc). The process was inspired by the method developed by Sallenger and Richmond (1984) [27]. Morphological variations in the beach, monitored by means of topography, are measured in relation to an initial state, using stakes as reference points. The stakes were placed at low tide across the beach at 2 m intervals. A control profile on which 13 pickets were implanted allows a relevant interpretation of the results. Readings are taken on each stake every five minutes, limiting measurement errors and providing precise information on changes in beach morphology [27]. However, reading errors related to the manual method may still occur. These errors are less than half a centimetre.

2.5. Movement Envelope Curve

The states of each profile are superimposed. The points with the greatest difference in height on all the superimposed profiles are marked. They define the upper envelope curve. The lowest points in elevation are also identified. They define the lower envelope curve. The superposition of the upper and lower envelope curves gives the envelope curve of sediment movements on the profile.

2.6. Amplitudes of Sediment Movements in the Tidal Cycle

The difference between the heights of the stakes fixed in the ground (RrI) is calculated consecutively for the monitoring period at the time of the waves. The cumulative resulting reshuffle (RrC), which accumulates the values of the instantaneous resulting reshuffle (RrI) over the follow-up time, is also calculated. These two parameters provide information on the amplitude of sediment movements in the tidal cycle. the greatest value between the instantaneous resultant reshuffle (RrI) and the cumulative resultant reshuffle (RrC) represents the maximum amplitude of sedimentary movements at a point.

3. Results

3.1. Beach Dynamics on the Scale of the Tidal Cycle

3.1.1. Amplitude of Movement of Sediments in the Catholic Mission Low Foreshore

a. Amplitude of movement at station A

Instant resulting reshuffle (RrI)

Point A11 is 24.7 m from the coastline (TC). On the ebb, the RrI curves of A11 and A12 are very tightly jagged with slight steep undulations but no peaks (**Figure 2**). The extremes are −2 cm and 3 cm at point A12. These curves show a beach area that is tending to stabilise. No real trend can be seen at these two points on the lower foreshore. At the flow, that is to say from 10h45mn the curves RrI are presented in sawtooth with very pronounced teeth and sometimes strong peaks. The extremities are 6 cm and -5 cm at point A11. We gradually attend the immersion of the pickets until total immersion for A12 at 13 h 20 mn and at 14 h 05 mn for A11. As wave energy is very high due to the approach of high tide, it is difficult to read the values of posts A11 and A12, which makes it difficult to carry out a complete study of the instantaneous reshuffle of the low foreshore. The maximum amplitude of sediment movement could reach 11 cm for the RrI. The low foreshore is more dynamic at this phase of the tide.

Cumulative resulting reshuffle (RrC)

At the flow, the measurement of the low shore pickets is practically impossible because the pickets were submerged. The trends will therefore be more visible than at ebb tide. During this phase, points A11 and A12 behave differently. A11 becomes progressively fatter until high tide, when it erodes, reaching a peak of -9 cm. A12, on the other hand, erodes until high tide, when it begins its fattening phase, reaching a peak of 11 cm. The maximum amplitude of sediment movement is 15 cm for the RrC.

b. Amplitude de mouvement sur la station témoin (station B)

Point B11 is 21.4 m from the coastline (TC).

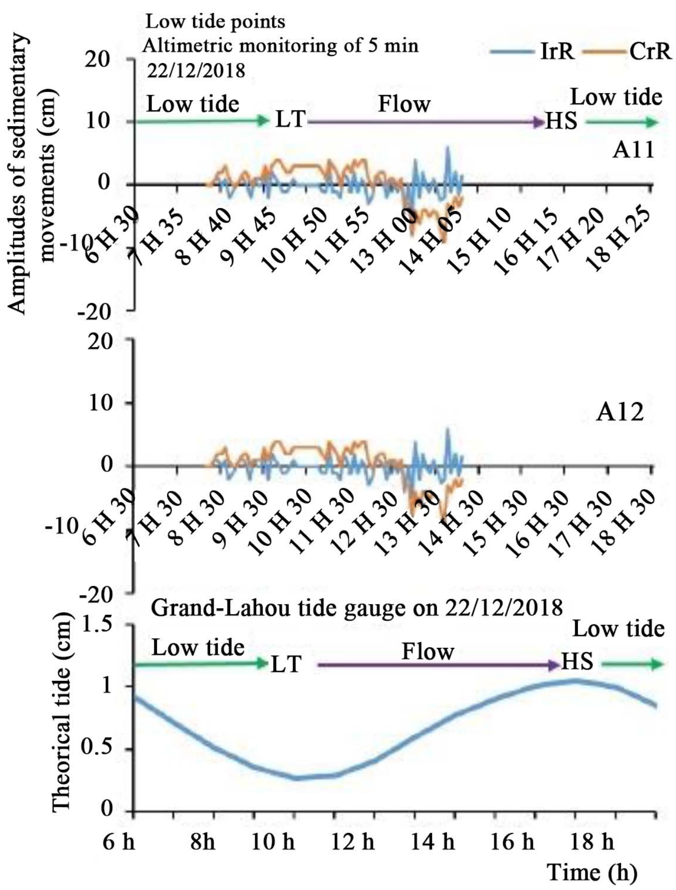

Figure 2. Continuous monitoring curves from the beach to the low foreshore at station A.

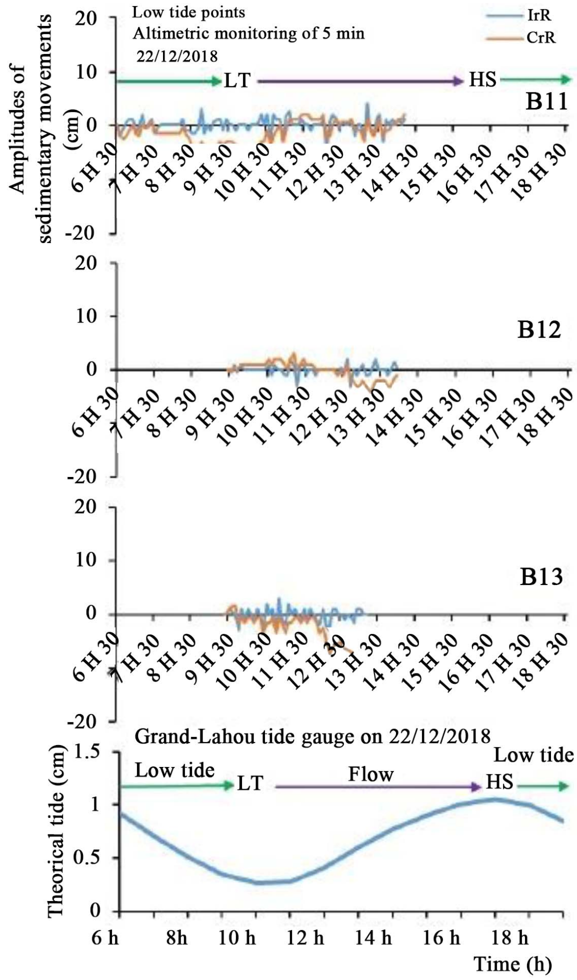

Figure 3. Continuous monitoring curves from the beach to the low foreshore at the control station.

Instant resulting reshuffle (RrI)

During the flow, points B13 and B12 could not be implanted due to the height of the waves on the low foreshore. It was only possible to implant them at low tide. The RrI of B11 shows stabilization with slight peaks (Figure 3). The movements are less equivalent to compassassions. The observed extremities are −3 cm and 3 cm. The RrI curve for B13 obtained at ebb tide shows that the movements are quite strong at this point. The tight sawtooth morphology is evidence of this. The RrI curve for B12 has an irregular sawtooth shape with no peaks. The RrI curve for B11, which is close to the mid-foreshore, shows trends with peaks at 4 cm and −4 cm. The maximum amplitude of sediment movement is 8.5 cm for the RrI.

Cumulative resulting reshuffle (RrC)

At the flow, the presence of a strong water column on the low foreshore makes it difficult to understand the morphology of this part of the foreshore. For the time period monitored, the RrC curve for B11 is below the initial altimeter level. The other two points, B12 and B13, show curves that differ very little from the initial level. The low foreshore is therefore eroding very little and is tending towards stability in the direction of the sea. The extremities are −6 cm and 0.5 cm. These values confirm a low erosion range that tends towards stability. On the ebb tide, the low foreshore points show a generally stable trend with occasional episodes of slight erosion. The extremes are observed at point B13 with −8.5 cm and 1.5 cm. The maximum amplitude of sediment movement is 10 cm for the RrC in this part of the foreshore.

3.1.2. Amplitude of Sediment Movement at the Catholic Mission Mid-Foreshore

a. Amplitude of movement at station A

Instant resulting reshuffle (RrI)

On the ebb, the RrI curves are straight with slight saw-tooth shapes and no peaks (**Figure 4**). This absence of peaks is due to the fact that wave movements are not strong enough to reveal peaks in the curves. The curves for the ebb tide show a phase of stability with episodes of low fattening. The extremes are observed at point A9 and are −11.5 cm and 7.5 cm. At flow, the RrI curves are narrow and peaks with medium to very strong trends as we approach the low range (A6 to A9). These curves show the morphological construction process. The RrI curve at A9 has no peaks because it is very close to the low foreshore. The extremes are −8 cm and 6 cm at point A8. The maximum amplitude of sediment movement is 19 cm for the RrI.

Cumulative resulting reshuffle (RrC)

On the ebb tide, the curves of RrC indicate that all the pickets in the middle are fattening. As posts A6, A7, A8 and A9 are no longer accessible to waves during low tide, their morphology is the result of previous processes. During the flood, three (3) phases can be identified for A10: the fattening observed during the ebb continues until 13:20 when, as the water rises, there is sudden erosion followed by a second phase of fattening. During the flow, three (3) phases can be identified for A10: the fattening observed during the ebb continues until 13:20 when, as the water rises, there is sudden erosion followed by a second phase of fattening. After 2.30 pm during high tide, the A10 picket is inaccessible. Stakes A7 and A8 are also going through the same phases as stake A10, but at different stages. For posts A6 and A9, there is no general trend towards increased sedimentation. The maximum amplitude of sediment movement is 15.5 cm for the RrC.

b. Amplitude of movement at the control station (station B)

Instant resulting reshuffle (RrI)

On the ebb, the RrI curves also appear, as at station A, in the form of tiny sawtooth shapes with no peaks (**Figure 5**). The RrI values are zero at the end of the ebb tide for B6, B7 and B8 because the wave energy is low enough to reach them and cause movement. B9 and B10 continue to be submerged without any real trends emerging. In the flow, the RrI curves of B6, B7 and B8 have very pronounced sawtooth shapes reaching extremes of 5cm and −3.5 cm. B9 and B10, on the other hand, have slight saw teeth with no peaks. The maximum amplitude of sediment movement is 12 cm for RrI.

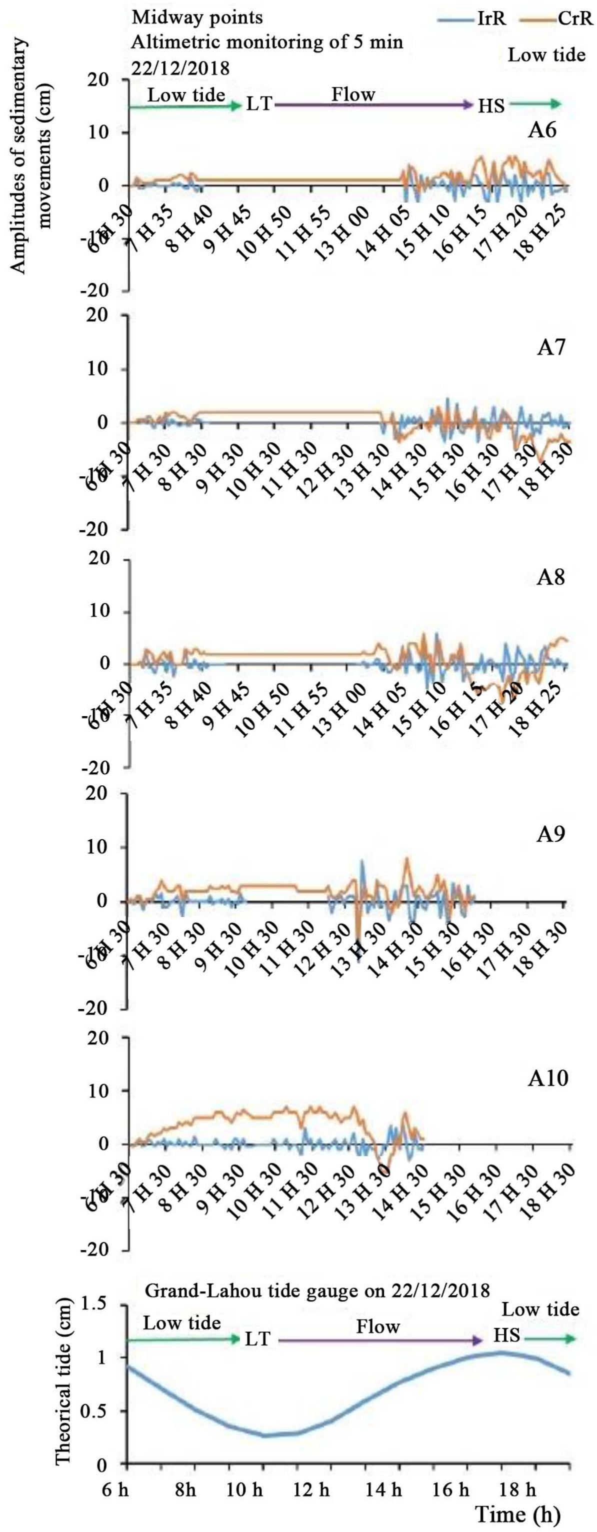

Figure 4. Continuous beach monitoring curves for the mid-foreshore at stations A.

Cumulative resulting reshuffle (RrC)

On the ebb, the general trend is towards accretion, which is clear at certain points (B6, B9 and B10), while other points (B7 and B8) show less accretion, to the extent that a sort of stability can be felt at these points. B9 and B10 continue to accrete before being eroded. Then a new phase of accretion begins for both posts before they are submerged. B7 shows no real trend during the flood until high tide, when the sediment input is so great that it reaches a maximum peak of 25.5 cm. B7 is the stake that is the most fattened of all the mid-foreshore stakes. For points such as B8, which show no trend, this is due to the fact that they are located at the point where the waves fall during the flow. The maximum amplitude of sediment movement is 25.5 cm for RrC.

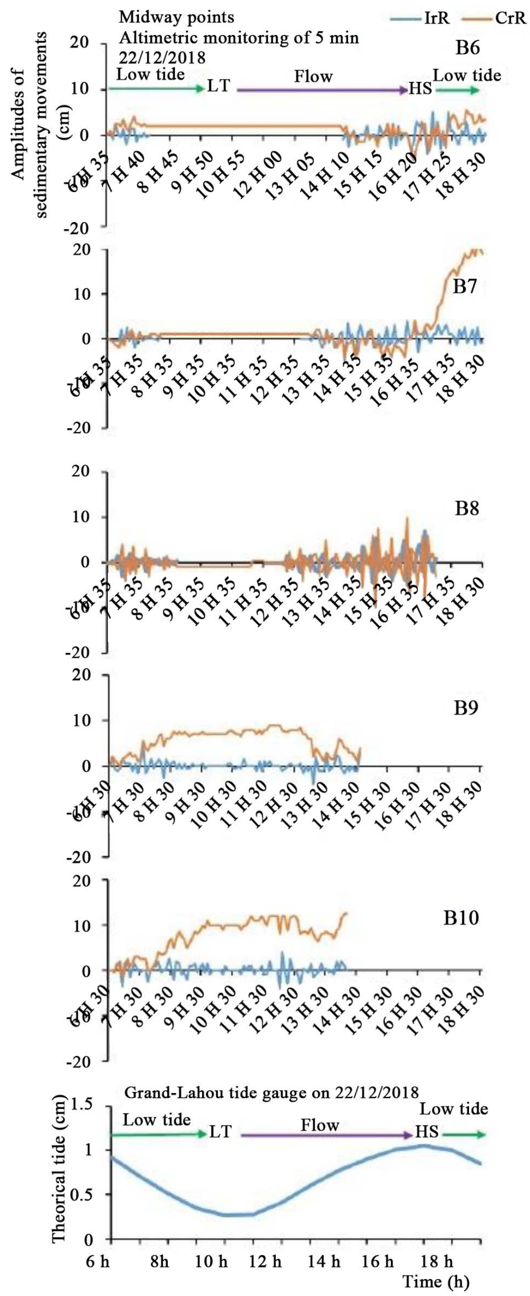

Figure 5. Continuous monitoring curves from the beach to the mid-foreshore of the control station.

3.1.3. Amplitude of Movement of Sediments on the High Foreshore of the Catholic Mission

a. Amplitude of movement at station A

Instant resulting reshuffle (RrI)

As the pickets were not submerged, this part of the shoreline remained stable.

Cumulative resulting reshuffle (RrC)

On the ebb tide, the RrC curves show stabilisation on all the picket of the high foreshore because the wave energy is too low to reach the picket, so the amplitude of mobilised sediment remains constant. This results in straight lines. Stakes A3, A4 and A5 are fattened until the end of the measurements (**Figure 6**). The extremes are 0 cm and 9 cm at point A5. The maximum amplitude of sediment movement is 9 cm for the RrC of profile A on the high foreshore.

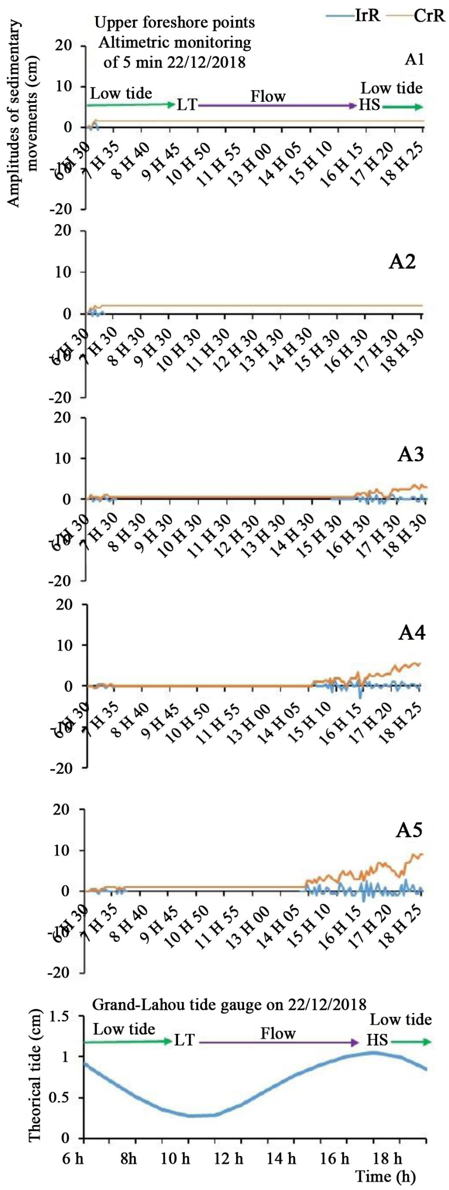

Figure 6. Continuous monitoring curves from the beach to the high foreshore: station A.

b. Amplitude of movement at station B

The picket at station B are B1, located 24.5 m from the coastline, B2, B3, B4 and B5.

Instant resulting reshuffle (RrI)

At ebb tide, all the pickets stabilise during the short time they may have been submerged by the waves. The straight lines show the constancy of the sediment in the absence of wave action.

At the flow, no trend emerged for B1 and B2 as the wave energy was too low to affect them. B3 became slightly fatter until the end of the measurements. B4 and B5 also became fatter, but in a progressive manner (Figure 7). All these accretions took place during high tide because the wave energy was powerful enough to reach pickets B3, B4 and B5. The extremes were observed at point B4 with 0 cm and 12.5 cm. The maximum amplitude of sediment movement was 12.5 cm for the RrC on the high foreshore.

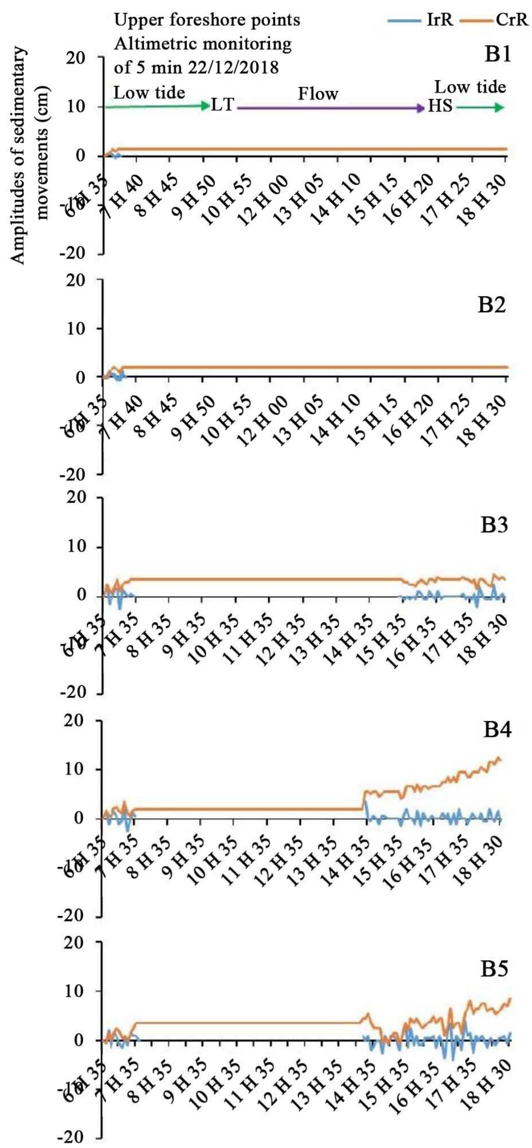

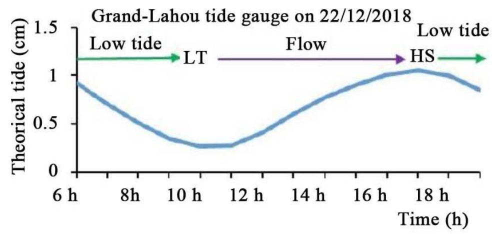

Figure 7. Continuous monitoring curves from the beach to the upper foreshore: control station.

3.1.4. Amplitude of the RrI and RrC in Stations A and Controls in One Tidal Cycle for a Follow-Up of 5 Min

The RrI curves show lower values than the RrC curves at all stations A and B except for points A7, B11 and B13 (**Figure 8**). The determination of the maximum amplitude of rearranged sediments at a point in the profile should take into account the greater of these two parameters (RrC and RrI).

For station A, the amplitudes of the RrI increase from A1 (1.5 cm) to A9 (19 cm). This amplitude falls at point A10 (7.5 cm), rises again at point A11 (11cm) before falling again at point A12. The amplitudes of RrC are also increasing from A1 (2 cm) to A9 (15.5 cm) with a slight drop at point A6. There is a drop at point A10 (12.5 cm) before a return to stabilization between A10 and A12 (15 cm).

For station B, the amplitudes of RrI and RrC increase together up to point B8. After the drop at point B9, the different amplitudes tend to stabilise. The maximum amplitude shows the points at station A becoming fatter. The maximum amplitude is 19 cm at point A9 on the mid-foreshore. For station B, all parts of the foreshore are getting fatter despite a few falls. The maximum amplitude is 25.5 cm at point B7 on the mid foreshore (**Table 1**).

Table 1. Maximum sediment amplitudes on profiles A and B in the tidal cycle for a 5mn monitoring on 22/12/2018.

	A1	A2	A3	A4	A5	A6	A7	A8	A9	A10	A11	A12	
Rrl mini	−0.5	−0.5	−1	−3	−2.5	−4	−5	−5	−11.5	−3	−5	−5	
RrI max	1	1	1.5	2	3	4	4.5	6	7.5	4.5	6	4	
RrC	0	0	0	−0.5	0	−1.5	−7.5	−8	−7.5	−5.5	−9	−4	
Rrc	2	2	3.5	5.5	9	5.5	3	6	8	7	4	11	
Ampl	1.5	1,5	2.5	5	5.5	8	9.5	11	19	7.5	11	9	
Ampl	2	2	3.5	6	9	7	10.5	14	15.5	12.5	13	15	
Ampl	2	2	3.5	6	9	8	10.5	14	19	12.5	13	15	
	B1	B2	B3	B4	B5	B6	B7	B8	B9	B10	B11	B12	B13
RrI mini	−0.5	−0.5	−2.5	−2.5	−4	−4	−5	−5	−4	−4	−4.5	−3	−3
RrI max	0.5	1	2.5	3	4	5	4	7	4	4	4	2	3
Rrc	0	0	0	0	−0.5	−5.5	−4.5	−10	0	−6	−6	−4	−8.5
Rrc	1.5	2	4.5	12.5	8.5	5.5	21	10	9	2	2	3	1.5
Ampl	1	1.5	5	5.5	8	9	9	12	8	8.5	8.5	5	6
Ampl	1.5	2	4.5	12.5	9	11	25.5	20	9	8	8	7	10
Ampl	1.5	2	5	12.5	9	11	25.5	20	9	8.5	8.5	7	10

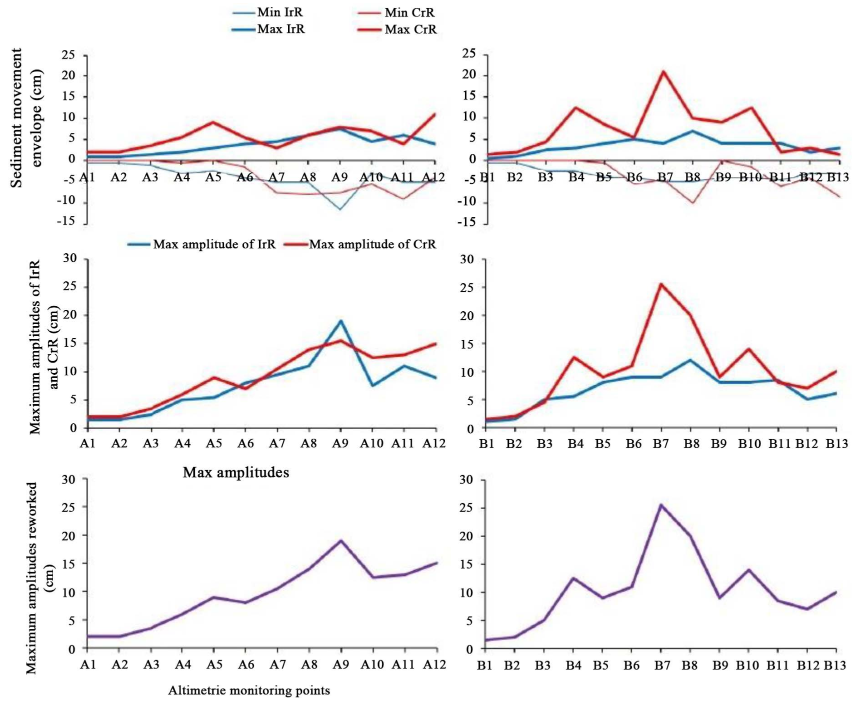

Figure 8. Amplitudes of the resulting instantaneous and cumulative reworking on Grand-Lahou beach

3.2. Annual Beach Dynamics

A comparison of the 1998 and 1999 profiles (**Figure 9**) shows that the coastline at Mission Catholique is stable. The low foreshore is eroding in favour of the high beach. The sediment balance is negative by -6.55 $m^3\ ml^{-1}$ of linear metre. A comparison of the 2006 and 2007 profiles (**Figure 10**) shows that the coastline has retreated by around (5.3 m). The sediment balance is very negative at 29.65 $m^3\ ml^{-1}$ linear metre. Superimposing the profile of 18/10/2017 and that of 22/12/2018 shows that the coastline has remained stable. Generally speaking, it can be seen that the beach at the Catholic mission is becoming deeper. The volume of the eroded surface was -3.51 $m^3\ ml^{-1}$ per linear metre, compared with a deposit of 88.32 $m^3\ ml^{-1}$ per linear metre. This gives a positive volume balance of 84.81 $m^3\ ml^{-1}$ m^3 linear metre of sediment. The shape of the GL1 profile indicates the presence of strong movements at the level of the cemetery with several subtleties. There is no eroded sediment, but there is a considerable input of sediment. Superimposing the two profiles (18/10/2017 and 22/12/2018) shows that the cemetery beach is growing adequately with a volume balance of 107.87 $m^3\ ml^{-1}$ per linear metre. The coastline remains stable. The mid foreshore and low foreshore will erode in favour of the high beach between October 2022 and July 2023.

3.3. Beach Dynamics in the Medium and Long Term (2 Years; 10 Years)

A comparison of the February 2006 and July 2008 profiles shows a concave profile in July 2008 as a result of severe erosion of the foreshore, with an estimated retreat of around 5 m during this period (**Figure 11**). The sediment balance was negative at −15,28 $m^3 ml^{-1}$ per linear metre. A comparison of the July 1998 and November 2007 profiles shows that erosion predominated during the 1998-2007 decade. The retreat of the coastline is estimated at around −4.8 m during this period. The sediment balance was negative by −30,35 $m^3 ml^{-1}$ of linear metre.

3.4. Beach Dynamics on a Storm and Seasonal Scale

Between May and August 2008, the shoreline retreated by an estimated 1.9 m (**Figure 12**). The erosion slope, which was around fifty metres from the lighthouse in May 2006, was only a few centimetres away in September 2008 (**Figure 13**). The coastline is retreating at an unusual rate, estimated at an average of 25 m.year/an between May 2006 and September 2008. The storms recorded in August 2007 undoubtedly had a considerable impact on this stretch of coastline. Twenty years after the construction of the 2nd lighthouse following the destruction of the first by heavy swells in July 1989, the authorities were obliged to build a third. In fact, given the threat of erosion, the lighthouse was dismantled and rebuilt twice as a precautionary measure. The enormous losses, generally located in the mouth area, have resulted in the destruction of the colonial heritage and the village cemetery… (**Figure 14**, **Figure 15**).

4. Discussion

The results show that the mobile layer on Grand-Lahou beach is between 4.5 cm and 12.5 cm on the upper beach and between 9 cm and 25.5 cm on the mid-shore. On the low foreshore, the mobile layer is between 7 cm and 15 cm with little sediment movement. This study reveals that the maximum amplitude of sediment movement corresponding to the thickness of mobilised sediment (25.5 cm) is acquired at mid-foreshore. The present study reveals a maximum effective reworking (Re) of 22.5 cm. These various sedimentary movements were also noted by [30] in his study of Port-Bouët beach.

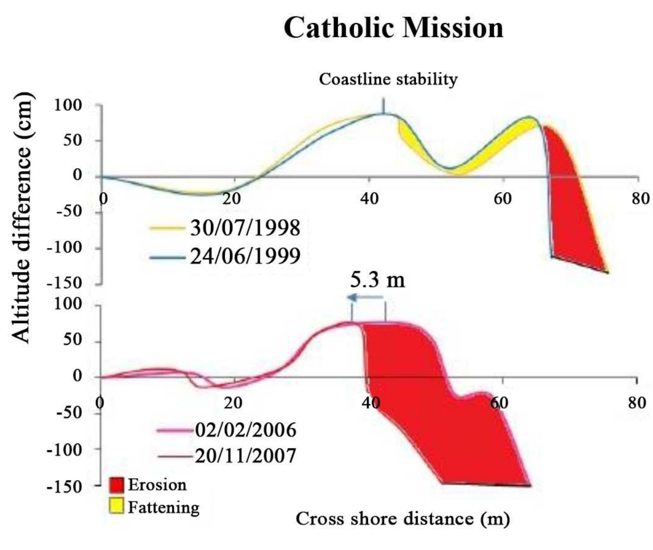

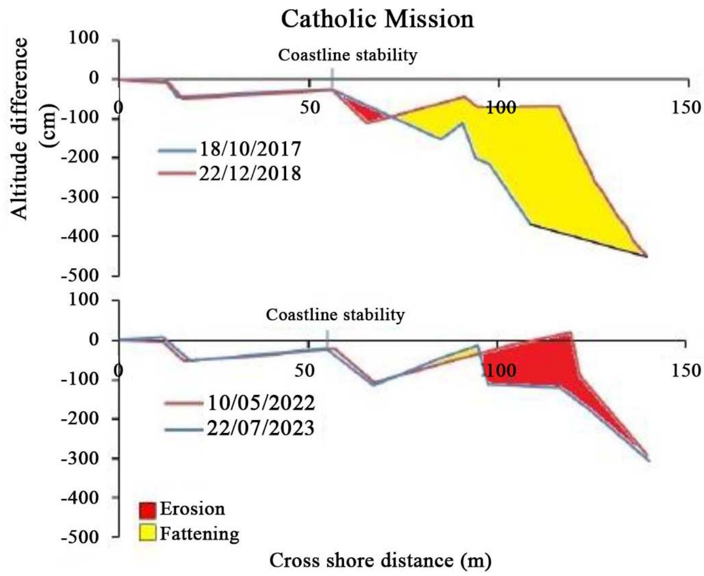

Figure 9. Interannual sediment evolution (1998-2023) of the foreshore and coastline on a coastal section of Grand-Lahou.

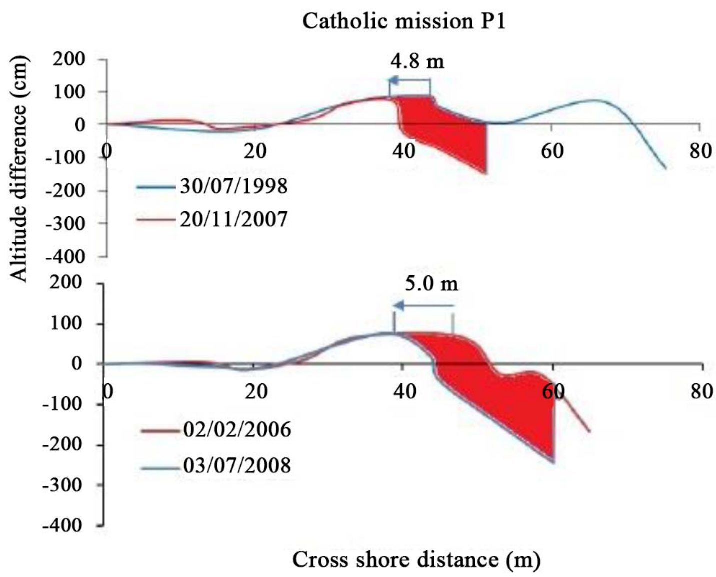

Figure 10. Interannual sediment trends (1998-2008) in the foreshore and coastline of the Catholic mission of Grand-Lahou.

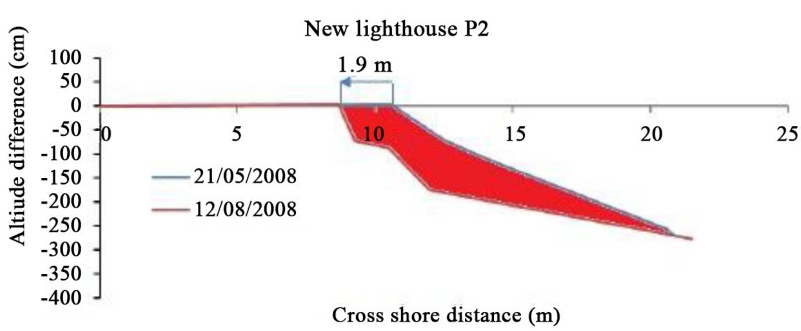

Figure 11. Evolution of the beach during heavy swells.

Figure 12. Erosion slope 50 m from.

Figure 13. Erosion slope at the lighthouse the lighthouse in May 2006 on 25 September 2008.

Figure 14. Well exposed at the mouth (May 2007).

Figure 15. Destruction of graves by erosion at Lahou-Kpanda (December 2018).

However, the maximum amplitude of sediment movement was 53 cm at mid-foreshore on Port-Bouët beach, compared with 25.5 cm on Grand-Lahou beach. The beach at Grand-Lahou is said to be less steep than that at Port-Bouët [21] [31]. It is characterised by concave topo-bathymetric profiles with medium to very steep slopes. The foreshore and underwater beach (−10 m) are made up of coarse to very coarse sands [32]. The coarsest and best sorted sediments are located in the Port-Bouët area. The grain size of beach sands varies between 764 µm and 1419 µm [5]. Studies have shown that the tide and beach morphology influence sediment dynamics in the swash zone [33]. The three factors involved in the morphodynamics of the swash zone are: hydrodynamics, slope and the granulometric characteristics of the beach. The behaviour of the swash zone is thought to be governed by various hydrodynamic and environmental factors such as wave height in the surf zone and beach slope, which change over the tidal cycle [34]. The morphology of the area submerged by the tide is constantly changing as the waves pass over it [9]. At each point of the profile, the beach has the necessary slope to allow the amount of wave energy to develop and thus have a volume of suitable size mobilisable sediment. Sediment transport intensifies as the slope increases until it reaches a maximum value. The value of this optimum slope depends on the speed of the current and on how far the river can progress over the sand [15]. The beach at Port-Bouët would have the necessary slope to allow the amount of wave energy to develop and thus have a greater volume of mobilisable sediment than the beach at Grand-Lahou. The beach of Grand-Lahou is also subjet to a rate of fattening during the tidal cycle considered to be much more pronounced in mid-offshore. A few episodes of minor erosion have nevertheless been recorded, but these are minimal compared with the sediment input. These results show that the dynamic swash zone, subject to major sediment flows, varies according to the phases of the tide. On the ebb tide, this zone is reduced to the low foreshore and a few points on the mid foreshore depending on the tide-swell conditions. At the flow, the area widens taking into account the upper shore. Generally speaking, on the scale of a tidal cycle, the flow of sediments transported increases with the tidal coefficient and is greater during the semi-diurnal tides of agitated to very agitated spring tides than during the semi-diurnal tides of calm to slightly agitated neap tides. The flow phase characterized by strong currents (tide and swell) is the most turbid [9]. The superposition of profiles at annual scale at the Catholic mission level shows that the coastline is stable. Generally, gains in sediment outweigh losses. However, between 2006 and 2007 there was an estimated retreat of 9m. We can therefore attest to the erosive nature of the beach during this period. The decade 1998-2007 at the level of the Catholic mission is marked by a retreat in the coastline estimated at 4.8 m. The retreat is estimated at 5 m between 2006 and 2008. These results show a decline that varies over time. Erosion is more pronounced at the mouth. Work by Koffi (2017) [29] revealed that the village cemetery area is experiencing the greatest shoreline regression with recession rates of −4.6 m/yr. Erosion at Grand-Lahou is exacerbated by a lateral (east-west) migration of the mouth of the Bandam river [5]-[7]. This study confirms this trend, with the corollary of destroying the lighthouse and the village tombs. The disappearance of the rocky banks under the mud at the mouth of the river would leave this area without natural defences, particularly vulnerable to erosion [5]. The sediments eroded in the cemetery sector were transported towards the western sector and the Catholic mission by an east-west longshore drift reported by Wognin (2004) [23]. This allows us to establish a relationship between sediment budgets and hydrodynamic forcing (waves). This could explain the dynamics of the Grand-Lahou beach, which, according to [23] and [5] is eroding in areas close to the mouth while rebuilding in areas further away. Apart from the so-called natural forcings (hydrodynamics, meteorological flows, morphological), another limiting factor of the advance of the coastline is the anthropogenic factor. Beach erosion is sometimes constrained by human constructions that provide additional protection against marine hydrodynamic forcing [9]. Areas that appear to be less dynamic reflect either the stability of these areas or accretion that is equivalent or almost equivalent to the erosion they are undergoing. When an annual time step is considered, the sediment balances are variable, sometimes positive, sometimes negative, which shows the variability and importance of the different hydrodynamic forcings acting on Grand-Lahou beach. These observations are consistent with those in the literature [3] [9].

5. Conclusion

The quantification of the sedimentary balance by zone and time period made it possible to highlight the sedimentary evolutions of the Grand-Lahou beach between

1998 and 2023, that is 25 years. The synthesis of the results allows us to observe the evolutionary trends of each zone by crossing their dynamics for different time steps (tide cycle, storm, year: 10 years). On the scale of a tidal cycle, the curve of the maximum reworked amplitude shows a marked deepening at mid-foreshore with a maximum amplitude of 25.5 cm compared with amplitudes of 15 cm and 12.5 cm respectively at low foreshore and high beach. The maximum effective reworking was 22.5 cm. The quantitative balance of the sedimentary reworking shows that overall, the beach is fattening. However, there is partial erosion of the coloured sediments. On an annual scale, the balances are rather variable, sometimes positive (2017-2018) and sometimes negative (1998-1999 and 2006-2007), reflecting the influence of different forcings (swell, tide) which vary from one period to another. On a ten-year scale (1998-2007), the retreat of the coastline is estimated at around 4.8 m. We have concluded that the beach is generally eroding over this period. However, the relatively low sediment balance indicates that the beach is relatively stable at this time scale. This sector does not therefore appear to be subject to any significant evolutionary trends at this time step. At the scale of the study area as a whole, the results show that the coastline is not evolving in the same way on the beach, as the different sectors are not exposed to forcing in the same way. The Catholic mission area is less subject to strong marine hydrodynamic forcing than the mouth area. The Catholic Mission sector, which appears to be relatively undynamic over the entire study period, shows low sediment balances, in line with its relative stability. The most significant retreats were observed at the mouth and during exceptional events such as storms. The retreat of the coastline, estimated at 25 m.yr-1 between May 2006 and September 2008, is thought to have been caused by the storms recorded in August 2007. The mouth of the river is located in an area where hydrodynamic forces have the most energy and are likely to cause severe erosion, even on the upper beach. Lateral migration of the mouth of the Bandama River is the main cause of erosion of the Grand-Lahou beach and therefore the main threat to the local population, given the damage recorded at the cemetery during the study period.

Conflicts of Interest

The authors declare no conflicts of interest regarding the publication of this paper.

References

[1] Agardy, T., Alder, J., Dayton, P., Curran, S., Kitchingman, A., Wilson, M. and Vörösmarty, C. (2005) Coastal Systems. In: *Ecosystems and Human Wellbeing: Current State and Trends. Volume* 1. *Conditions and Terms*, *Findings of the Condition and Trends Working Group of the Millennium Ecosystem Assessment*. Island Press, Washington.

[2] Perrin, A. (2015) Utilisation des médias sociaux. *Pew Research Center*, **125**, 52-68.

[3] Bouillet, M.L. (2022) Analyse multi-échelles et multi-capteurs des évolutions morphodynamiques des fonds de la Baie de Somme. Sciences de l'ingénieur [physics]. 71 p.

[4] Bird, E.C.F. (1993) Submerging Coasts. The Effects of a Rising Sea Level on Coastal

Environments. John Wiley and Sons, 184 p.

[5] N'Doufou, G.H.C. (2012) Contribution de l'étude morphosédimentologique et exoscopique à la compréhension de l'évolution du secteur du littoral ivoirien entre Sassandra et Abidjan. Thèse de Doctorat, Univ. Felix Houphouët Boigny, 193 p.

[6] Haouhouot, C. and N'doufou, C. (2009) Sedimentary dynamics of the Ivorian coastline between Grand-Lahou and Abidjan. Revue de Géographie Tropicale et d'Environnement, 2.

[7] Hauhouot, C., Koffi, P. and Pottier, P. (2015) Sensibilité des plages du littoral ivoirien à l'érosion. Les risques littoraux, atlas permanent de la mer et du littoral, LETG-Nantes Géolittomer, UMR 6554-Cnrs, n°7 Juin, 26-29.

[8] Pomel, R.S. (1979) La prismation des «laves en pavés» à Lanzarote et Ténérife (Iles Canaries). *Bulletin de l'Association de géographes français*, **56**, 275-281. https://doi.org/10.3406/bagf.1979.5114

[9] Charlotte, M. (2016) Morphodynamique et transferts sédimentaires au sein d'une baie mégatidale en comblement (Baie de Somme, Manche Est). Stratégie multi-échelles spatio-temporelles. Thèse Géomorphologie, Normandie Université.

[10] Bonnot-Courtois, C., Bassoullet, P., Le Hir, P., Tessier, B., Cayocca, F. and Baltzer, A. (2006) Évolution et mobilité des sédiments superficiels de l'estran occidental de la baie du Mont Saint-Michel. *Actes IXèmes Journées Génie Côtier—Génie Civil*, Brest, 57-64. https://doi.org/10.5150/jngcgc.2006.014-b

[11] Bonnot-Courtois, C., Bassoulet, P., Tessier, B., Cayocca, F., Le Hir, P. and Baltzer, A. (2008) Remaniements sédimentaires superficiels sur l'estran occidental de la baie du Mont-Saint-Michel. *Revue européenne de génie civil*, **12**, 51-65. https://doi.org/10.3166/ejece.12.51-65

[12] Koffi, K.P. (1981) Contribution à l'étude des processus sédimentaires dans la zone littorale Aquitaine (France): Remaniements et transport en suspension. Thèse Doctorat 3ème cycle, Univ. Bordeaux I, n° 1718, 145 p.

[13] Richmond., B. and Sallenger, A. (1984) Transport transversal de sables bimodaux, Coastal Engineering Proceedings, n° 19.

[14] Osborne, P.D. and Rooker, G.A. (1999) Sand Re-Suspension Events in a High Energy Infragravity Swash Zone. *Journal of Coastal Research*, **15**, 74-86.

[15] Degryse-Kulkarni, C. (2003) Morphodynamique de la zone de swash. Thèse Sciences de la Terre, Université de Caen Basse-Normandie.

[16] Jestin, H., Bassoullet, P., Le Hir, P., L'Yavanc, J. and Degres, Y. (1998) Development of ALTUS, a High Frequency Acoustic Submersible Recording Altimeter to Accurately Monitor Bed Elevation and Quantify Deposition or Erosion of Sediments. *IEEE Oceanic Engineering Society. OCEANS'*98. *Conference Proceedings*, Vol. 1, 189-194. https://doi.org/10.1109/oceans.1998.725734

[17] Tastet, J.P. (1972) Quelques considérations sur les classifications des côtes. La morphologie côtière ivoirienne. *Annales de l'Université d'Abidjan*, (*C*), **8**, 135-162.

[18] Abe, J., Bakayoko, S.B., Bamba and Koffi, K.P. (1993) Morphologie et hydrodynamique à l'embouchure du fleuve Bandama. *Journal Ivoirien d'Océanologie et de Limnologie*, **2**, 9-24.

[19] Varlet, F. (1958) Le régime Atlantique près d'Abidjan, Côte d'Ivoire: Essai d'océanographie littoral. *Etudes Eburnéennes*, **7**, 222.

[20] Hinschberger, F. (1977) Aspects et problèmes d'aménagement du littoral en Côte d'Ivoire. *Cahiers du Centre nantais de recherche pour l'aménagement régional*, **13**, 51-63. https://doi.org/10.3406/canan.1977.1304

[21] Martin, L. (1973) Morphologie sédimentologie et paléogéographie au quaternaire récent du plateau continental ivoirien. Th. Sc. Nat., Paris VI Trav. Doc. ORSTOM, No. 61, 126, fig., 266 p.

[22] Lecolle, J. (1971) Sédimentologie des fonds lagunaires et estuariens. Variations morphologiques saisonnières de l'embouchure d'un fleuve en climat intertropical (Le Bandama-Côte d'Ivoire). Cahiers ORSTOM, Série. Géol., III, 2, 189-220.

[23] Wognin, A.V. (2004) Caractérisation hydrologique et sédimentologique de l'embouchure du fleuve Bandama. Thèse de Doctorat, Univ. Cocody, 195 p.

[24] Dehouck, A. (2006) Morphodynamique des plages sableuses de la mer d'Iroise (Finistère). Thèse de doctorat en géographie physique, Université de Bretagne Occidentale, 262 p.

[25] Robin, M. (2002) Télédétection et modélisation du trait de côte et de sa cinématique. In: *Le littoral*: *Regards*, *pratiques et savoirs*, Éditions Rue d'Ulm/Presses de l'École normale supérieure, 230 p.

[26] Brabant, M. (2003) Maîtriser la topographie, des observations au plan. Eryolles, 539 p.

[27] Sallenger, A.H. and Richmond, B.M. (1984) High-Frequency Sediment-Level Oscillations in the Swash Zone. In: *Developments in Sedimentology*, Elsevier, 155-164. https://doi.org/10.1016/s0070-4571(08)70145-6

[28] Kroon, A. (1994) Sediment Transport and Morphodynamics of the Beach and Nearshore Zone, near Egmond, The Netherlands. Thèse de Doctorat, Univ. Utrecht (NL), 275 p.

[29] Koffi, K.P. (2017) Etude de l'évolution morpho-sédimentaire du littoral ivoirien: Remaniement sédimentaire à l'échelle multi-temporelle. Thèse de Doctorat, Université felix houphouët boigny-abidjan, 322 p.

[30] Saimon, A.A.M. (2011) Contribution à la connaissance de la dynamique sédimentaire du littoral ivoirien: Cas du périmètre littoral de Port-Bouët. Mém. DEA Université Cocody, 79 p.

[31] Monde, S. (1997) Nouvelles approches de la cartographie du plateau continental de Côte d'Ivoire: Aspects morphologiques et sédimentologiques. Thèse Doctorat 3ème Cycle, Université Cocody, 175 p.

[32] Koffi, K.P., Abe, J. and Affian, K. (1989) Rapport technique de l'étude complémentaire du littoral de Vridi-Port-Bouêt, Morphologie et sédimentologie. N.D.R. n°3, Centre de Recherches Océanologiques Abidjan, 25 p.

[33] Guedes, R.M.C., Bryan, K.R., Coco, G. and Holman, R.A. (2011) The Effects of Tides on Swash Statistics on an Intermediate Beach. *Journal of Geophysical Research*, **116**, C04008. https://doi.org/10.1029/2010jc006660

[34] Enjalbert, C., Senechal, N., Bryan, K., Coco, G., Macmahan, J. and Brown, J. (2012). Dynamique de la zone de swash: Influence de la marée et de la morphologie sur les paramètres du run-up. *XIIèmes Journées Nationales Génie Côtier—Génie Civil*, Cherbourg, 12-14 June 2012, 51-58. https://doi.org/10.5150/jngcgc.2012.006-e